The Dissertation Committee for Fahmida Ferdousi Certifies that this is the approved version of the following dissertation:

Device Design and Process Integration of High Density Nonvolatile Memory Devices

Committee:

Sanjay K Banerjee, Supervisor

Leonard F. Register

Emanuel Tutuc

Edward Yu

Maxim Tsoi

Device Design and Process Integration of High Density Nonvolatile Memory Devices

by

Fahmida Ferdousi, B.S.E.E.; M.S.E.

Dissertation

Presented to the Faculty of the Graduate School of

The University of Texas at Austin

in Partial Fulfillment

of the Requirements

for the Degree of

Doctor of Philosophy

The University of Texas at Austin

May 2011

Dedication

To my favorite teachers

Acknowledgements

I would like to thank my supervisor Prof. Sanjay K Banerjee for providing support and guidance during my graduate studies and helping me to be an independent, responsible researcher. I want to specially thank Dr. Maxim Tsoi for his supervision, discussion, and guidance on the spin-torque project and also for serving in my dissertation committee. I also want to thank Dr. Emanuel Tutuc, Dr. Leonard F. Register, and Dr. Edward Yu for serving in my dissertation committee and helpful discussions over time. I want to especially thank Dr. Kelin Kuhn, my manager during internship at Intel, for being a wonderful teacher and giving me confidence. I want to thank Dr. Swaroop Ganguly and Dr. Luigi Colombo for the helpful discussions. I thank Jeannie, Melanie, Bill, Jesse, Johnny, Gabriel, Ricardo, Brenda, Rachel, James, Darren, Gerlinde and Joyce for doing their magic everyday so that our work goes smoothly. I would like to thank my group mates and lab mates for their help, patience and co-operation, especially Dr. Joseph Donnelly, Doreen Ahmad, Dr. Joy Sarkar, Dr. Marylene Palard, Dr. Shan Tang, Dr. Sachin Joshi, Dr. Davood Shahrjerdi, Michael Ramon, Sayan Saha, Dr. Aparna Gupta, Tarik Akyol, Jason Mantey, Seyoung Kim, Shagandeep Kaur, Emmanuel Onyegam, Heidi Seinige and Urmimala Roy. I thank my teachers from elementary up to graduate school for always showing me the way. I am grateful to my family and friends who support me even on my worst of days. Last but not least, I thank my friend, group mate, and husband, Mustafa Jamil, for taking the high road with me; it is not an easy journey.

Device Design and Process Integration of
High Density Nonvolatile Memory Devices

Publication No._____________

Fahmida Ferdousi, PhD
The University of Texas at Austin, 2011

Supervisor: Sanjay K Banerjee

This research focuses on device design and process integration of high density nonvolatile memory devices. Research was carried out to improve scaling of floating gate memories by increasing charge density as well as spin-based memories by reducing critical switching current. This work demonstrates fabrication of CMOS-compatible nonvolatile hybrid memory device using fullerene molecules as a floating gate. Molecules have dimensions of several Angstroms resulting in an electron density of $\sim 10^{13}$ cm^{-2} or higher. In hybrid MOSCAPs, fullerenes were encapsulated between inorganic oxides, i.e. SiO_2 as a tunnel oxide and HfO_2 as a control oxide. Introduction of a high-k material as a control oxide improves capacitive coupling between control gate and floating gate as well as the program/erase efficiency. The MOS capacitors demonstrate nonvolatile memory operation at room temperature. The device data infers that program/erase mechanism in fullerene devices is Fowler-Nordheim tunneling; however, retention is determined by trap-assisted tunneling.

The next part of the work focused on spin-transfer-torque (STT) based magnetic memory. Spin-based memory has the unique potential to be the universal memory because of its high density, fast switching, and nonvolatility. This work presents STT switching of perpendicular magnetic anisotropy (PMA) spin-valves with tilted magnetization using point contact measurement. The PMA materials have high coercivity resulting in good retention and tilted magnetization induces precessional switching resulting in a lower switching current density. First, micromagnetic simulations were performed for spin-valves with tilted magnetization and precessional switching was observed to reduce the switching current. Then, spin-valve structures were fabricated by e-beam evaporation. The structure consisted of Co/Pt and Co/Ni layers, where the thickness of the layers was optimized to obtain different amount of tilt in magnetization. Point contact measurements of tilted spin-valves show STT switching, where the switching field of the free layer varies with the magnitude and sign of the applied current. The observed STT effect is stronger in a 45° tilted spin-valve compared to a 12° tilted device presumably due to the tilted spin polarization. However, tilting introduces nonuniform effective field and canting of the domains which affect the STT.

Table of Contents

List of Tables

List of Figures

Chapter 1: Introduction

1.1 High density nonvolatile memory devices

Nonvolatile memory market has grown extensively in the past few years and cost has been reducing due to the high density and high programming throughput. Among the nonvolatile products, flash memory is very popular especially in portable market. Recent research is also focusing on flash-based solid state drives to replace conventional magnetic hard disk as a storage medium. As the market expands, widespread research is going on to improve the performance of flash devices as well as continue scaling to lower dimensions. Table 1.1 shows comparison among different promising nonvolatile memory structures.[1] Figure 1.1 shows the schematic of a conventional flash memory device. The device is similar to a MOSFET structure with multiple stacks in the gate where a floating gate is sandwiched between a tunnel oxide and a blocking oxide. Floating gate is the storage node that acts as a potential well and is charged and discharged by applied electric field on the control gate. If no field is applied, then the floating gate should store the charge for 10 years which is the retention requirement. The devices are expected to survive through 10^5 cycles of program/erase (P/E) operations.

1.2 Scaling issues

Scaling issues concerning flash devices are mainly twofold. Complementary MOS (CMOS) technology is governed by Moore's law: double the number of transistors every two years[2] which is achieved through scaling the devices following Dennard's scaling theory[3]. According to Dennard's theory if the gate oxide and the applied voltage are scaled down, effective field in the channel region is unchanged which allows scaling of gate length and area, thus giving cost/Si and delay improvement. Moreover, scaling of applied voltage and capacitance allow low power and faster operation. However, scaling of oxide in flash devices is limited due to the defects in tunnel and blocking oxide. These defects result in charge loss from the floating gate which reduces retention time. Moreover, defects also result in a threshold voltage (V_{th}) shift of the devices which limits device operation to less than 10^5 cycles. The thickness of tunnel oxide in a conventional flash device is thus limited to ~7-9 nm which prevents the overall scaling of the devices. Another important scaling issue is to maintain an electron density of at least 10^{12} cm^{-2} to achieve a reasonable memory window as the gate lengths become smaller. Reducing V_{th} variation among devices is also very important to achieve uniformity throughout the chip.

1.3 Evolution of flash memory devices

The design and architecture of flash devices have been evolving to circumvent the scaling issues mentioned above. Charge loss through tunnel oxide is the limiting case for scaling the conventional continuous poly-Si floating gate device. However, if the charge is stored in a discrete, i.e. nanocrystal[4] or trap-based[5], floating gate then defects in the oxide will result in a localized charge loss. Thus most of the charges in the floating gate will be retained.[6]This improvement in retention allows a thinner tunnel oxide design. Moreover, band-gap engineering in the tunnel oxide has been proposed to improve retention as well as programming speed. High-k oxide has been introduced as a blocking oxide to improve control gate to floating gate capacitance.[5] Metal gates with different work functions have been studied to improve the memory window.[7] However, as devices are scaled down, memory operation is affected in two ways. Total charge stored in a device is less with smaller area available which results in a smaller memory window.[8]This affects retention and devices are more vulnerable to interference and crosstalk. Moreover, total charge varies among devices due to nonuniform deposition of floating gate, especially in nanocrystal floating gates, which results in a V_{th} variation and causes yield issues. Various schemes have been proposed in the literature to improve uniformity.[4,9,10] One of the methods proposed nanocrystal assembly using a protein called Chaperonin 60 or GroEL.[9] In this method, nanocrystals are assembled on an oxide surface using GroEL. Nanocrystal assembly using GroEL on the vertical sidewalls has also been demonstrated.[8]This result implies that the mechanics of the method depends more on Van Der Waals force than gravity.[8] The advantages of a vertical structure are that it improves cell density and provides greater surface area for nanocrystal deposition on sidewalls than a planar structure of similar dimensions. Hence, threshold voltage variation might be further reduced.

A recent development to improve charge density in the floating gate is to employ organic molecules as a storage node.[11,12] Organic molecules have dimensions of several Angstroms and multiple charge storage levels, resulting in an electron density of $5\text{x}10^{13}$ cm^{-2} or higher, which makes them very attractive as a storage medium in highly scaled memory devices. Moreover, lateral electron mobility in organic molecules is generally much lower than 0.1 $cm^2/(V \cdot s)$ which makes charge storage discrete. Different device structures have been proposed in the literature incorporating different organic molecules for memory operation but many of the devices reported so far are two-terminal devices sensing changes in resistance or capacitance.[13,14] In addition, much of the fabrication and electrical characterizations need to be done in a vacuum or controlled environment to obtain memory operation.[11,15] Moreover, two-terminal devices require a select transistor for circuit integration, which increases area requirement and design complexity. On the other hand, thermal stability of molecules is an important criterion for CMOS process integration. The molecules should have thermal stability of up to 400°C or more to be compatible with high-volume CMOS production.

For low-power and fast operation of memory devices, direct tunneling or Fowler–Nordheim (FN) tunneling are used as P/E mechanisms. The continued scaling of memory devices requires the use of new materials as control oxide to extend the direct tunneling regime or improve the programming window in the FN regime. Introduction of a high-k material as a control oxide improves capacitive coupling between control gate and tunnel oxide as well as the P/E efficiency due to high dielectric permittivity of the materials.[16,17] For most high-k materials, the improvements of higher permittivity are diminished by poor retention resulting from the low conduction band offset of these materials. Table 1.2 shows the dielectric permittivity, conduction band offset, valence band offset, and energy gap among different insulating dielectric materials.[18]

Recently memory research is focusing on new materials and device architectures for high density, low power, and nonvolatile application. A strong candidate for future nonvolatile memory is spin-transfer-torque (STT) based magnetoresistive random access memory (MRAM). A detailed discussion on STT MRAM is presented in the following section.

1.4 Spin-transfer-torque-based nonvolatile memory device

Spin-transfer-torque-based MRAM has the potential to be the "universal" memory device, especially for nonvolatile applications because of its high density, fast switching, and nonvolatility.[19,20]Spin-transfer-torque was first predicted by Slonczewski[21] and Berger[22] and then experimentally demonstrated by Tsoi et al.[23] Figure 1.2 shows a schematic of a conventional STT MRAM structure. The memory consists of two ferromagnetic (FM) layers separated by a non-FM barrier. If magnetizations of both the FM layers are in the same direction or parallel, then resistance through the structure is low; if the magnetizations are in antiparallel direction then the resistance is high. The percentage change of resistance is known as magnetoresistance (MR). One of the FM layers has a pinned or fixed magnetization which is kept unchanged during device operation and is known as the reference layer. The other layer, which is known as the free layer, switches magnetization direction with respect to the reference layer. When electrons flow through the reference layer to the free layer, spin polarization occurs and these spin polarized electrons exert a torque such that the free layer may switch to parallel orientation if it were antiparallel. On the other hand, when electrons flow from the free layer, some of them get reflected at the reference layer/barrier interface; these reflected electrons have the opposite orientation of the reference layer. These oppositely polarized electrons may switch the free layer orientation in antiparallel direction, as shown in Figure 1.3.[24]If the non-FM barrier layer is a metal, then the structure is known as a spin-valve and it usually shows giant MR (GMR) of 1-2% or less. If the barrier is an insulating dielectric such as MgO or Al_2O_3, then the structure is known as magnetic tunnel junction (MTJ) and it usually shows tunneling MR (TMR) of well above 10%. The added advantage of MgO is that it shows spin filtering effect, as shown in Figure 1.4, which improves the TMR.[25] In 3d FM metal and alloys, Δ_1 Bloch states (spd hybridized states) have positive spin polarization, whereas Δ_2 (d) states have negative spin polarization. Crystalline (001) MgO allows coherent tunneling of Δ_1 states, while blocking other states, thus improving the spin polarization and TMR.[25]

Significant research is going on to develop FM materials with low damping constant, low saturation magnetization, and good remanance. The FM materials can be classified mainly based on their preferred magnetic anisotropy: in-plane and perpendicular to the plane. Among the in-plane materials Co-based alloys, especially CoFeB is the most popular because of its excellent interface with MgO(001), which results in a high TMR and high spin-polarization factor that reduces the critical switching current.[26] The critical switching currents for in-plane devices are given as[27]:

$$I_C^{P-AP} \approx \frac{A\alpha M_S V}{g(0)p}(H + H_{dip} + H_{K\|} + 2\pi M_S)$$
$$I_C^{AP-P} \approx \frac{A\alpha M_S V}{g(\pi)p}(H + H_{dip} - H_{K\|} - 2\pi M_S) \tag{1.1}$$

where α, M_S, V, and p are Gilbert damping constant, saturation magnetization, volume of the free layer and spin-polarization of current, respectively. The factor g depends on the relative angle of the free layer and reference layer. The factor A depends on the specifics of the transport model. $H, H_{dip}, H_{K\|}$ are the applied field, the dipole field from the reference layer acting on the free layer and the in-plane anisotropy field, respectively. The factor $2\pi M_S$ comes from the shape anisotropy of the in-plane material.[27] The two important factors from device application point-of-view are to reduce the critical switching current to less than 10^7 A/cm^2 and improve retention for 10 years. From equation 1.1, switching current can be improved by lowering damping constant and magnetization, scaling volume, and increasing spin-polarization. However, retention energy of in-plane materials is not suitable for 10 year nonvolatility since the energy depends on coercivity, which is smaller for these materials.

Perpendicular magnetic anisotropy (PMA) materials, on the other hand, do not suffer from the bulk shape anisotropy effect and they have a higher coercivity, thus improving retention. The critical switching currents for PMA materials are given as[27]:

$$I_C^{P-AP} \approx \frac{A\alpha M_S V}{g(0)p}(H_{K\perp} - 4\pi M_S - H_{dip} - H)$$
$$I_C^{AP-P} \approx \frac{A\alpha M_S V}{g(\pi)p}(-H_{K\perp} + 4\pi M_S - H_{dip} - H) \tag{1.2}$$

where $H_{K\perp}$ is the perpendicular anisotropy field of the free layer. Different schemes have been proposed in the literature to develop new PMA materials with low damping constant, low saturation magnetization, and good remanance. In general, rare earth transition metal alloys have PMA but they are amorphous and have high damping constant. Again, L10 FePt or FePd alloys require high deposition temperature which makes them rough.[28] Recently, Toshiba and IBM have shown significant reduction in switching current through their newly developed PMA materials.[20,28] Although specifics of these materials were not published, the goals were to lower the damping constant and improve crystalline quality of the alloy materials.

Perpendicular anisotropy can also be achieved through multilayer structure of Co, Fe or Ni. It has been shown that Co/X, Fe/X, Ni/X multilayer exhibit PMA where X is, in general, a nonmagnetic metal such as Pt, Pd, Cu, Ag, or Au. The origin of anisotropy in these structures is believed to be interface anisotropy, aided in some cases by (111) crystal orientation and strain between the layers. The exact mechanism for the anisotropy is not established but it is believed to be due to spin-orbit interaction; empirically it has been shown that for thin (couple of monolayer) Co, Fe or Ni, the interface anisotropy dominates over volume anisotropy, as shown in Figure 1.5.[29] Volume anisotropy is attributed to the crystal lattice symmetry and demagnetizing field. The PMA varies with the thickness of the FM, the ratio of the FM and non-FM thickness, and number of the bilayer in the structure. The PMA has also been observed for Co/Ni multilayer where both metals are magnetic. The theoretical calculations predict that the total number of valence electrons in Co(1 monolayer)/Ni(2 monolayer) structure positions the Fermi energy close to bands with x^2-y^2 and xy character and the spin-orbit interaction favors PMA.[30] The magnetic properties of these materials depend on growth condition, roughness, and crystal orientation. The magnetization orientation can also be tilted by varying different parameters.

1.5 Spin torque measurement using point contact technique

In order to achieve spin torque switching of an FM layer, a large current density is pushed through a small area. There are two main experimental techniques for this: point contact and nanopillar devices, as shown in Figure 1.6.[19]In nanopillar devices, at least the free layer or both the layers are patterned and etched to make structures of around 100 nm or less. Electron-beam lithography, ion milling, focused ion beam, and stencil mask are some of the techniques to define and make the pillars. The critical switching current for nanopillar devices can be less than 10^7 A/cm^2. The point contact technique, on the other hand, requires current density within 10^8-10^9 A/cm^2 for switching as the point contact has to excite a small region in an extended film.[19]In this method, an electrical contact is made on the extended substrate through a small (several nm) mechanical tip[23] or a lithographically defined contact[31]. The advantage of this structure is that the device measurements are not affected by lithography and etch-induced parameters.

Figure 1.7 shows a schematic of the mechanical point contact set-up, [32] and the details are given in Ref. 32. The point contact is made using electro-polishing of a Cu wire and contact radius of 1-10 nm can be achieved in this technique. This Cu contact is then attached to the mechanical set-up by soldering it to a leaf-spring (11). The leaf-spring is connected to a movable cylinder (3) and differential screw (2) through a metallic ball (13). The upper part of the screw is connected to the framework (1) and the lower part is connected to the cylinder. The cylinder is free to move within the framework and is connected to a spring (6) that prevents it from turning. The differential screw is rotated by a rod (4), both of which are connected through a fork blade coupling (5) to keep vibrations away from the screw. One complete rotation of the screw moves the cylinder by 25 μm. The block, including the tip and sample, is tightly connected to the framework by four screws (14). There are two spacers (9, 12) and a sample table (7) to provide a closed space and protect the components inside. The sample (8) is placed on the table and held securely by glue. The sharpened tip (10) is bent to minimize damage to the sample. The construction of the block minimizes the horizontal displacements of the tip and makes a stable point contact. However, the tip's thermal expansion doesn't allow temperature dependent measurement in this set up.[32]The radius of the point contact can be estimated using Wexler's method.[33]In this structure, the electron transport at room temperature between the contact and the substrate is assumed to be in between diffusive and ballistic regimes and contact resistance R is given as [33]:

$$R = \frac{4}{3\pi}\frac{\rho l}{a^2}\left(1 + \frac{3\pi}{8}\Gamma(K)\frac{a}{l}\right) \tag{1.3}$$

where ρ, l, a are metal resistivity, mean free path, and point-contact radius, respectively and $\Gamma(K)$ is a slowly varying function of the Knudsen number *K*, with $\Gamma(K = 0) = 1$ and $\Gamma(K = \infty) = 0.694$.

1.6 Outline

In Chapter 1, an overview is given of the nonvolatile memory market and different memory devices. The scaling issues related to this technology are discussed along with some innovative recent solutions. Spin-transfer-torque memories are explained and discussed as one of the promising solutions.

Chapter 2 discusses fabrication and device results of high density organic molecule-based nonvolatile memory. Molecular orbital energies are calculated to explain device operation. This chapter also compares different high-k dielectric oxides to improve memory operation.

Chapter 3 discusses the simulation work done on PMA spin-valve structure with different tilting of the reference layer where the free layer is magnetized in perpendicular to the plane direction. Tilting of the reference layer introduces precessional switching which requires smaller energy and shorter time to switch the free layer. However, the amount of tilting needs to be optimized. Here 90° tilting of the reference layer is not suitable, as the free layer switching is not stable in easy-axis direction.

Chapter 4 discusses fabrication, material characterization, and point contact measurement of PMA spin-valves. A seed layer was introduced to attain smooth films and (111) crystal orientation. The deposited layers were characterized using AFM, XRD, XPS, VSM, and MR measurements. Point contact measurements were done on the samples with good MR to study spin torque effect.

Chapter 5 discusses future experiments and improvements of the simulation and processing work.

1.7 References

[1]http://en.wikipedia.org/wiki/Nonvolatile_memory;http://creativecommons.org/licenses/by-sa/3.0/

[2]G. E. Moore, Int. Elec. Dev. Meeting 21, 11 (1975).

[3]S.E. Thompson, R.S. Chau, T. Ghani, K. Mistry, S. Tyagi, and M.T. Bohr, IEEE Tran. Semi. Manu. 18, 26 (2005).

[4]K.W. Guarini, C.T. Black, Y. Zhang, I.V. Babich, E.M. Sikorski, and L.M. Gignac, IEEE Int. Elect. Dev. Meeting Tech. Dig., 22.2.1 (2003).

[5]C.Y. Lu, K.Y. Hsieh, and R, Liu, Microelec. Eng. 86,283 (2009).

[6] R.F. Steimle, R. Muralidhar, R. Raoa, M. Sadd, C.T. Swift, J. Yater, B. Hradsky, S. Straub, H. Gasquet, L. Vishnubhotla, E.J. Prinz, T. Merchant, B. Acred, K. Chang, and B.E. White, Jr., Microelec. Reliability 47, 585 (2007).

[7]C.M. Compagnoni, D. Ielmini, A.S. Spinelli, and A.L. Lacaita, IEEE Trans. Elec. Dev. 52, 2473 (2005).

[8]J. Sarkar, Ph.D. dissertation,The University of Texas at Austin, Austin, TX (2007).

[9]S. Tang, C. Mao, Y. Liu, D.Q. Kelly, and S.K. Banerjee, IEEE Trans. Electron. Dev. 54, 433 (2007).

[10]I. Yamashita, Thin Solid Films 393, 12 (2001).

[11]S. Gowda, G. Mathur, Q. Li, S. Surthi, and V. Misra, IEEE Trans. Nanotech. 5, 258 (2006).

[12]C. Li,W. Fan, B. Lei, D. Zhang, S. Han, T. Tang, X. Liu, Z. Liu, S. Asano, M. Meyyappan, J. Han, and C. Zhou, Appl. Phys. Lett. 84, 1949 (2004).

[13]H. Majumdar, J. Baral, R. Osterbacka,O. Ikkala, and H. Stubb, Org. Electron. 6,188 (2005).

[14]J. Scott, and L. Bozano, Adv. Mater.19, 1452 (2007).

[15]T. Hou, U. Ganguly, and E. C. Kan, Appl. Phys. Lett. 89, 253113 (2006).

[16]Y.Y. Chen, C.H. Chien, and J.C. Lou, Jpn. J. Appl. Phys. 44,1704 (2005).

[17]C. Sargentis, K. Giannakopoulos, A. Travlos, and D.Tsamakis, Surf. Sci. 601, 2859 (2007).

[18]C. K. Maiti, S. K. Samanta, S. Chatterjee, G. K. Dalapati, and L. K. Bera, Solid state Elec. 48, 1369 (2004).

[19] D.C. Ralph, and M.D. Stiles, J. Magn. Magn. Mater. 320, 1190 (2008).

[20] T. Kishi, H. Yoda, T. Kai, T. Nagase, E. Kitagawa, M. Yoshikawa, K. Nishiyama, T. Daibou, M. Nagamine, M. Amano, S. Takahashi, M. Nakayama, N. Shimomura, H. Aikawa, S. Ikegawa,S. Yuasa, K. Yakushiji, H. Kubota, A. Fukushima, M. Oogane,T. Miyazaki, and K. Andoet, IEEE Int. Elect. Dev. Meeting Tech. Dig. 2008.

[21] J.C. Slonczewski, J. Magn. Magn. Mater. 159 (1996).

[22]L. Berger, Phys. Rev. B 54 , 9353(1996).

[23]M. Tsoi, A.G.M. Jansen, J. Bass, W.C. Chiang, M. Seck, V. Tsoi, and P. Wyder, Phys. Rev. Lett. 80, 4281 (1998).

[24]X. Zhu, PhD dissertation, Carnegie Mellon University, 2007.

[25]S. Yuasa, and D. D. Djayaprawira, J. Phys. D: Appl. Phys. 40, R337(2007). DOI: 10.1088/0022-3727/40/21/R01

[26]J. G. Zhu, Proceedings of the IEEE 96, 1786 (2008).

[27]S. Mangin, D. Ravelosona, J. A. Katine, M. J. Carey, B. D. Terris, and E. E. Fullerton, Nature Mat. 5 , 210 (2006).

[28]D. C. Worledge, G. Hu, P. L. Trouilloud, D. W. Abraham, S. Brown, M. C. Gaidis, J. Nowak, E. J. O'Sullivan, R. P. Robertazzi, J. Z. Sun, and W. J. Gallagher, IEEE Int. Elect. Dev. Meeting Tech. Dig. 2010.

[29]M. T. Johnson, P. J. H. Bloemenz, F. J. A. Broeder and J. J. Vries, Rep. Prog. Phys. 59, 1409 (1996). DOI: 10.1088/0034-4885/59/11/002

[30]G.H.O. Daalderop, P.J. Kelly, and F.J.A. Broeder, Phys. Rev. Lett. 68, 682 (1992).

[31]E.B. Myers, D.C. Ralph, J.A. Katine, R.N. Louie, and R.A. Buhrman, Science 285, 867 (1999).

[32] Z. Wei, PhD dissertation,The University of Texas at Austin, 2008.

[33] G. Wexler, Proc. Phys. Soc. 89, 927 (1966).

Table 1.1: Comparison among different nonvolatile memory structures[1]

Type	Floating gate	Magnetic	Mechanically addressed
Mechanism	Electrically program/erase	Switch magnetic domain	Contact structure
Density(Gbit/cm2)	6.7	0.0021	20.3
Access time (ms)	0.025	0.035	11
Power (w)	0.1	0.08	1.8
Data rate (Mbit/s)	23	436	540
Price per unit (Euro)	14	17.4	110
Example	Flash	MRAM	Hard disk drive

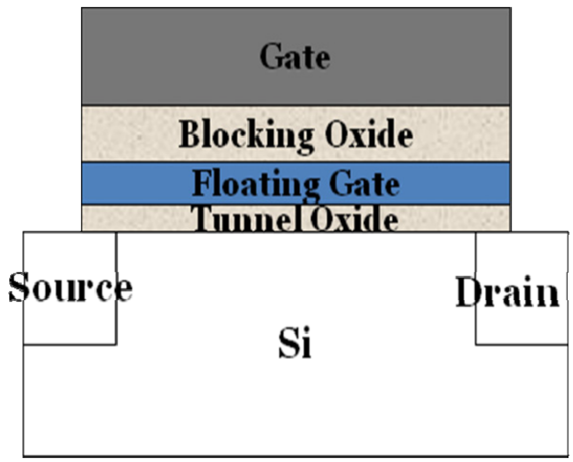

Figure 1.1: Schematic of a conventional nonvolatile memory device (not drawn to scale). Floating gate is sandwiched between a tunnel oxide and a blocking oxide. The top gate is the control gate where voltage pulses are applied.

Table 1.2[1]: Comparison of dielectric permittivity ε, conduction band offset φ_c, valence band offset φ_v, and energy band gap E_g among different dielectric materials[14]

Dielectric	Dielectric permittivity, ε	Conduction band offset, φ_c (eV)	Valence band offset, φ_v (eV)	Energy band gap, E_g (eV)
SiO_2	3.9	3.5	4.4	9
Al_2O_3	9	2.8	4.9	8.8
HfO_2	25	1.5	3.4	6
ZrO_2	20	1.4	3.3	5.8
TiO_2	80-100	1.2	-	3.05
Ta_2O_5	25	0.3	3.0	4.4

1 Reprinted from Solid-State Electronics, Vol 48, C. K. Maiti, S. K. Samanta, S. Chatterjee, G. K. Dalapati, L. K. Bera, Gate dielectrics on strained-Si/SiGe heterolayers, Pages No.1369-1389, Copyright (2004), with permission from Elsevier.

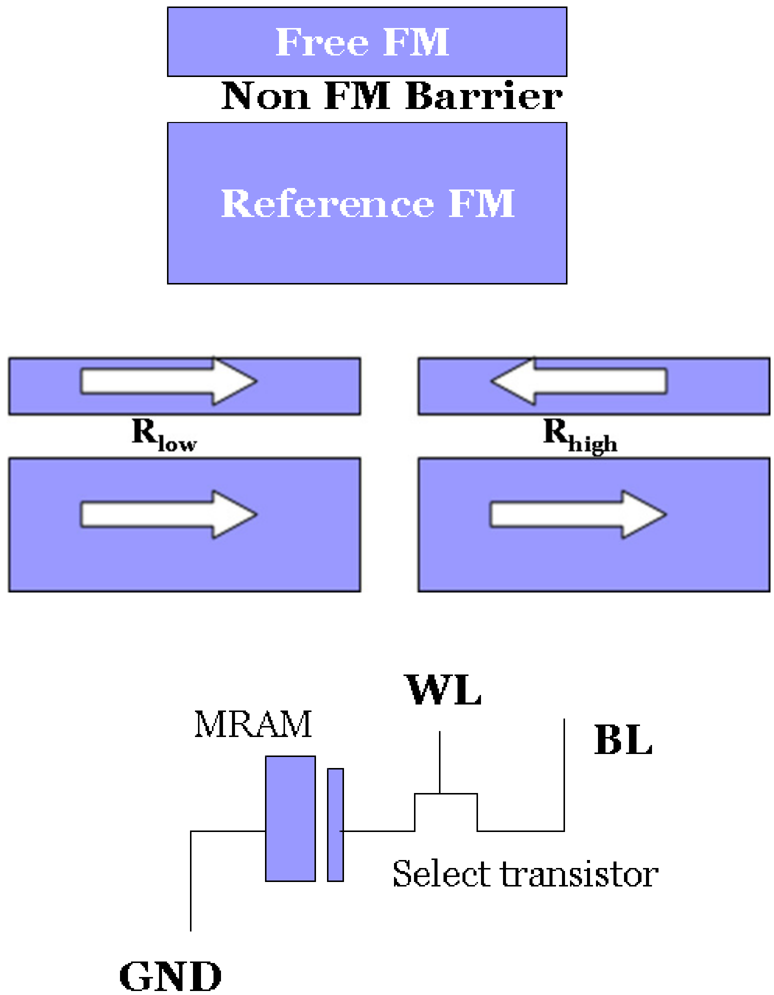

Figure 1.2: Schematic of a STT MRAM structure (top); change in resistance in an MRAM depending on magnetization direction (middle); circuit integration of a STT MRAM with a select transistor (bottom).

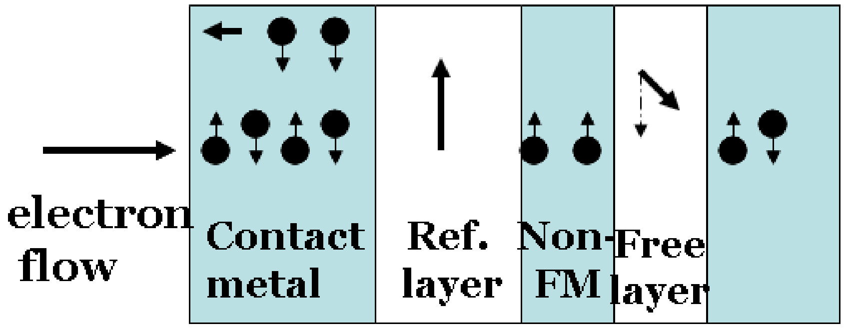

(a)

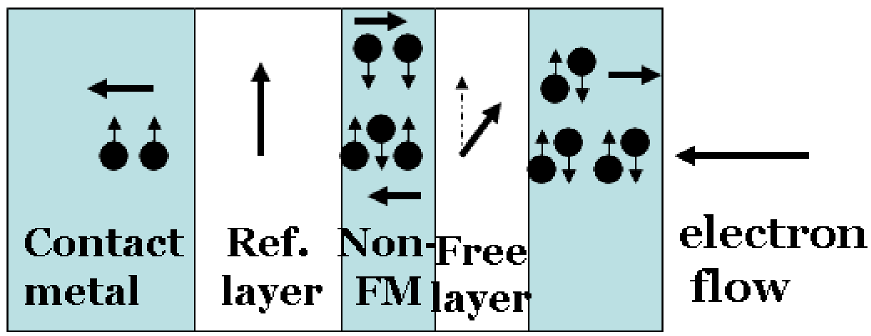

(b)

Figure 1.3: Spin-transfer-torque switching of free layer by spin polarization. As electrons pass through the reference layer, they are spin-polarized and may switch the free layer magnetization to parallel orientation (a). When electrons get reflected at the interface of reference layer/non-FM barrier they are spin-polarized in the opposite direction of the reference layer and may switch the free layer in antiparallel orientation (b).[24] Copyright (2007) by X. Zhu.

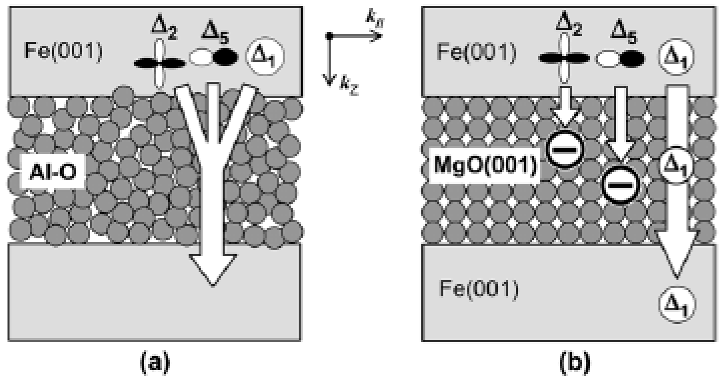

Figure 1.4: Electron transport through (a) amorphous Al_2O_3, (b) MgO(001). Crystalline (001) MgO allows coherent tunneling of Δ_1 states while blocking other states, thus improving the spin polarization and TMR.[25]

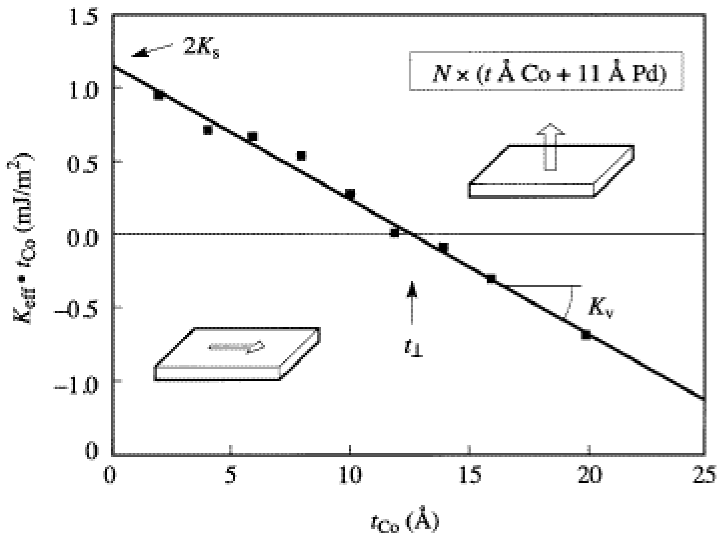

Figure 1.5: In Co/X multilayer, where X=Pt, Pd, Au, Cu, Ni etc., interface anisotropy (K_s) dominates over bulk shape anisotropy (K_v) upto a certain thickness resulting in the perpendicular magnetic anisotropy of the multilayer. [29]

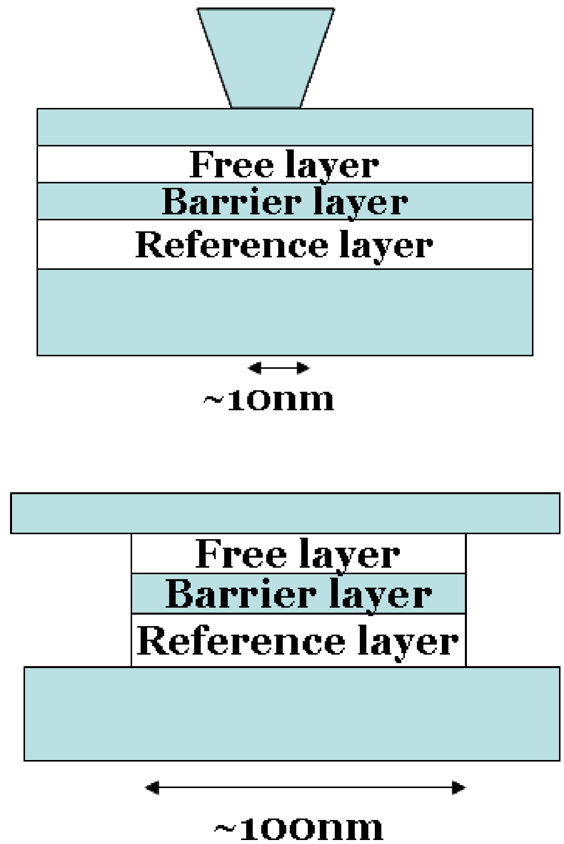

Figure 1.6: Schematics of (top) point-contact device, and (bottom) nanopillar device.[19]

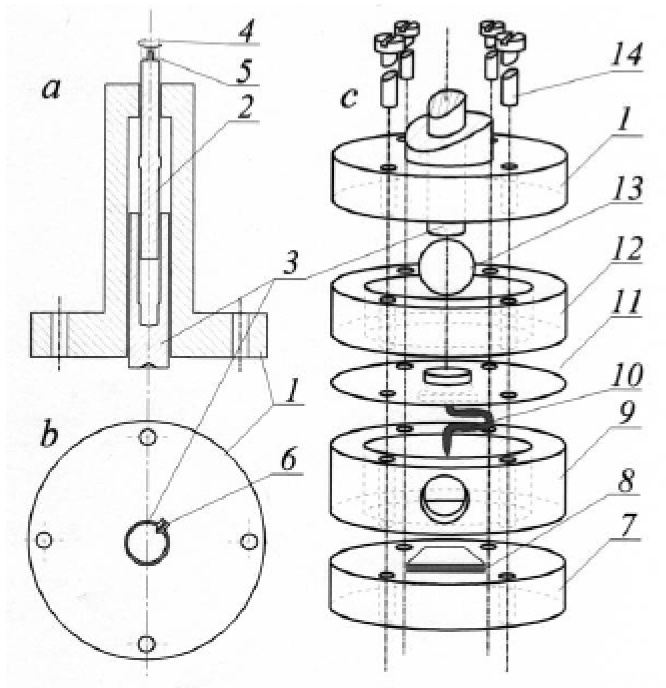

Figure 1.7: Schematics of experimental set-up for mechanical point contact measurement.[32] Details are given in Ref. 32. Copyright (2008) by Z.Wei.

Chapter 2: Fullerene-based Hybrid Devices for High Density Nonvolatile Memory

This chapter presents a CMOS-compatible, nonvolatile, hybrid memory device using fullerenes as a floating gate. In the hybrid MOSCAPs, organic fullerene molecules were encapsulated between inorganic oxides, i.e. SiO_2 as a tunnel oxide and HfO_2 as a control oxide. Aluminum was e-beam deposited on the fullerenes and oxidized to act as a nucleation layer for the HfO_2 control oxide. Material characterization confirmed the presence of fullerenes and high-k dielectric in the gate stack. Electrical characterization verified the memory operation of the devices. Finally, the molecular orbital energies of fullerene molecules in the gate stack were estimated.[2]

2.1 Device Fabrication

The MOS capacitors were fabricated on lightly doped (10^{15} cm^{-3}) p-type silicon (Si) wafers with a ~3.6 nm silicon dioxide (SiO_2), grown using thermal oxidation or rapid thermal oxidation (RTO), as a tunnel oxide. The fullerene solution was prepared in toluene (0.5 mg/ml) and sonicated for several hours, then spin coated on SiO_2 to create a uniform film. The spin coating speed was optimized to deposit a thin layer of molecules. Fullerene molecule (C60) was chosen among the available organic molecules because C60 molecules have multiple charge storage levels, high thermal stability (~400°C), and are easily assembled on dielectric oxides. After deposition, the samples were baked in air at 200°C to remove the toluene. A thin Al film, ~3nm, was then e-beam evaporated on fullerenes and oxidized. A thin film of HfO_2 , ~13 nm, was deposited on the Al-O nucleation layer by atomic layer deposition (ALD) as a control oxide followed by a post

---

[2] Part of this chapter is © [2010] IEEE. Reprinted, with permission, from [F. Ferdousi, M. Jamil, H. Liu, S. Kaur, D. Ferrer, L. Colombo, and S. K. Banerjee, Fullerene-Based Hybrid Devices for High-Density Nonvolatile Memory, IEEE Transaction on Nanotechnology, in press].

deposition anneal at 400°C in N_2 ambient. Physical vapor deposition of ~200nm TaN completed the gate stack and photolithography, followed by reactive ion etching (RIE) was done to define capacitor areas from 100μm×100μm to 300μm×300μm. Figure 2.1 is a schematic of the fabricated capacitors.

2.2 Results and Discussion

X-ray photoelectron spectroscopy (XPS) analysis was used to analyze the various materials and Table 2.1 shows a summary of the film component peak position and the relative peak area. The dominant C 1s peak corresponds to fullerene[1] molecules deposited between SiO_2 and HfO_2 layers. The other C 1s peaks correspond to different C-O bonds. Further, no Al-C, Hf-C or Si-C peaks were observed.[2]In the sample with Al, the thin Al layer was mostly oxidized to aluminum oxide (Al_2O_3). On the other hand, the sample without Al layer shows hafnium silicate ($HfSiO_x$) peaks as well as HfO_2 peaks. The data support following conclusions: 1) fullerene was self-assembled on dielectric oxide and 2) high-k dielectric may be deposited through ALD on fullerene with a thin interfacial layer, despite the low chemical reactivity of fullerenes. The oxidized Al layer presumably improves the interface between fullerene and HfO_2, hence reducing traps and improving memory operation. The MOS devices with Al_2O_3 showed a comparable memory window as that of the devices without Al_2O_3 at smaller average effective fields. In addition, the thin Al_2O_3 layer increases effective oxide thickness and breakdown voltage of the capacitors.

During P/E characterization, the capacitors exhibited a memory window in the form of a flat-band shift. The devices were stressed by 6-11V pulses for durations of 100-1000 ms. A flat-band shift of ~0.8V was observed under ± 10V stress for 500 ms as shown in Figure 2.2 which corresponds to a charge density of 7.67×10^{-7} C·cm^{-2} and a stored electron density of 4.79×10^{12} cm^{-2}. The stretch-out in the erase C-V is believed to be caused by traps in the potential well at the HfO_2/Al_2O_3 interface. The devices without fullerene showed a smaller shift, ~0.05V, under the same condition. The memory window of fullerene MOS capacitors increased exponentially with increasing effective field across the tunnel oxide (E_{eff}), as shown in Figure 2.3(a). This indicates that the programming mechanism is Fowler-Nordheim (FN) tunneling through the tunnel oxide and the erase mechanism depends on FN tunneling at high fields. Moreover, the introduction of high-k dielectric as a control oxide improves cell coupling capacitance between the control gate and floating gate resulting in an improved memory operation.[3] Figure 2.3(b) presents flat band shift with P/E time, which shows that the memory window did not saturate up to 1s of pulse duration. Program/erase speed may be further enhanced by band-engineering the tunnel oxide layer.[4]

The endurance test was carried out at ± 10V stress for 500ms. During endurance test, the devices suffered flat-band deviation after 10^4 P/E cycles although a 0.5V memory window was maintained even after 10^5 cycles of operation. The reason for V_{FB} shift may be the poor quality of SiO_2. In addition, the retention test was carried out at 293K, 328K, and 358K. The MOS capacitors suffered a charge loss of about 22% at 293K after 6.2×10^4s. However, the charge loss is aggravated at high temperatures.

In order to calculate the energy band diagram of fullerene MOS devices, the lowest unoccupied molecular orbital (LUMO) energy of fullerene was calculated and the data is shown in Table 2.2 for SiO_2, Al_2O_3, and HfO_2 dielectrics following the theoretical models given in literature.[5,6] Interestingly, charge storage levels in fullerene may be changed by employing different encapsulating oxides. The orbital energies in HfO_2, for the first, second, third and fourth charge states are close to 4.9 eV. Because of the very small difference among these charge states, C-V plots of fullerene in HfO_2 are expected to be continuous as the experimental data show in Figure 2.2. Furthermore, Figure 2.4

shows Arrhenius plot of retention time of fabricated fullerene devices versus temperature (T).[7] The strong temperature dependence indicates trap-assisted tunneling rather than band-to-band tunneling through tunnel oxide during retention; as a result, retention is poor. Further, the 1/T dependence of retention time at high temperature indicates fixed-range hopping conduction,[8] as shown in equation

$$\ln \Delta Q - \ln \Delta t \propto -{\Delta Ea}/{kT} \tag{2.1}$$

For fixed range hopping conduction, the slope of Arrhenius plot corresponds to the energy difference between initial and final charge states. In fullerene capacitors, electrons are presumably tunneling from the LUMO in fullerene to the conduction band in Si. The energy level of electrons in fullerene devices is estimated to be ~4.52 eV, in agreement with the LUMO value calculated in Table 2.2. Figure 2.5 presents energy band diagram of the gate stack with the estimated orbital energy value of fullerene. From the device data it can be concluded that P/E mechanism in fullerene devices is FN tunneling; however, retention is limited by trap-assisted tunneling.[9]

2.3 Comparison of high-k insulating oxides in a memory structure

Conventional memory devices have the same dielectric oxide as the tunnel and control oxides. The effective field across tunnel oxide, F_1, can be increased by using a high-k dielectric as a control oxide and SiO_2 as a tunnel oxide which will increase the memory window and improve P/E speed. Program/erase speed may be further enhanced by band engineering the tunnel-oxide layer.[4] The introduction of high-k dielectric as a control oxide improves cell-coupling capacitance between the control gate and floating gate resulting in an improved memory operation.[3] The effective field across tunnel oxide, F_1, is given in Ref. 10 as

$$F_1 = \frac{\varepsilon_2 V_G}{\varepsilon_1 t_2 + \varepsilon_2 t_1} \tag{2.2}$$

where $\varepsilon_{1,2}$ is the dielectric constant of the oxides, $t_{1,2}$ is the thickness of the oxides, F_1 is the electric field across tunnel oxide, and V_G is the applied pulse amplitude. Again, F_1 is expressed in terms of conduction band offset of the dielectrics in Ref. 11 as

$$F_1 = \frac{V_G}{t_1 + t_2 (\frac{\phi_{B2}}{\phi_{B1}})^{3/2}} \tag{2.3}$$

where $\phi_{B1,2}$ is the conduction band offset of the oxides with respect to Si. Figure 2.6 shows a contour plot of equation (2.3) where the band offset and the thickness ratio are varied. A thin control oxide with a low conduction band offset will improve F_1, however, at the expense of retention. Although equation (2.2) and (2.3) express F_1 in terms of permittivity and band offset separately, both these parameters are important for memory operation. The memory window as the difference in threshold voltage during P/E, ΔV_t, is given as: [11]

$$\Delta V_t = -R * V_G \frac{1-ab}{ac+ab} \tag{2.4}$$

where $a = \varepsilon_2 / \varepsilon_1, b = (\phi_{B2} / \phi_{B1})^{3/2}, c = t_1 / t_2$; R is less than unity and accounts for the non-uniform distribution of discrete charge in the floating gate. Figure 2.7 and 2.8 show ΔV_t with varying parameters. In Figure 2.7 SiO_2/Al_2O_3 combination shows larger memory window due to larger conduction band offset of Al_2O_3. On the other hand, Al_2O_3/HfO_2 suffers from low permittivity as well as band offset ratio. As control oxide is thinned down, memory window decreases since tunneling currents through the oxides become similar. The difference in ε_1 and ε_2 provides different injection and emission currents through the tunnel and control oxides which helps to enhance the memory window. Again, reasonable conduction/valence band offsets of control oxide are necessary for retention as well as memory window maintenance as shown in Figure 2.8. If the band offset is small, injection from control gate or emission from discrete charges to control gate will be high. This tunneling will degrade the memory window and retention. For most high-k materials, the improvement of higher permittivity is diminished by low conduction/valence band offsets. The smaller the band offset, the narrower the operating range of memory devices due to the overlapping of injection/emission currents through oxides.[11] In order to use high-k materials with small band offsets, the thickness of the control oxide has to be large enough to prevent electron tunneling across the control gate. This limitation not only reduces scalability but also increases the effective oxide thickness (EOT) of the gate structure.

2.4 Summary

In summary, hybrid fullerene MOS capacitors were fabricated in a CMOS-compatible process flow and material as well as electrical characterization was carried out. The MOS capacitors demonstrate nonvolatile memory operation at room temperature. From the device data it can be concluded that P/E mechanism in fullerene devices is FN tunneling; however, retention is determined by trap-assisted tunneling. Molecular orbital energies associated with the charge states in different dielectric environments were calculated to explain the device performance. Different high-k dielectric oxides were compared to optimize the memory operation.

2.5 References

[1]L. Chiang, J. Swirczewski, C. Hsu, S. Chowdhury, S. Cameron, and K. Creegan, J. Chem. Soc. , Chem. Commun., 1791(1992).

[2]A. Pirkle, R. M. Wallace, and L. Colombo, Appl. Phys. Lett. 95, 133106 (2009).

[3] F. Ferdousi, J. Sarkar, S. Tang, D. Shahrjerdi, T. Akyol, E. Tutuc, and S.K. Banerjee, J. Elec. Mat. 38, 438 (2009).

[4]D.C. Gilmer, N. Goel, H. Park, C. Park, S. Verma ,G. Bersuker, P. Lysaght, H.H. Tseng, P.D. Kirsch, K.C. Saraswat, and R. Jammy, IEEE Int. Elec. Dev. Meet. Tech. Dig. 2009.

[5]W. Green, S. Gorun, G. Fitzgerald, P. Fowler, A. Ceulemans, and B. Titeca, J. Phys. Chem. 100, 14892 (1996).

[6]U. Ganguly, C. Lee, and E. C. Kan, MRS Proc. NI6.3.1 (2004).

[7]Y. Liu, S. Tang, and S. K. Banerjee, Appl. Phys. Lett. 88, 213504 (2006).

[8]M. Okutan, H.I. Bakan, K. Korkmaz, and F. Yakuphanoglu, Physica B 355, 176 (2005).

[9]F. Ferdousi, M. Jamil, H. Liu, S. Kaur, D. Ferrer, L. Colombo, and S. K. Banerjee, IEEE Tran. Nanotech. (in press). This material is posted here with permission of the IEEE. Such permission of the IEEE does not in any way imply IEEE endorsement of any of the products or services of The University of Texas at Austin. Internal or personal use of this material is permitted. However, permission to reprint/republish this material for advertising or promotional purposes or for creating new collective works for resale or redistribution must be obtained from the IEEE by writing to pubs-permissions@ieee.org. By choosing to view this material, you agree to all provisions of the copyright laws protecting it. If applicable, University Microfilms, Inc. and/or ProQuest may supply single copies of the dissertation.

[10]C. Sargentis, K. Giannakopoulos, A. Travlos, and D. Tsamakis, Surf. Sci. 601, 2859 (2007).

[11]C.M. Compagnoni, D. Ielmini, A.S. Spinelli, and A.L. Lacaita, IEEE Trans. Electron. Dev. 52, 2473 (2005).

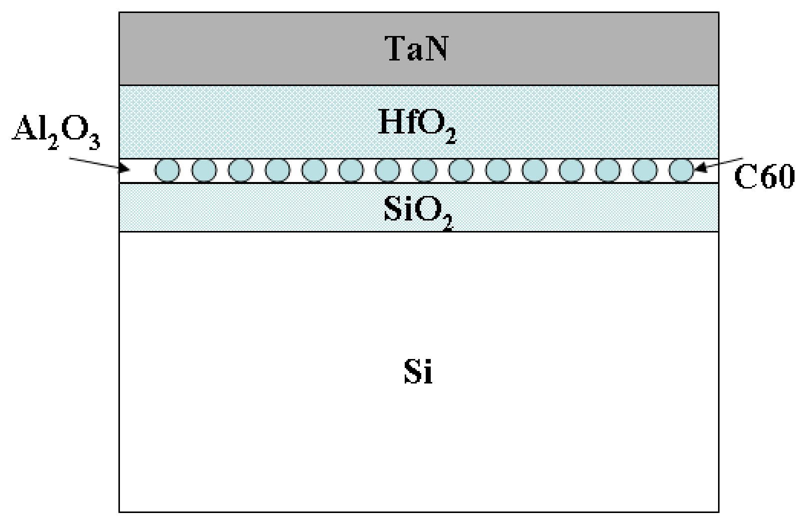

Figure 2.1: Schematic of the fabricated MOS capacitors (not drawn to scale).[9]

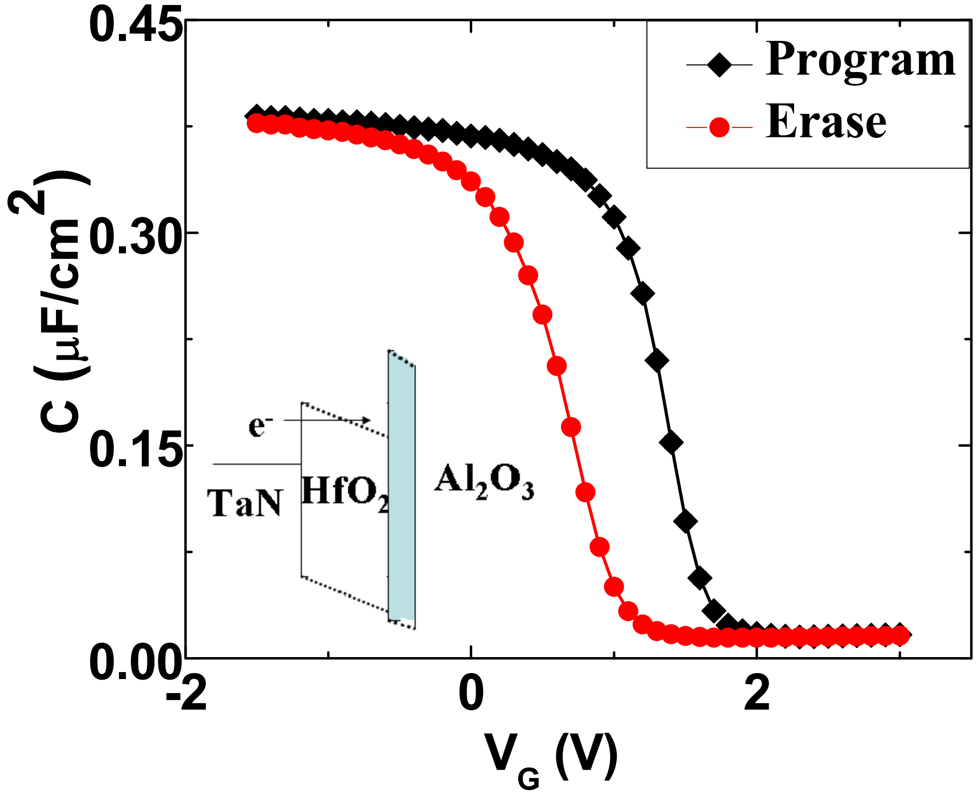

Figure 2.2: High frequency C-V characteristics of hybrid MOS capacitors under ±10V stress for 500ms. The memory window corresponds to a trapped electron density of 4.79×10^{12} cm^{-2}. The stretch in erase C-V is due to the traps at the HfO_2/Al_2O_3 interface. Inset shows a schematic diagram of the control oxide under erase condition.[9]

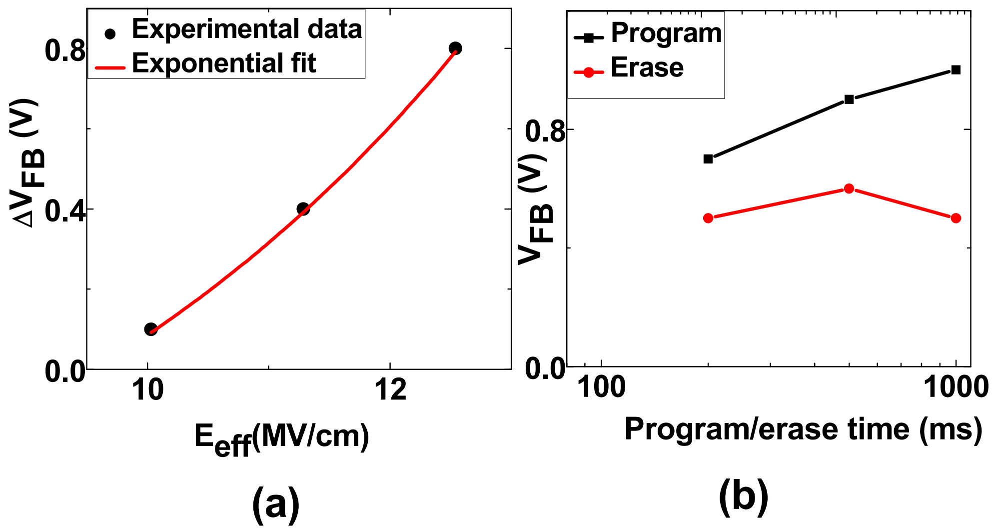

Figure 2.3: (a) Flat-band voltage shift with increasing effective field across tunnel oxide for 500ms stress. ΔV_{FB} shows exponential dependence with effective field indicating FN tunneling. (b) Flat-band voltage shift with program/erase time at 9V stress. Memory window increases as program/erase time increases.[9]

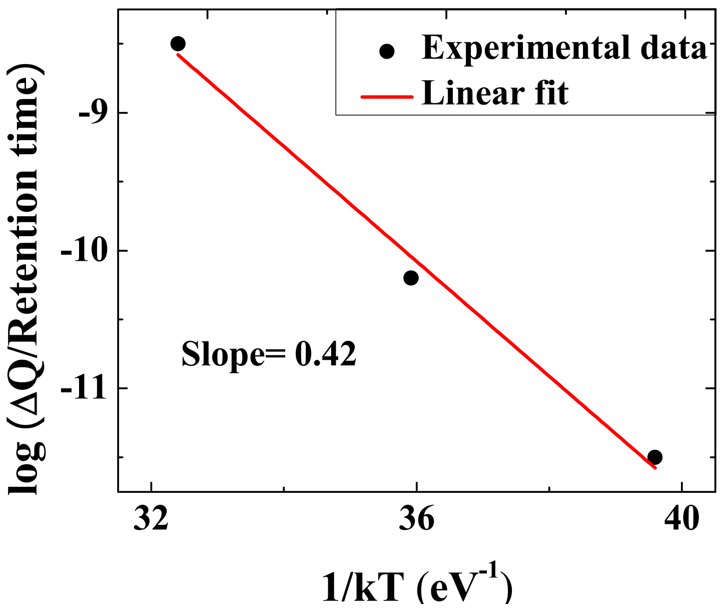

Figure 2.4: Arrhenius plot showing ΔEa=0.42eV between the LUMO of fullerene and the conduction band of Si. The empirically obtained LUMO is 4.52 eV which agrees with the theoretically calculated LUMO for fullerene in HfO_2. Retention time was chosen as ~19% charge loss time at 293K, 328K, and 358K. [9]

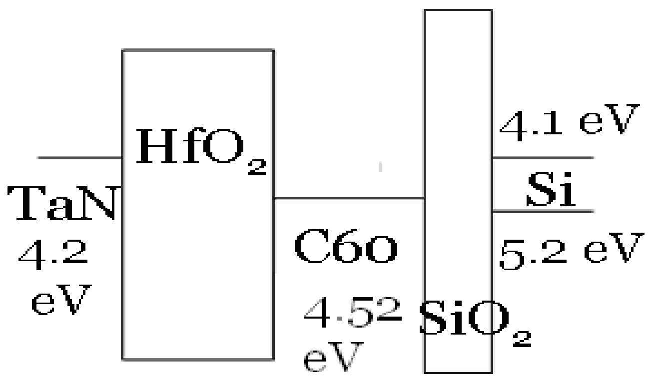

Figure 2.5: Energy band diagram of the gate stack in MOS capacitors.[9]

Table 2.1: XPS peak positions for C, Al, Hf in the gate stack[9]

Sample 1: with Al IL		
	Binding Energy(eV)	%Area
C 1s	286.42	51.46
	287.99	18.5
	287	17.37
	290.41	12.67
Hf 4f	18.77	55.76
	20.42	44.24
Al 2p	76.48	94.38
	75.68	5.62

Sample 2: without Al IL		
	Binding Energy(eV)	%Area
C 1s	286.43	70.71
	287.79	15.45
	290.13	13.84
Hf 4f	18.49	40.29
	20.49	23.40
	20.04	19.45
	18.94	16.86

Table 2.2: Calculated MO energy of fullerene [5,6,9]

Charge State	LUMO in Vacuum (eV)	Corrected LUMO in SiO_2 (eV)	Corrected LUMO in HfO_2 (eV)	Corrected LUMO in Al_2O_3 (eV)
0	-4.76	-4.76	-4.76	-4.76
1	-1.77	-4.27	-4.83	-4.6
2	1.29	-3.71	-4.83	-4.37
3	4.28	-3.22	-4.9	-4.21
4	7.31	-2.69	-4.93	-4.01
5	10.3	-2.2	-5	-3.85

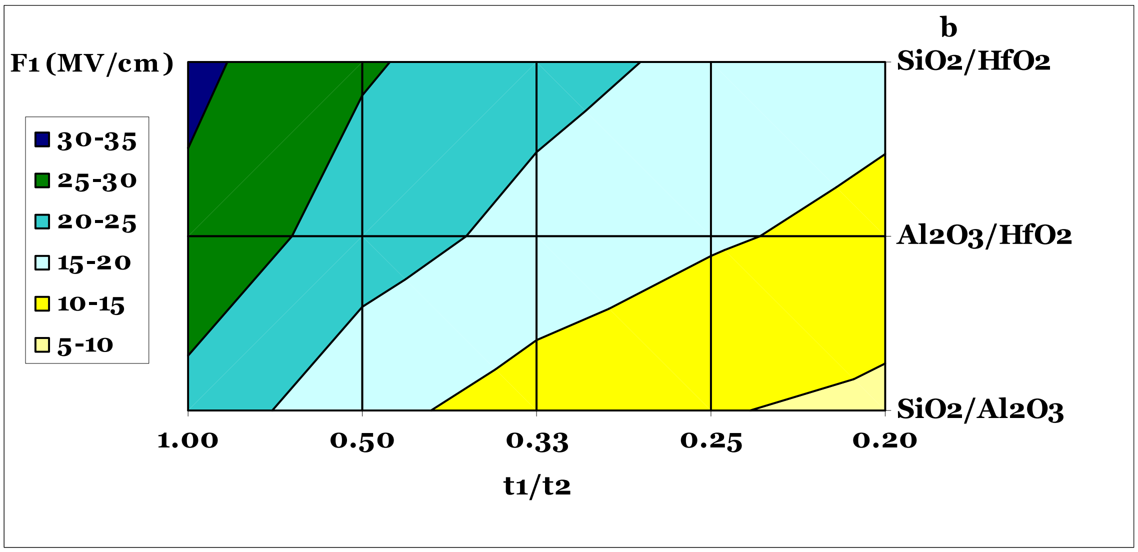

Figure 2.6: Effective field across tunnel oxide, F_1, as $b = (\phi_{B2} / \phi_{B1})^{3/2}$ and the thickness ratio are varied. A thin control oxide with small conduction band offset will have high F_1, at the expense of retention.

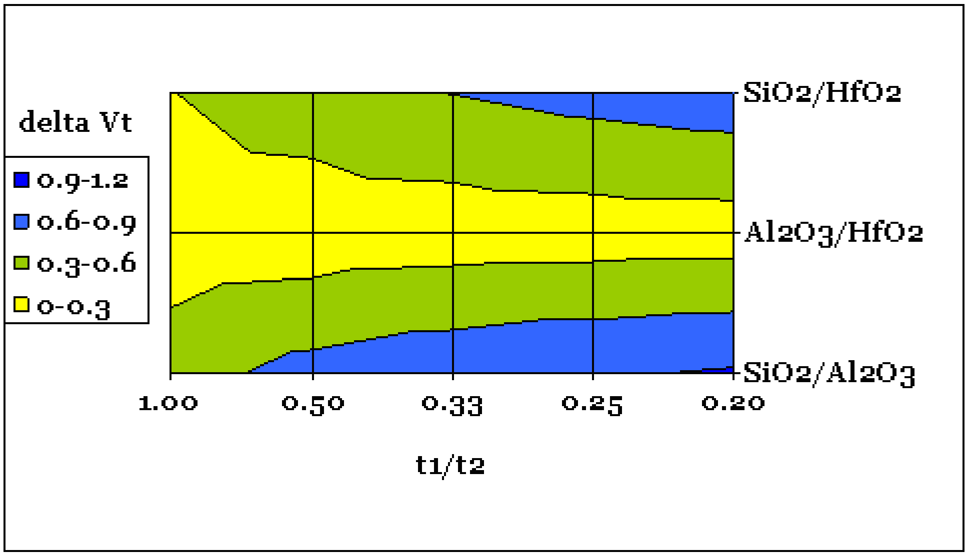

Figure 2.7: Memory window as $a = \varepsilon_2 / \varepsilon_1, b = (\phi_{B2} / \phi_{B1})^{3/2}, c = t_1 / t_2$ are varied. SiO_2/Al_2O_3 shows larger memory window. Al_2O_3/HfO_2 suffers from low a, and b. As control oxide is thinned down, memory window decreases since tunneling currents through the oxides become similar.

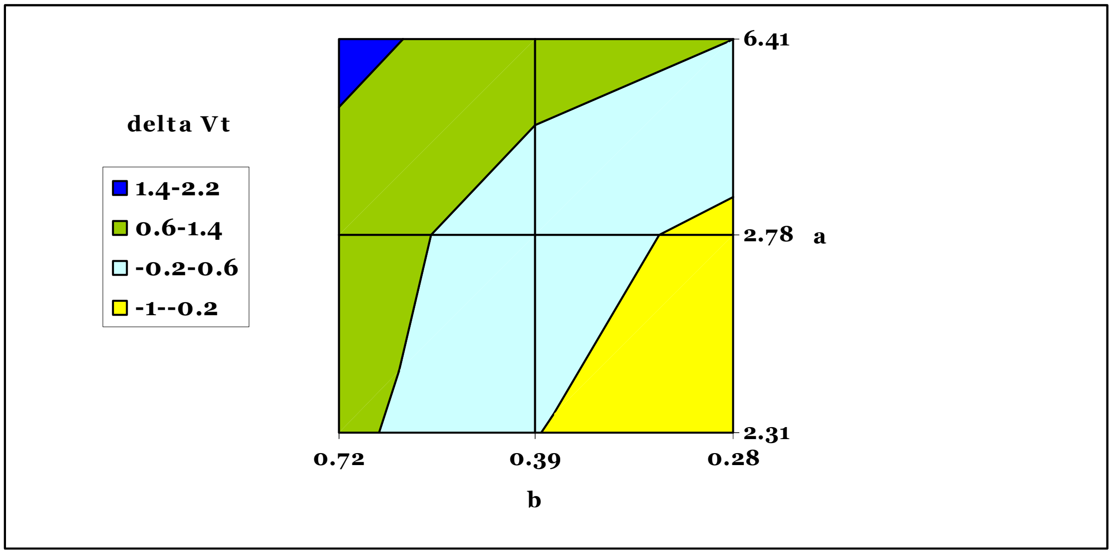

Figure 2.8: Memory window as $a = \varepsilon_2 / \varepsilon_1, b = (\phi_{B2} / \phi_{B1})^{3/2}$ are varied for a fixed $t_1 / t_2 = 0.33$. Memory operation improves when both a, b are enhanced through oxide engineering.

Chapter 3: Micromagnetic Simulation of STT Memory Device

This chapter discusses micromagnetic simulations of magnetic materials and STT devices. The simulations were carried out to optimize material parameters and device structures. The effect of precessional switching in reducing critical current and switching time was investigated.

3.1 Spin-transfer-torque: A brief overview

Figure 3.1 gives a simple overview of STT effect on an FM layer. At a certain effective field, the magnetization of an FM layer is assumed to be oriented at a small angle from the effective field. When a spin torque acts on the layer, three things can happen depending on the strength of the torque. If the applied torque is small, then the FM layer magnetization can exhibit a damped motion about the initial direction. When the torque is high, the FM layer magnetization can exhibit either stable precession at a certain angle or switch to the opposite direction.[1] Magnetization dynamics of a FM layer in presence of spin polarized current at zero temperature is described by the Landau-Lifshitz-Gilbert (LLG) equation with the spin torque term and field like torque term as : [1,2,3,4,5]

$$\frac{d\vec{m}}{dt} = -|\gamma|\vec{m} \times \vec{H}_{eff} + \alpha\left(\vec{m} \times \frac{d\vec{m}}{dt}\right) + |\gamma|\beta\varepsilon\left(\vec{m} \times \vec{m}_p \times \vec{m}\right) - |\gamma|\beta\varepsilon'\vec{m} \times \vec{m}_p \tag{3.1}$$

where $\vec{H}_{eff}$ is the effective field, γ is the Gilbert gyromagnetic ratio, α is the damping constant, $\vec{M}$ is the magnetization in A/m, M_s is the saturation magnetization in A/m, $\vec{m}$ is M/Ms, $\vec{m}_p$ is the (unit) electron spin polarization direction, and $\beta = \left|\frac{\hbar}{\mu_0 e}\right| \frac{J}{tM_s}$, e is electron charge in C, J is current density in A/m^2, t is the free layer thickness in meters, $\varepsilon = \frac{P\Lambda^2}{(\Lambda^2 + 1) + (\Lambda^2 - 1)(\vec{m} \bullet \vec{m}_p)}$, ε' is the secondary spin transfer term, P is spin polarization factor. The first term of the right hand side of the equation denotes precession due to the effective field, the second term denotes damping effect, the third term is the spin-transfer-torque term and the fourth term is field-like torque. The first two terms come from LLG equation and express magnetization dynamics of any FM layer in presence of a field. The spin transfer term depends on the current density, polarization, and the angle between the free and fixed layers. Here, $\Lambda^2 = GR$ where R is the total effective resistance of spin-up and spin-down electrons between the spacer and reservoir and G is the conductance given as $G = Se^2 k_F^2 / 4\pi^2\hbar$ where k_F is the Fermi wave vector and S is the cross-sectional area of the device. The effective resistance includes the effects of resistive scattering, spin-flip scattering and interface scattering.[4] Field like torque (FLT) depends on the direction of magnetization of the reference layer and current flow. The term $\vec{m} \times \vec{m}_p$ creates a precessional motion of the free layer magnetization and it is found to be about 30% of the spin transfer torque experimentally.[6]This is different from charge current induced fields since the charge current field does not depend on the direction of reference layer. Field-like torque can be important in precessional switching especially with non-collinear magnetization of the free and reference layers.[7]

3.2 Tilted spin polarization to enhance STT switching

Different schemes have been proposed in the literature to reduce critical switching current of spin-valve or MTJ devices. One of the methods is to have a dual spin-valve structure with two reference layers sandwiching a free layer. The magnetizations of the reference layers are oriented in the opposite directions which increase the number of spin-polarized electrons passing through the free layer for the same current density with only one reference layer.[8] Simulation studies have shown that non-collinear magnetization results in smaller energy and shorter time for STT structures with in-plane materials as a result of precessional switching.[7,9] However, the tolerance of switching is small for 90° tilt of reference layer in out-of-plane direction compared to the in-plane reference layer. The amount and direction of tilting need to be optimized, especially at different damping constants. Another method involves a tapered nanopillar structure with in-plane materials where the spin current has a component with out-of-plane polarization maximized along the major axis of the elliptical device.[10]However; this device structure requires an aspect ratio of greater than one which impedes high density fabrication. Dual spin-valve structure has been fabricated where one reference layer is magnetized in-plane and the other out-of-plane to introduce tilted spin polarization of the in-plane free layer.[11]This design improves switching time but results in a discontinuous switching region. Another disadvantage of this structure is that the amount of tilt is not easily controlled. In another design, the free layer was out-of-plane while the two reference layers were in-plane and out-of-plane as before.[12]In this design, the retention energy of the free layer was reduced from single spin-valve structure probably due to the biasing effect of the in-plane reference layer. Another disadvantage of the dual spin-valve structure is that the damping constant of the free layer can not be optimized through cap layer engineering.[13]This chapter investigates the effect of non-collinear magnetization in PMA spin-valves through micromagnetic simulation for a single spin-valve structure. Chapter 4 describes fabrication techniques to introduce tilted spin polarization in a single spin-valve through tilted reference layer.

3.3 Micromagnetic simulation of PMA spin-valve

Magnetization dynamics of PMA spin valves were studied through micromagnetic simulations[5] where the magnetization direction of the reference layer is varied between 0 to 45 degrees in the direction perpendicular to the plane of the sample.

The perpendicular to the plane direction is z-axis; the long axis of the ellipse is x-axis and the short axis is y-axis as shown in Figure 3.2. At first, 2D simulations were carried out to optimize the saturation magnetization and aspect ratio of long (x) axis and short (y) axis of the elliptical structure as shown in Figure 3.3 and 3.4 respectively. Lowering the saturation magnetization improves PMA and is expected to lower critical current. On the other hand, no significant difference was observed for different aspect ratios of the elliptical structure once the material parameters were optimized. The dimension of the elliptical spin-valve was 90nm x 40nm and the material parameters for Co/Pt PMA multilayer were chosen as following: saturation magnetization, Ms= $4x10^5$ A/m, damping constant, α=0.1, crystalline anisotropy constant, K1= $1.1x10^5$ J/m^3 for free layer and $6.6x10^5$ J/m^3 for reference layer.[14,15] The in-plane layer is simulated with the following parameters: Ms=$1450x10^3$ A/m and K1= $5.2x10^5$ J/m^3.Thermal effect was not included and no exchange bias was assumed between the layers; field like torque was assumed to be 30% of spin torque.[6,7] The material parameters and switching conditions were chosen such that only the free layer was switched and the reference layer kept its initial magnetization direction during simulations. As the magnetization direction of reference layer is tilted from 0 to 45 degree, the critical switching current density for a 2 ns pulse reduces by 37%. Similarly for a fixed current density of $5x10^{11}$ A/m^2, the switching time for parallel to antiparallel (P→AP) transition improves by 49% while that for antiparallel to parallel (AP→P) transition improves by 33%, as shown in Table 3.1. During P→AP transition, the free layer switches against the effective field from reference layer, so the switching time is longer than AP→P transition. Figure 3.5 shows an M-H loop of the free layer with 0° tilt of reference layer. Figure 3.6 shows free layer switching with an applied current pulse in time domain where little precession is observed in either x, y, or z direction. Figure 3.7 shows the same for 45° tilt and figure 3.8 shows the same for an in-plane reference layer with 90° tilt. With 45° tilt, precession of the domains are observed in x, y, and z direction. For 90° tilt with in-plane reference layer, the free layer switches as soon as the negative current pulse is applied, then switches back to +z direction once the pulse is stopped, so the switching from P→AP direction is not stable. Then, when the positive pulse is turned off, the domains oscillate in z direction and finally stabilizes away from +z or -z direction. Single pulse switching for this orientation is not applicable and requires additional switching technique.

Figure 3.9 shows magnetization dynamics of a PMA spin-valve with tilting of (a)0°, (b)15°, (c) 25°, (d) 45°, (e) 90° with in-plane free layer and perpendicular reference layer, and (f) 90° with in-plane reference layer and perpendicular free layer for a 2 ns current pulse of $5x10^{11}$ A/m^2 . The magnitude of precession at different tilting can be compared from these plots. For 0° tilting, the precession is negligible, so a higher current or longer time is needed to provide enough energy to switch the free layer. For 15°, 25°, and 45° tilting, the AP→P switching paths are similar but the paths for P→AP transition change with tilting angle. All these switching are in out-of-plane direction, mainly through oscillating in x and z directions. The initial starting torque is not large enough to switch the free layer. As the domains start to oscillate the torque increases and finally switches the domains in the opposite direction. The trajectory of the switching path probably depends on at which point of precession the switching occurs. For 90° tilt with in-plane free layer and PMA reference layer, a number of precessions occur mainly in xy plane before the free layer is switched, requiring high energy to switch. For 90° tilt with in-plane reference layer and PMA free layer, the free layer stabilizes at a certain orientation different from +z or –z axis with any current pulse, so switching is not accomplished. Figure 3.10 shows energy plot vs free layer magnetization for different tilt angle of the reference layer. The demagnetization and uniform exchange energies are reduced as tilting changes from 0° to 45°, which also reduces the total energy. Demagnetization energy is expected to be lowest when magnetization points along the longest axis of a nanomagnet, and highest when magnetization points along the shortest axis. Since the shortest axis is z-axis, demagnetization energy decreases with increasing tilting and for a certain tilting, as magnetization points away from +z or –z orientation during switching. At 0° tilt, the domains are mostly pointing at +z or –z until switching resulting in higher exchange energy among domains. Whereas with tilting the domains point at different directions resulting in a smaller exchange energy. The uniaxial anisotropy energy is almost similar among the devices. Total energy is still minimum at +z or –z orientation which allows the free layer to switch and stabilize. When the reference layer is in-plane, the total energy becomes fixed for any z and no switching is observed. For in-plane free layer, the demagnetization energy is minimum at +x or –x and increases for in-between orientations. The uniform exchange energy is also higher resulting in a higher total energy for the device resulting in a high switching current.

Figure 3.11 through 3.13 show trajectory of magnetization of the free layer, with and without tilting of the reference layer, at a critical switching current density without FLT. Trajectories are shown with FLT, without FLT and when the damping constant is halved to 0.05. For 0° tilting, there is no observable difference in the trajectories but the switching becomes faster at the same current density with FLT and lower damping constant, as expected. For tilted polarization, changing FLT and damping constant changes the switching trajectory. Field-like-torque aides the STT here and as a result less number of precessions are needed to switch. For a different damping constant, the precession follows a different path since lowering the damping constant enhances the STT. Example codes for STT switching are given in Appendices 1 and 2.

3.4 Summary

This chapter discussed the simulation work done on PMA spin-valve structure with different tilting. Tilting of the reference layer introduces precessional switching which requires smaller energy and shorter time to switch the free layer. However, the magnitude and direction of tilting need to be optimized for memory operation. Here 90° tilt with in-plane reference layer is not suitable as the free layer switching is not stable in easy axis direction.

3.5 References

[1]D.C. Ralph, and M.D. Stiles, J. Magnetism and Magnetic Mat. 320, 1190 (2008).

[2]T. L. Gilbert, Phys. Rev.100, 1243 (1955).

[3]L. Landau, and E. Lifshitz, Physik. Z. Sowjetunion 8, 153–169 (1935).

[4]J. Xiao, A. Zangwill, and M. D. Stiles, Phys. Rev. B 70, 172405 (2004).

[5]M. J. Donahue, and D. G. Porter, OOMMF User's Guide, Version 1.0, National Institute of Standards and Technology Report No. NISTIR 6376, September 1999 (unpublished).

[6]M. A. Zimmler, B. Ozyilmaz, W. Chen, A. D. Kent, J. Z. Sun, M. J. Rooks, and R. H. Koch, Phys. Rev. B 70, 184438(2004).

[7]D. E. Nikonov, G. I. Bourianoff, G. Rowlands, and I. N. Krivorotov, J. App. Phys. 107, 113910 (2010).

[8]L. Berger, J. Appl. Phys. 93, 7693 (2003).

[9]A. D. Kent, B. Ozylimaz, and E.D. Barco, Appl. Phys. Lett. 84, 3897 (2004).

[10]P. M. Braganca,O. Ozatay, A. G. F. Garcia, O. J. Lee, D. C. Ralph, and R. A. Buhrman, Phys. Rev. B 77, 144423 (2008).

[11]O. J. Lee, V. S. Pribiag, P. M. Braganca, P. G. Gowtham, D. C. Ralph, and R. A. Buhrman, Appl. Phys. Lett. 95, 012506 (2009).

[12]R. Law, E.L. Tan, R. Sbiaa, T. Liew, and T. C. Chong, Appl. Phys. Lett. 94, 062516 (2009).

[13]C.L. Wang, S.H. Huang, C.H. Lai, W.C. Chen, S.Y. Yang, K. H. Shen, and H.Y. Bor, J. Phys. D: Appl. Phys. 42 , 115006(2009).

[14]G. Csaba, P. Lugli, M. Becherer, D. S. Landsiedel, and W. Porod, J. Comput. Electron 7, 454 (2008).

[15]S. Mangin, D. Ravelosona, J. A. Katine, M. J. Carey, B. D. Terris, and E. E. Fullerton, Nature Mat. 5, 210 (2006).

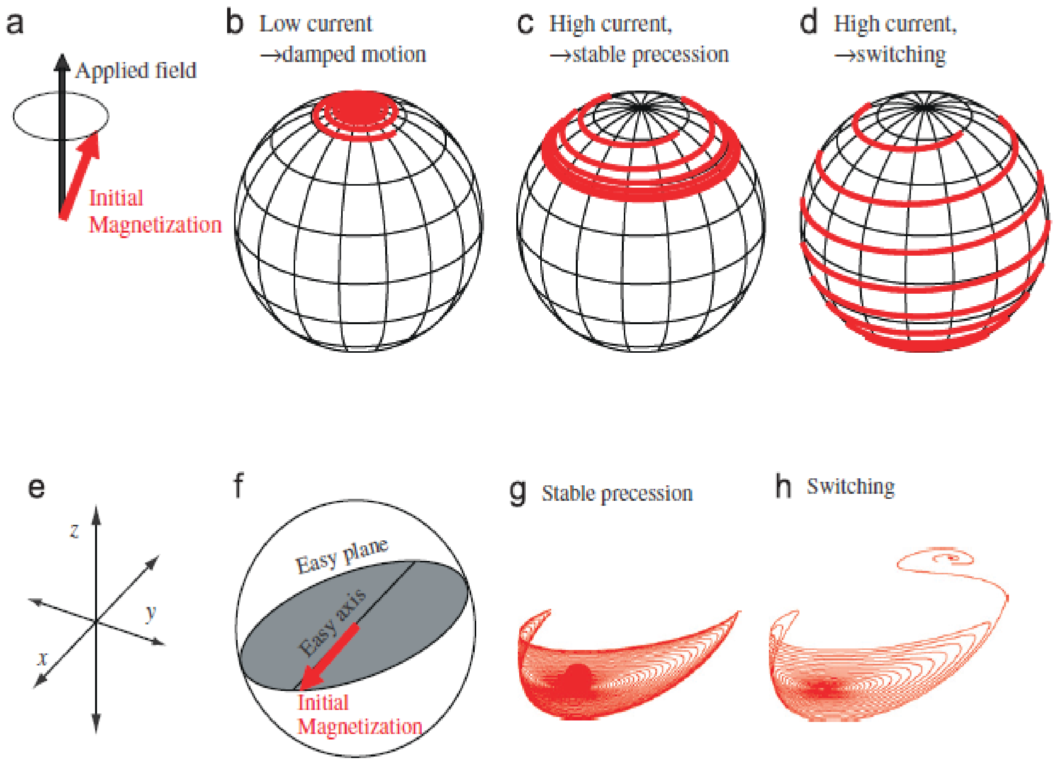

Figure 3.1: STT effect on an FM layer.[3] At a certain effective field, the magnetization of an FM layer is oriented in a certain direction (a).When a small spin torque acts on the FM layer; the magnetization can exhibit a damped motion about the initial direction (b). When the torque is high, the FM layer magnetization can either precess at a certain angle continuously (c) or switch to the opposite orientation (d). If an FM layer has easy axis in the xy plane as shown in (e) and (f), then (g) shows a possible stable precession condition and (h) shows a switching condition.[1]

---

[3] Reprinted from Journal of Magnetism and Magnetic Materials, Vol 32, D.C. Ralph, M.D. Stiles, Spin transfer torques, Pages No. 1190-1216, Copyright (2008), with permission from Elsevier.

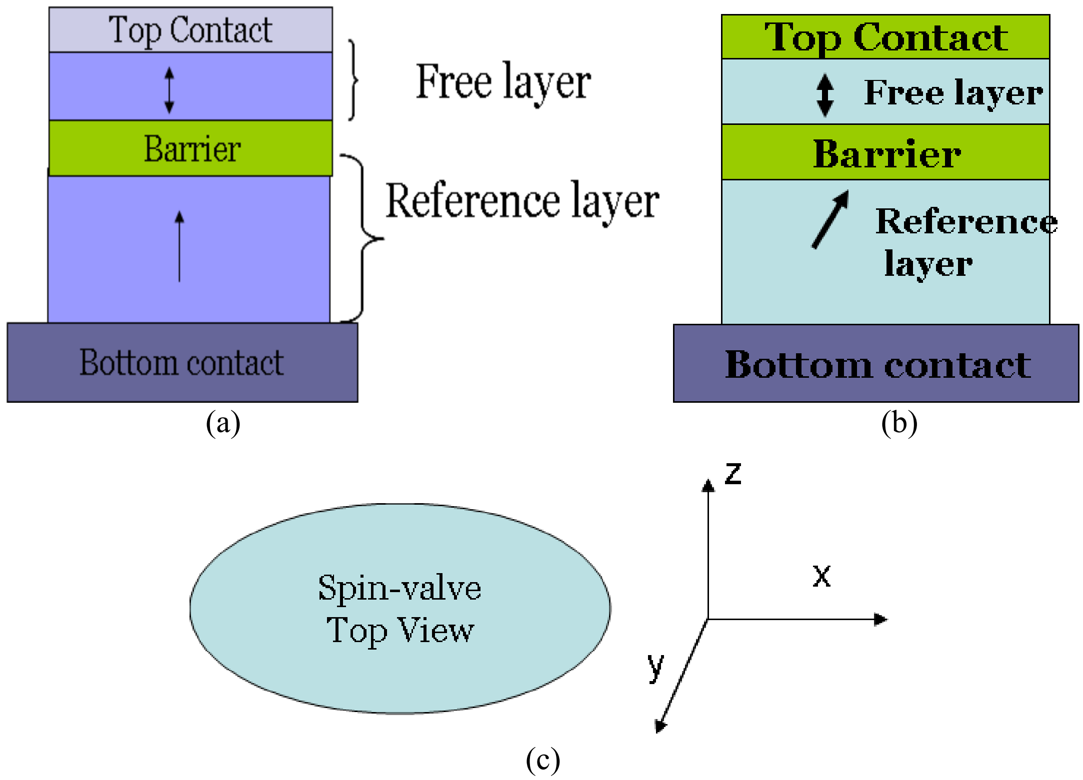

Figure 3.2: Schematics of the simulated spin-valve structure; (a) conventional collinear spin-valve, (b) proposed tilted spin-valve, (c) top view of the device.

Table 3.1: Switching time and current for different tilting of the reference layer

Tilt angle of Reference Layer (degree)	Critical Switching Current, A/m^2, for a 2 ns pulse	Switching time, ns, for $Ic=5x10^{11}$ A/m^2	
		P→AP	AP→P
0	$3.70x10^{11}$	0.89	0.3
6	$3.00x10^{11}$	0.72	0.3
15	$2.80x10^{11}$	0.62	0.2
25	$2.60x10^{11}$	0.5	0.2
35	$2.50x10^{11}$	0.478	0.2
45	$2.30x10^{11}$	0.449	0.2

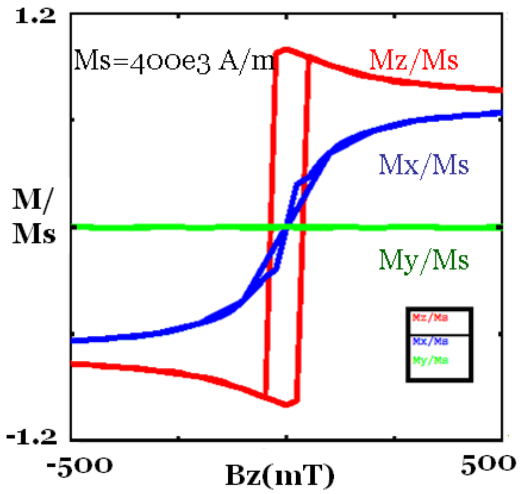

(a)

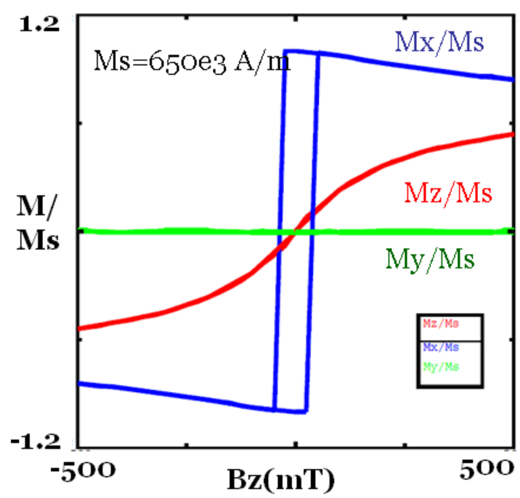

(b)

Figure 3.3: 2D M-H loop simulation of PMA FM material. The y-axis shows normalized Mz/Ms, Mx/Ms, and My/Ms with varying perpendicular applied field in x-axis. As Ms reduces, PMA increases.

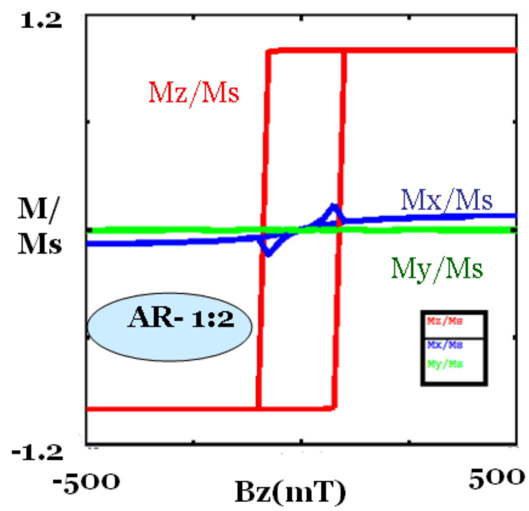

(a)

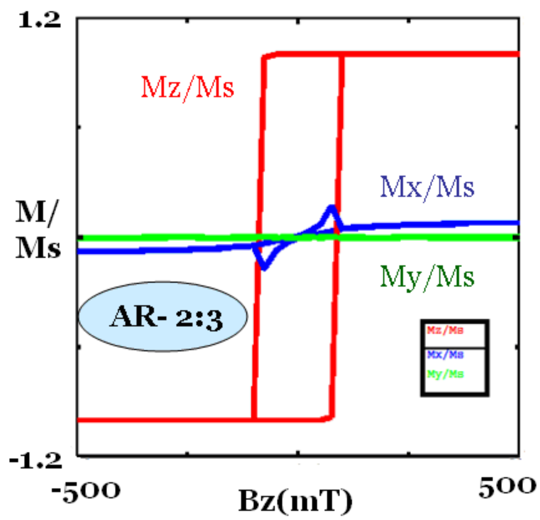

(b)

Figure 3.4: 2D simulation of PMA FM material with an elliptical shape and different aspect ratio (AR) of the ellipse in xy plane. The graphs show normalized M-H loop. The aspect ratio (AR) does not have any significant effect on materials with Ms=4x10^5 A/m.

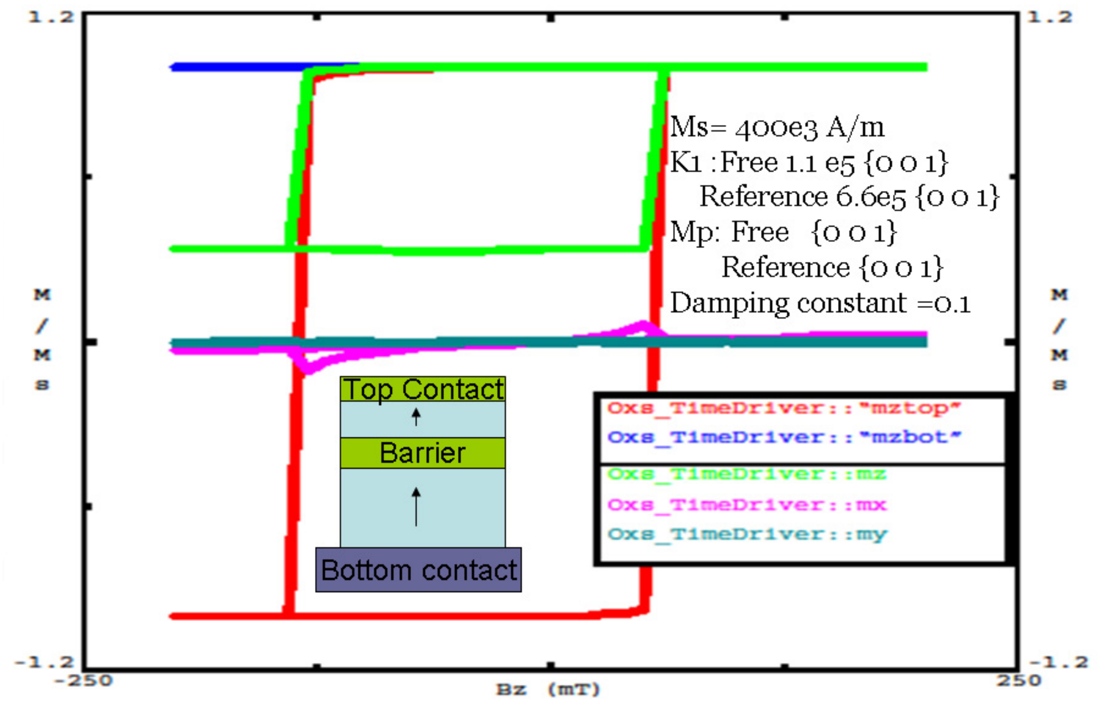

Figure 3.5: 3D M-H loop simulation of a conventional spin-valve. The red "mztop" curve shows Mz/Ms of the free layer and blue "mzbot" curve shows Mz/Ms for the reference layer which remains fixed during simulation. The green "mz" curve shows total Mz/Ms of the spin-valve, "mx" show the same for Mx/Ms and "my" shows the same for My/Ms. The loop shows asymmetric switching field since the reference layer is not switched.

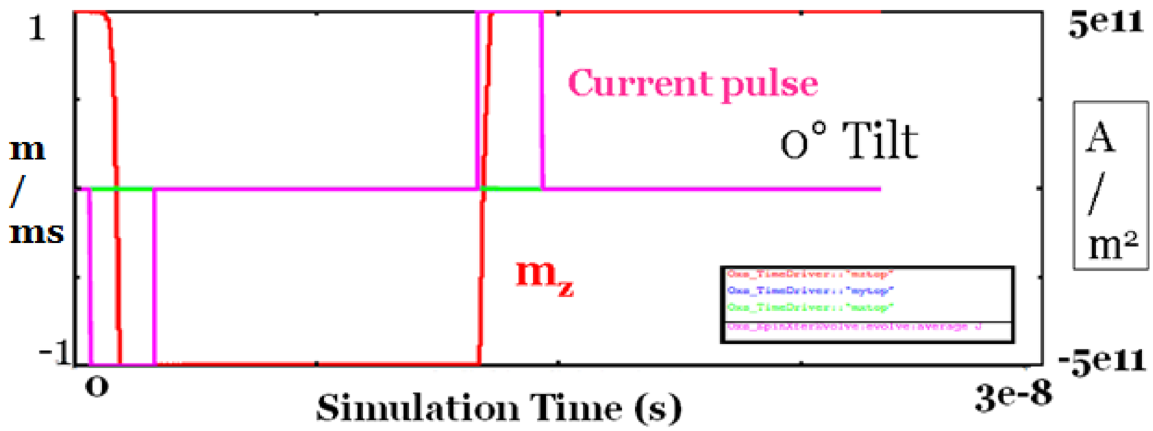

Figure 3.6: 3D time dependent simulation of equation (3.1) for a PMA spin-valve with 0° tilting. The left y-axis shows normalized M/Ms and the right y-axis shows applied current pulse with x-axis showing simulation time. Initially, both the layers are oriented in the +z direction. When the current pulse (J) is applied, the free layer switches to –z direction (m_z) without precession and vice versa. The reference layer remains fixed in the +z direction during the simulation.

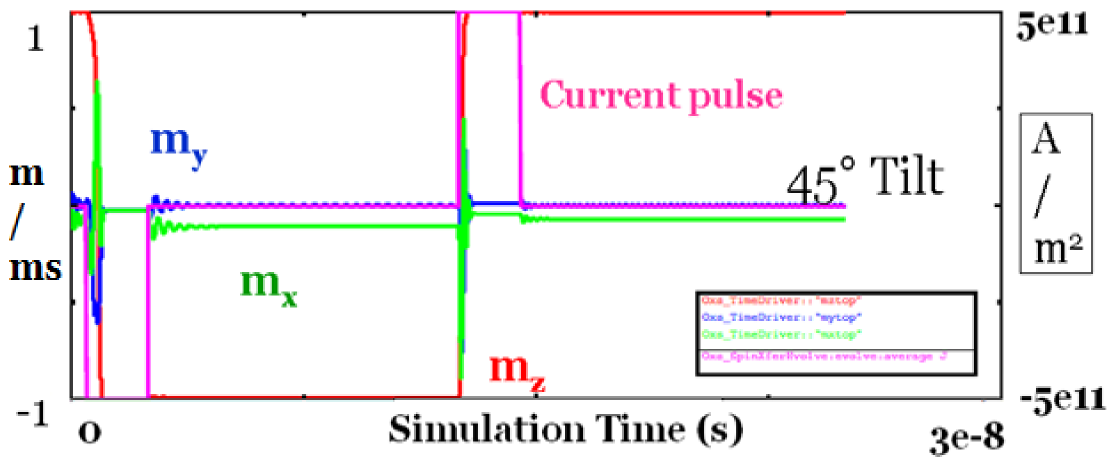

Figure 3.7: 3D time dependent simulation of equation (3.1) for a PMA spin-valve with 45° tilting. The left y-axis shows normalized M/Ms and the right y-axis shows applied current pulse with x-axis showing simulation time. Initially, both the layers are oriented in the +z direction. When the current pulse (J) is applied, the free layer starts to precess and finally switches to –z direction (m_z) and vice versa. The reference layer remains fixed in the +z direction during the simulation. The x and y oscillations of free layer are denoted as m_x and m_y, respectively.

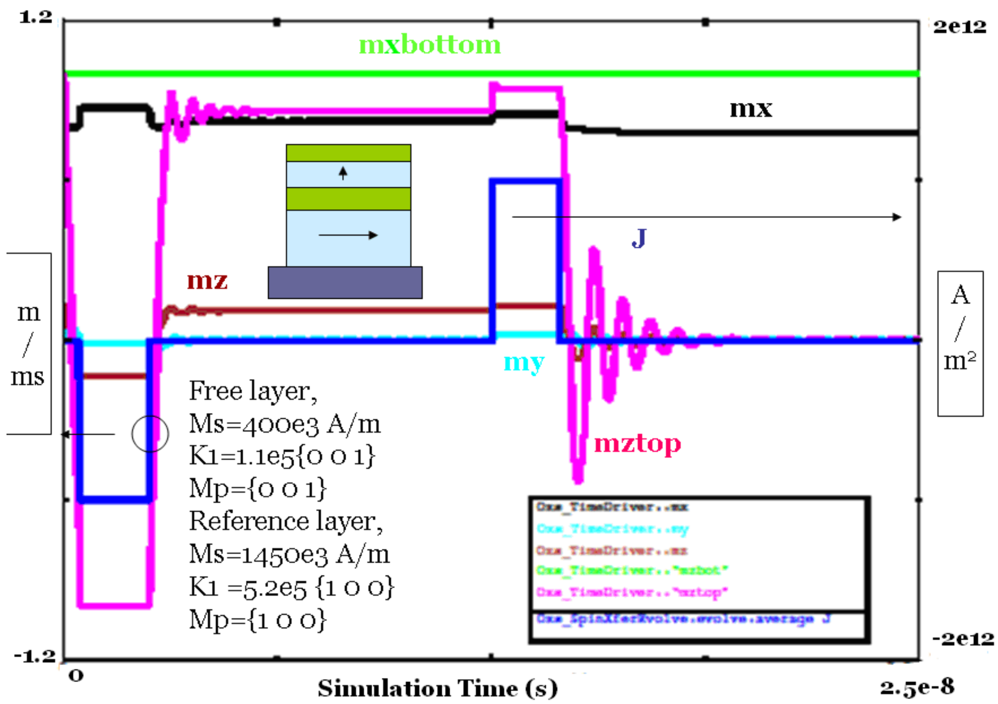

Figure 3.8: 3D simulation of equation (3.1) for a PMA spin-valve with 90° tilt. The left y-axis shows normalized M/Ms and the right y-axis shows applied current pulse with x-axis showing time. Initially, both the layers are oriented in the +z direction. When the current pulse (J) is applied, the free layer switches to –z direction (mztop), and then switches back to +z when the current pulse is stopped. The layer then loses energy in z when a positive current pulse is applied and stopped. The reference layer remains fixed in the +x direction (mxbottom) during the simulation. The "mz" curve shows total Mz/Ms of the spin-valve, "mx" show the same for Mx/Ms and "my" shows the same for My/Ms.

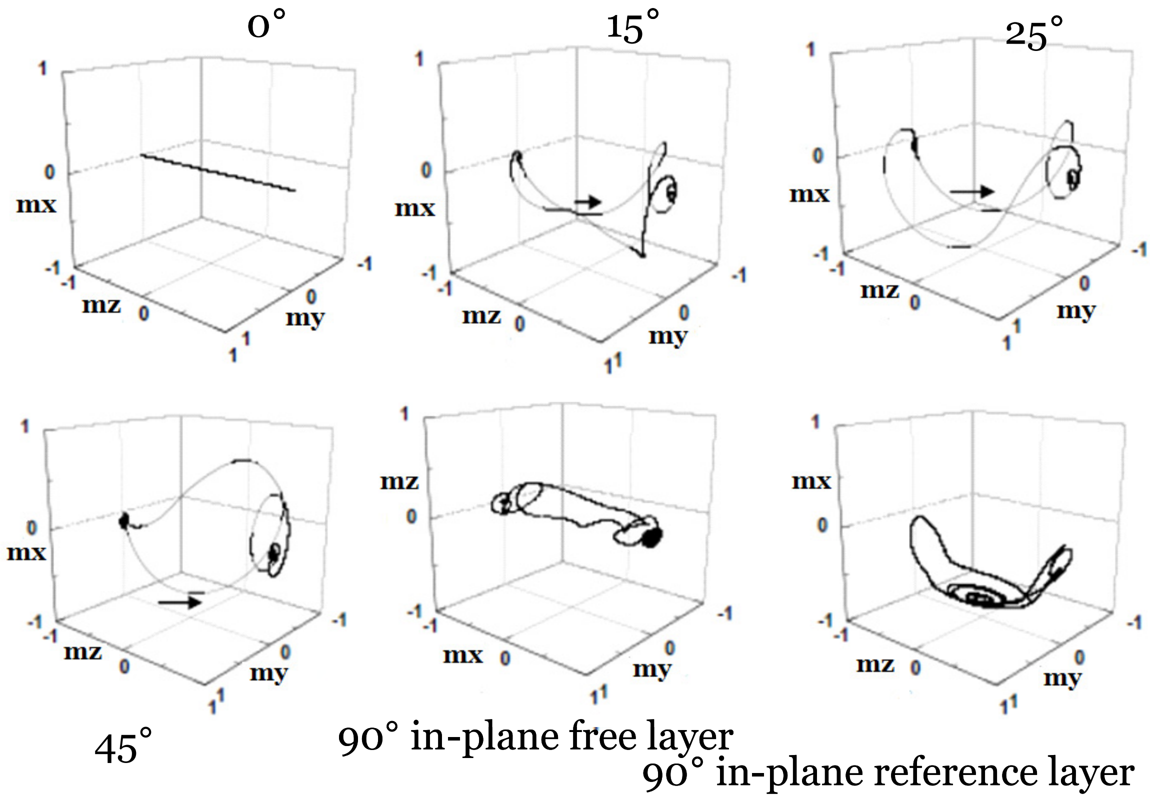

Figure 3.9: Magnetization dynamics of a PMA spin-valve with reference layer tilting of (a)0°, (b)15°, (c) 25°, (d) 45°, (e) 90° with in-plane free layer, and (f) 90° with in-plane reference layer for a 2 ns current pulse of $5x10^{11}$ A/m^2 . The switching becomes faster as the tilting increases to 45°. In (e), a number of precessions occur before the free layer is switched. In (f), the free layer stabilizes at a different orientation than easy axis, so switching is not accomplished.

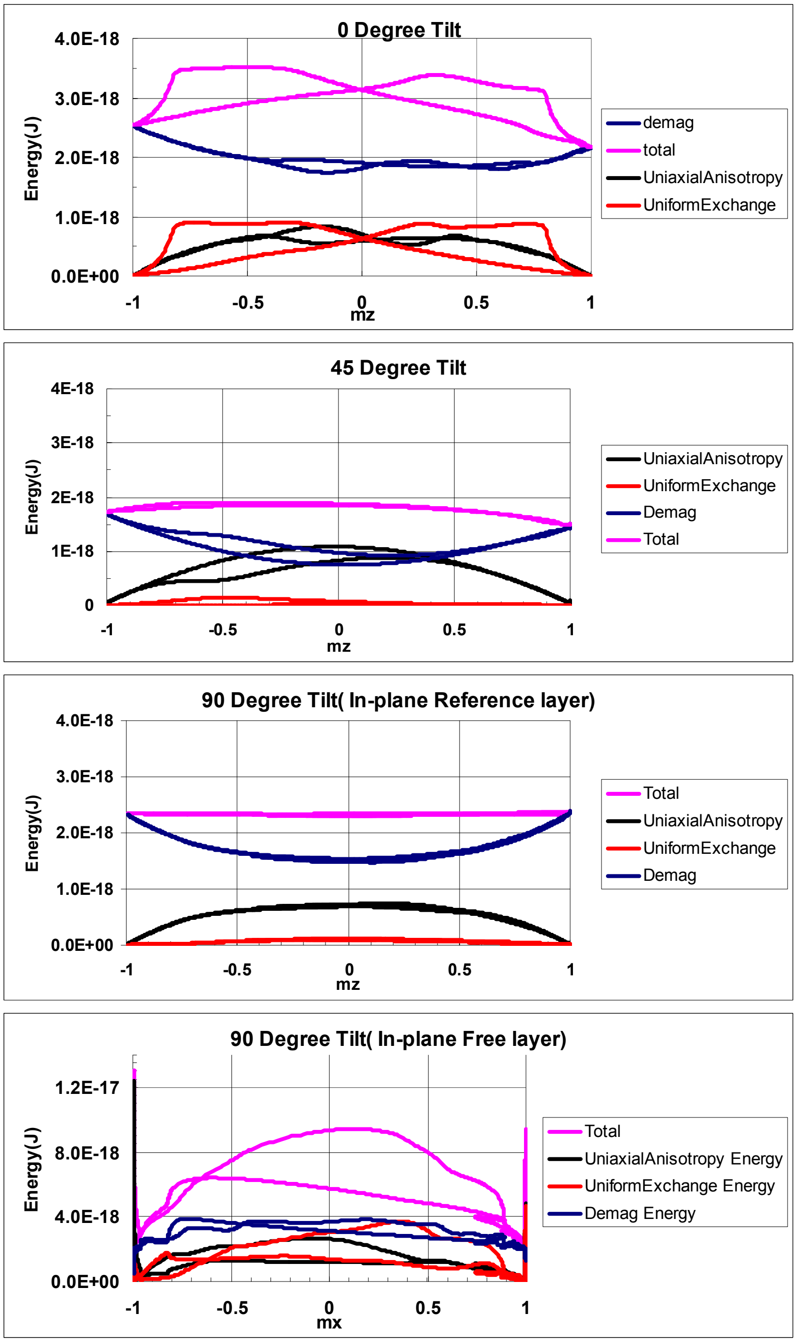

Figure 3.10: Energy plot vs free layer magnetization at different tilting. Demagnetization energy is different for out-of-plane and in-plane free layer and is important to lower switching energy.

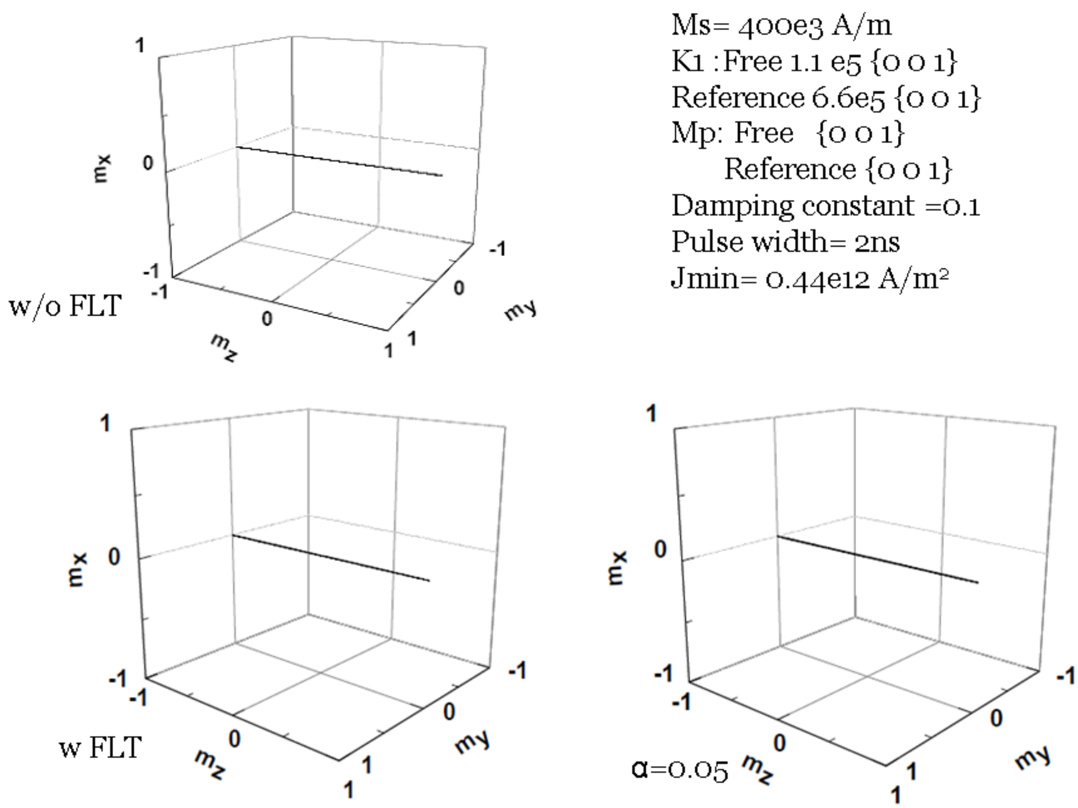

Figure 3.11: Magnetization dynamics of a PMA spin-valve with 0° tilting. The switching does not have any observable precession. The top figure shows trajectory without FLT in equation (3.1), the bottom left figure shows the same with FLT and a damping constant of 0.1. The bottom right figure shows the same with damping constant of 0.05.

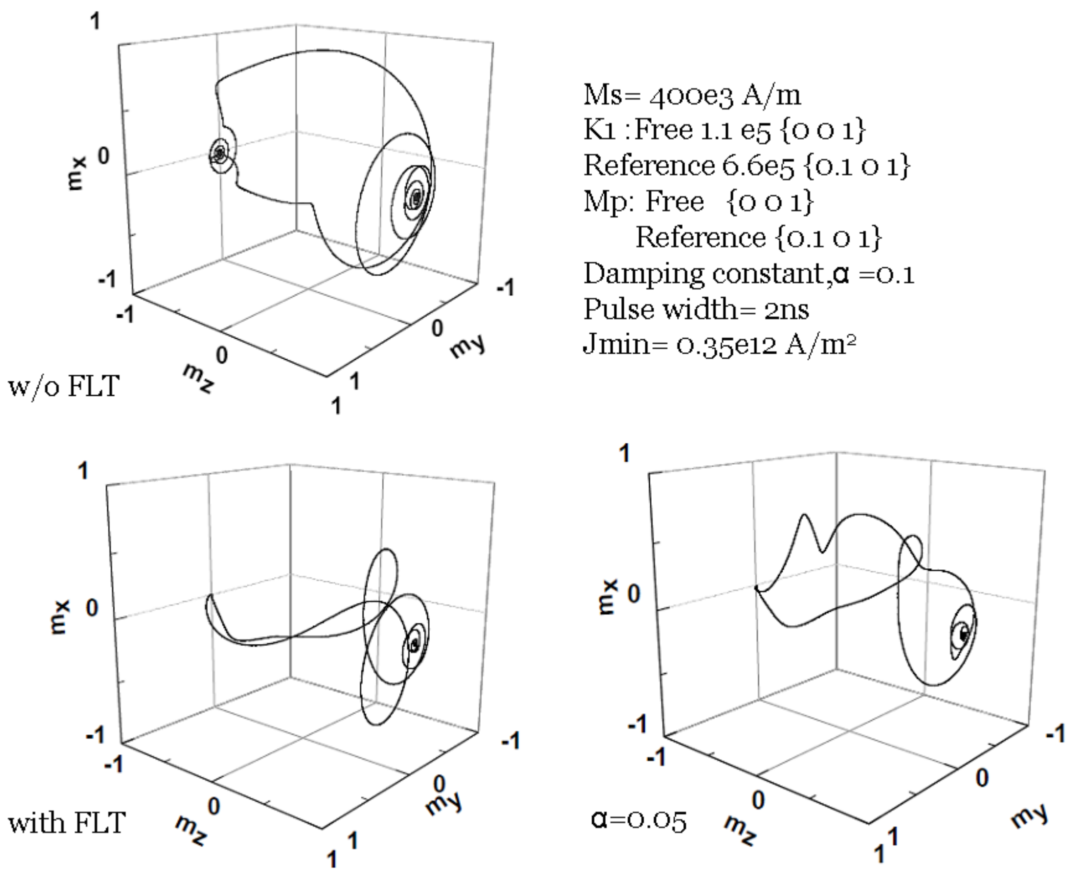

Figure 3.12: Magnetization dynamics of a PMA spin-valve with 6° tilting showing precessional switching. The top figure shows trajectory without FLT in equation (3.1), the bottom left figure shows the same with FLT and a damping constant of 0.1. The bottom right figure shows the same with damping constant of 0.05.

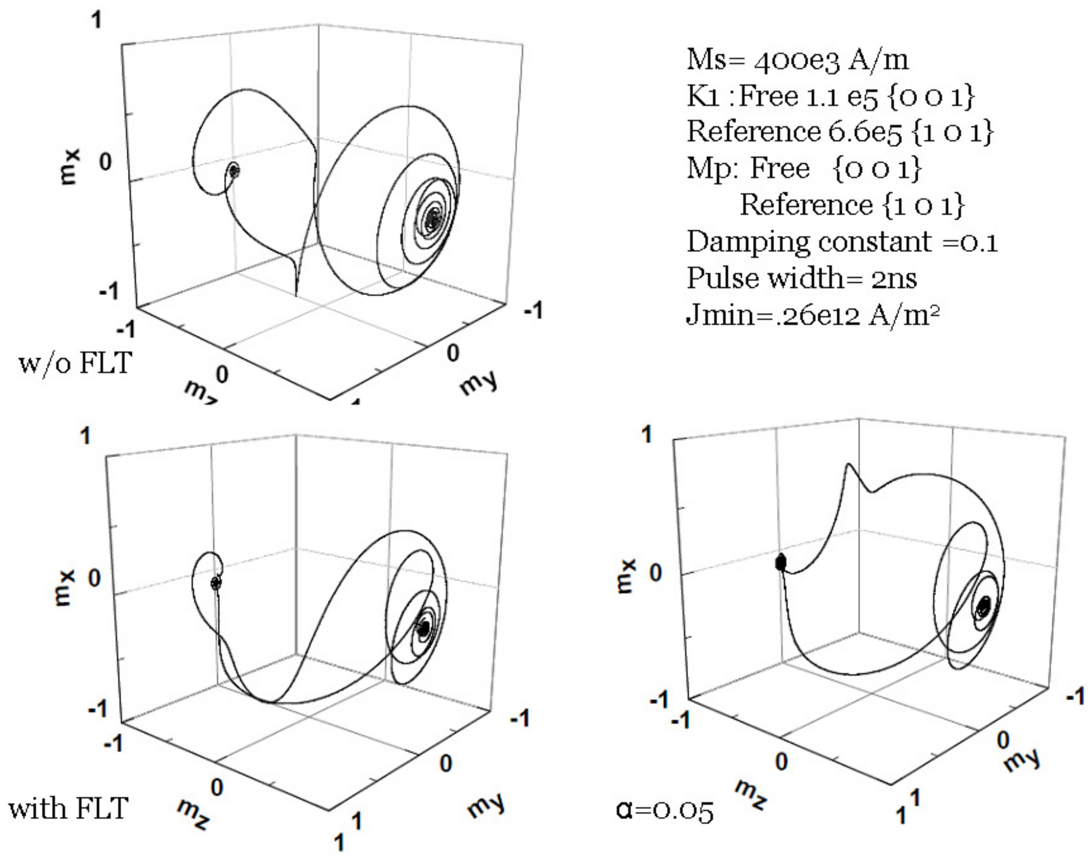

Figure 3.13: Magnetization dynamics of a PMA spin-valve with 45° tilting showing precessional switching. The top figure shows trajectory without FLT in equation (3.1), the bottom left figure shows the same with FLT and a damping constant of 0.1. The bottom right figure shows the same with damping constant of 0.05.

Chapter 4: Spin-transfer-torque switching of tilted PMA spin-valves with Co/Pt and Co/Ni multilayer

This chapter discusses fabrication, material characterization, and point contact measurement of PMA spin-valves. A seed layer was introduced to attain smooth films and (111) crystal orientation of the multilayer. The deposited layers were characterized by AFM, XRD, XPS, VSM, and MR measurements. Point contact measurements were done on the samples with good MR to study spin torque effect.

4.1 Fabrication of multilayer PMA spin-valve

In this work, Co/Pt and Co/Ni multilayer were chosen to constitute reference and free layers of the spin-valve. The advantage of these multilayers is that the magnetization direction, amount of tilt from a reference axis, quality of PMA and hysteresis can be varied by varying the thickness and number of layers in the stack. Again, these materials are well studied experimentally so literature was available to guide the process flow. The Co/Pt is known to show good PMA for a wide range of deposition condition and thickness. However, it is important to have a seed layer to allow the (111) growth of Co/Pt. Here, a seed layer of TaN/Ta/Pd was used on SiO_2-grown Si substrate for stack deposition. It is difficult to achieve crystalline Pd without a thin (5-10 nm) Ta seed layer. [1] It is believed that atoms deposited on a thin Ta layer enjoy greater mobility to form their energetically favored texture.[2]The thicknesses of TaN (40-50 nm) and Pd (15-25nm) were optimized to achieve a low RMS roughness of ~1 nm while the thickness of Ta was ~ 6nm. The TaN and Ta were sputter deposited at 1.1 KW and 10 mTorr while Pd was e-beam evaporated at ~0.2 Angstrom/s deposition rate. The TaN as well as the combined seed layer shows mainly (111) crystal orientation with and without any post deposition annealing in X-ray diffraction (XRD) measurements. If TaN is made thicker, then other crystal peaks, namely (200) start to come up. On the other hand, if TaN is made thinner or omitted, then heat conduction during Co/Pt evaporation process or annealing becomes poor and surface becomes rough resulting in a low quality film. Having a Pd (15-25nm) seed layer has also shown to improve PMA mainly due to the improved crystalline orientation and quality.[1, 2]

The fabrication process is, in general, as follows- Si (100) wafers were piranha cleaned, then loaded in an oxide furnace to grow ~400 nm SiO_2 through wet oxidation. Then wafers were loaded to a DC magnetron sputtering chamber to sputter TaN and Ta without breaking vacuum. After this, Pd was deposited by e-beam evaporation. The final stack of Co/Pt, Co/Ni and Cu layers were also deposited in an e-beam evaporation chamber with base pressure less than 5e-6 Torr. The deposition rate of Co, Pt, and Ni was less than 0.1 Angstrom/s. A number of calibration samples were prepared to optimize the spin-valves. Table 4.1 shows a PMA spin-valve without any tilt (sample I) and a spin-valve with ~45° tilt (sample II); Table 4.2 shows a PMA spin-valve with 12° tilt (sample III) and a spin-valve with ~90° tilt where the free layer is in-plane and reference layer is out-of-plane (sample IV). Sample II had 15 nm Pd and was annealed at 400°C for 10 s in N_2 ambient to improve the (111) crystal growth after the seed layer deposition. The other samples had 25 nm Pd and (111) crystal structure was obtained without annealing. In sample I, Co and Pt had thicknesses of ~0.4 nm and 1.2 nm respectively showing a strong PMA. Similar Co thickness also showed strong PMA with 1.7nm Pt. In sample II, Co had a thickness of 0.7 nm, which allowed the magnetization to be tilted as will be verified later by the VSM measurements, and Pt had a thickness of 1.7 nm.[3] Sample II also had a Co (0.7nm)/Ni (0.7nm) in-plane multilayer which increase the in-plane magnetization component. Sample III had Co (0.4 nm)/Pt(1.2)nm and Co(0.2nm)/Ni(0.4nm) multilayer where Co and Ni thicknesses presumably originate PMA with small tilting in magnetization. In sample IV, a thick Co (1.5nm) layer was deposited as free layer which prefers bulk anisotropy and the magnetization easy axis is along the in-plane direction. In all the samples, number of Co/Pt repeat in reference layer was fixed at four since four to eight repeats of multilayer usually provide good PMA and squareness in M-H hysteresis loop.[1,3]

4.2 Material characterization of spin-valves

The surface morphology of the layers was examined by atomic force microscopy (AFM), the crystalline quality was investigated by X-ray diffraction (XRD), the elemental quality was studied by X-ray photoelectron spectroscopy (XPS), and the domain structure was observed by magnetic force microscopy (MFM). Table 4.3 presents the RMS roughness measured by tapping mode AFM and four point resistance of the samples. The RMS roughness improved by a thicker Pd layer and no annealing. The XPS was performed on sample II and the summary of the peak positions for different elements are shown in Table 4.4. During XPS, materials were subsequently etched and scanned to perform a depth profile. Platinum and Pd show only metallic peaks, Cu barrier shows metallic peaks although the top Cu is oxidized. The Co and Ni layers show an oxidation peak although it is not possible to clearly identify whether these are mono-oxide or di-oxide. The presence of the oxides does not seem to deteriorate the magnetic performance of the stack as will be shown later. The XRD data for samples I and II are shown in Figure 4.1 and Figure 4.2 shows the same for sample III and IV. The peak at 35.6° is TaN (111) peak, [4] the peak at 69° is Si(100) peak, and the (111) peak at 40° is from mainly Pd and Pt. [5, 6] From literature, the face centered cubic (fcc) Pt (111) peak is at 39.76° ,fcc Co (111) peak is at 44.2°,[3] Cu(111) peak is around 43°, [7] and Ni (111) peak is around 44.5° [8]. However, in Figures 4.1 and 4.2, only one mean peak is observed around 40°. The thickness of Co, Cu and Ni is probably not large enough to show individual peaks.

Magnetic force microscopy (MFM) is a technique where the domain structure of a magnetized film is observed using tapping mode scanning in lift mode in a Dimension V microscope as shown in Figure 4.3.[9] In this technique, first a tapping cantilever with a special magnetic tip is scanned over the surface to obtain surface topography. Then, the tip is raised a certain height above the sample to maintain a constant separation between the tip and surface. In absence of a magnetic field, the cantilever oscillates at a certain frequency f_0. The frequency shifts by a small amount Δf proportional to vertical gradients of the magnetic force on the tip. This change in frequency is detected by three ways: amplitude detection by change in oscillation amplitude, phase detection by measuring the cantilever's phase of oscillation with respect to the piezo drive, and frequency detection by tracking the change in oscillating frequency.[9] Figure 4.4 is a frequency detected MFM image of demagnetized sample II which shows up and down stripe-like magnetic domains. [10]

4.3 Magnetic characterization of spin-valves

The magnetic properties of the spin-valves were characterized by extra-ordinary Hall Effect (EHE) measurement, MR measurement, and vibrating sample magnetometer (VSM) measurement. The EHE is observed mainly in ferromagnets, and also in strong paramagnets and antiferromagnets. The Hall resistivity in these samples are given as

$$\rho_H = R_0 H + 4\pi R_S M \tag{4.1}$$

where the first term is the ordinary Hall effect and the second term is the EHE. Here R_0 is the ordinary Hall coefficient, H is the applied magnetic field, R_S is the extra-ordinary Hall coefficient, M is the spontaneous magnetization. The applied magnetic field makes the extra-ordinary effect evident in a macroscopic scale but is not the primary cause. It is generally believed that EHE is caused by an asymmetric scattering of the conduction electrons by various irregularities in the regular arrangement of the localized moments on the magnetic ions.[11]The two main mechanisms for this effect are known as skew scattering and quantum side-jump which are shown in Figure 4.5. Theories based on these mechanisms relate R_S on the longitudinal resistivity in the following way

$$R_S = a\rho + b\rho^2 \tag{4.2}$$

where ρ is the longitudinal resistivity, a, b are constants of skew-scattering and side-jump components respectively.[12] The scattering may be caused by impurities, phonons and thermal spin disorder. Although this formalism was proposed for bulk ferromagnets, this is applicable to FM/Non-FM multilayer structures also.[12] Figures 4.6 through 4.9 show EHE and MR data for the four samples respectively. The measurements were done by H. Seinige and supervised by Dr. M. Tsoi.[13] Sample I shows a square hysteresis loop with distinct switching of the free layer during EHE measurement in Figure 4.6 due to the strong PMA of Co(0.4nm)/Pt(1.2nm) multilayer. However, for the 45° tilted layers in sample II, the hysteresis loop is slanted and free layer switching is not evident in the EHE of Figure 4.7. Sample III shows mostly square loop but again free layer switching is not evident in the EHE of Figure 4.8. The free layer magnetization in these two samples is probably not comparable to the reference layer and does not come up in EHE measurement. Sample IV shows a nice square loop originating from the PMA reference layer in the EHE of Figure 4.9. This sample also does not show any free layer switching effect. The MR curves, on the other hand, show separate free layer and reference layer switching for all four samples. The MR values of all samples are summarized in Table 4.3. Sample II has the highest MR of 0.34% followed by sample III with 0.19%. The MR curve of sample II in Figure 4.7 has a broader distribution with out-of-plane (perpendicular) field possibly since this is not the easy axis of magnetization and also due to the grains in evaporated metal layers. Samples II and III have Co/Ni layers around the non-FM barrier which improves the MR with respect to sample I. Sample IV has a small MR of 0.07% probably because the in-plane layer is not magnetized in the out-of-plane direction and also due to the spin-scattering of Pt in reference layer.

Vibrating sample magnetometer (VSM) measurements of the samples were carried out at University of Minnesota and the data are shown in Figure 4.10 through 4.13 for samples II, III, and IV and the data are summarized in Table 4.4. The figures show M-H hysteresis loops for both in-plane and out-of-plane applied fields and the free layer switching is evident for samples II and III in Figure 4.10, 4.11 and 4.12. The amount of tilting for sample II is ~45° and ~12° for sample III as calculated from Mr/Ms values in Table 4.4.[14] The saturation magnetization (Ms) values of in-plane and out-of-plane fields are similar to each other in samples II, III, and IV. The out-of-plane and in-plane coercivity values of sample II are close to each other but out-of-plane coercivity is about 4x times of in-plane coercivity for sample III and IV. Figure 4.11, 4.12 and 4.13 show the derivative of M-H loops for sample II, III, and IV respectively. The derivative curves show the switching of free layer and reference layers. A change in slope is observed for switching of each individual layer. In Figure 4.11, sample II clearly shows two different slopes during both in-plane and out-of-plane measurements associated with the switching of free and reference layers. The slopes also change slowly similar to the MR curves in Figure 4.7 indicating that the broadening in MR is due to the hard axis magnetization. A small but distinct slope related to free layer switching is also observed in out-of-plane derivative for sample III in Figure 4.12. The onsets of free layer switching from Figures 4.8 and 4.12 are at similar fields indicating that the MR is indeed from the antiparallel orientation of the free layer. However, Figure 4.13 mainly shows one layer switching with both field directions which may explain the broad distribution of MR in Figure 4.9. With perpendicular applied field, the reference layer switching is evident. The in-plane free layer is parallel to the PMA reference layer at very high perpendicular fields but probably has an angular orientation with respect to the reference layer at other fields, resulting in a broad MR distribution. Figure 4.14 shows angular VSM measurements of sample IV at 30° and 60° angles with respect to the plane of the sample and their respective 1st order derivatives. There are two distinct switching events from two different layers. Comparing the data with Figure 4.13, the lower field switching is presumably from the free layer and the higher field switching is from the reference layer. At these angular positions, both the FM layers are canted and switch magnetization with applied fields.

4.4 Point contact measurement of spin-valves

Point contact measurements were carried out to study spin-transfer-torque (STT) effect of the spin-valve samples. The measurements were done by H. Seinige and supervised by Dr. M. Tsoi. Two different types of measurements were done where in one case, a dc bias current was applied to the contact and magnetic field was varied from negative to positive and vice versa. In the second set of measurement, known as current-voltage (I-V) measurement, a fixed magnetic field was applied perpendicular to the sample and dc current was varied.[15]The first measurement is known as MR measurement and STT effect is observed in the slope of applied current vs magnetic switching field curves. The MR measurements were done on all four samples. Sample I did not show any STT effect, the switching field did not change with varying dc current probably due to the spin-scattering effect of Pt layers near Cu spacer.[16]Sample II with 45° tilt showed distinct STT effect in both MR and I-V measurements. Figure 4.15 shows change in resistance at a fixed dc current while the magnetic field is swept. At high negative fields, both layers are parallel and resistance is almost constant, then the free layer switches at a small positive field and resistance reaches a higher value. At an even higher positive field, the reference layer also switches direction and the two layers become parallel again and reach the previous parallel resistance value. This is mentioned as upsweep from now on. The measurement starting with high positive field gave similar result and is mentioned as downsweep. The upsweep and downsweep measurements were carried out at different dc current levels and plotted against free layer switching field in Figure 4.16. The reference layer switching field show little dependence on current and is not shown in plot. The switching current density at zero field was calculated from the plot and compared in Table 4.6 with sample III. During upsweep, the switching field decreases as more electrons flow through the free layer or negative current increases. Here negative current aides the magnetic field to switch the free layer to antiparallel orientation as expected. On the other hand, as positive current increases, electrons are flowing through the reference layer and the resulting torque wants to keep the free layer parallel with the reference layer. This spin current effect makes free layer switching difficult and higher positive switching field is needed to switch the free layer against the spin current. During downsweep, however, the free layer switching becomes difficult with negative current and easier with positive current indicating some biasing effect. From the measurements, it seems that for negative current a field is present which aides the reference layer in downsweep. Similarly, for positive current, the field works against the reference layer in downsweep. This field or biasing effect results in the positive slope during downsweep measurements instead of a negative slope. This effect might result due to charge current, field-like-torque or in-plane magnetic component, which is not clearly understood at this moment. Figure 4.17 shows both MR and I-V data of sample II where only the free layer is switched by varying magnetic field or current. As dc current is swept from negative to positive values, and vice versa, free layer switching is observed and the hysteresis loop can be exchange biased by applying a magnetic field perpendicular to the sample. Similar phenomena are observed with sweeping the magnetic field at different fixed dc current levels. The slopes of the current vs switching field curves are linear, as expected.

Figure 4.18 shows the applied current vs switching field plot for sample III with 12° tilt. During upsweep, the switching field moves towards more negative values as negative current increases but for positive current, the magnitude of slope is changed. Again, during downsweep, the switching field moves towards positive values as negative current increases, as expected, with a change in the magnitude of slope when current direction is reversed. Reference 16 also reports similar change in slope for P→AP transition of the free layer when the sign of current is reversed. When electrons are flowing through the reference layer, the STT works to keep the free layer parallel; but if the applied field is in such a direction that it works to switch the free layer antiparallel then the domains around the edge of the free layer get canted away from the perpendicular direction and results in a slope change of I-B curve.[16] Reference 16 also reports change in the sign of slope at certain canted conditions which might explain the positive slope obtained in sample II during downsweep measurements. The free layer is probably canted to some degree from the perpendicular direction due to the deposition conditions. Moreover, the tilted reference layer introduces nonuniform effective field on the free layer.[17]Both these effects including other effects not clearly understood at this point, might result in a positive slope during downsweep measurements instead of a negative slope in sample II.

The switching current density, point contact radius, and slope of I vs B plots are summarized in Table 4.6 for samples II and III. The current density of sample III is smaller than sample II since Ms of sample III is about 0.5x times of sample II as shown in Table 4.5. The damping constant of the samples may be assumed similar since free layer and top contact of both samples are very similar as shown in Table 4.1 and 4.2. The point contact radii for samples II and III are 3.41 nm and 5.33 nm respectively. The slopes of upsweep and downsweep switching of sample II calculated from Figure 4.16 are higher than those of sample III calculated from Figure 4.18. A higher slope means that less spin current is needed in sample II to obtain the same change in switching field indicating a possibly stronger STT effect. Moreover, STT effect is observed for both positive and negative currents during up and down sweeps in sample II whereas in sample III, the STT effect is significant only for negative current. The improvement in STT effect in sample II might be due to the tilted polarization of the spin-valve which introduces precessional switching.

3-dimensional plots of downsweep and upsweep MR measurements of sample IV are shown in Figure 4.19 and 4.20 respectively. Magnetic field is shown in x-axis, dc current in y-axis, and resistance value in color contrast. Different colors indicate different resistance values (dark-low, light-high). The field was applied at different angular orientations with respect to the plane of the sample. Spin-torque-effect is observed as the resistance change varies with applied field, especially at 30° and 60°. At 90° the free layer switching is very slow and resistance change is not distinct, which is similar to MR results with applied field in Figure 4.9. At 0°, there is an observable change in resistance at about ±20mT and ±45mT with a distribution in the switching fields. At this angular orientation, the in-plane free layer is oriented mostly at 0° but the PMA reference layer probably has a tilted orientation with respect to the plane of the sample. It is possible that the final magnetization of the reference layer has variation among measurements and thus causes the distribution in switching fields. At 30° and 60° applied fields, the light colored high resistance region broadens with positive current in downsweep and with negative current in upsweep. There are three different regions in Figure 4.19 and 4.20 at 0°, 30° and 60° angular orientations. Two different slopes are obtained at the intersections of the regions with high and low resistances. The intersections, at about ±15mT, do not show strong STT effect. The intersections, at about ±50mT, show negative slope during both downsweep and upsweep measurements. During upsweep measurement, the region of antiparallel orientation or high resistance increases as negative current increases since negative current tends to maintain the free layer in antiparallel orientation, as shown in Figure 4.20. The high resistance region gets smaller with positive current as positive current tends to help parallel orientation. On the other hand, during downsweep measurement high resistance region gets smaller with increasing negative current, as shown in Figure 4.19. This phenomenon might be due to the similar canting and biasing effects observed in sample II which are not clearly understood at this moment.

4.5 Summary

This chapter discussed fabrication and characterization of spin-valves with different amount of tilted magnetization. The difference of tilt was obtained by varying mainly the thickness of Co and Ni layers. The tilting is quantified through VSM measurement. Material characterization was done to confirm a uniform, smooth film deposition. The STT effect of different samples was studied through point contact measurements and compared. The STT effect is not observed in the PMA sample with 0° tilting probably due to the presence of Pt near the Cu barrier. The sample with 45° tilting shows STT effect over a wide range of dc current compared to the sample with 12° tilting. The sample with 90° tilting shows STT effect mainly at angular applied fields. Tilting introduces new effects which needs further investigation.

4.6 References

[1]J. H. Jung, B. Jeong, S. H. Lim, and S.R. Lee, App. Phys. Exp. 3, 023001(2010).

[2]R. Law, R. Sbiaa, T. Liew, and T. C. Chong, Appl. Phys. Lett. 91, 242504 (2007).

[3]J.H. Park, C. Park, T. Jeong, M. T. Moneck, N. T. Nufer, and J.G. Zhu, J. App. Phys. 103, 07A917(2008).

[4]A. E. Kaloyeros, X. Chen, T. Stark, K. Kumar, S. C. Seo, G. G. Peterson, H. L. Frisch, B. Arkles, and J. Sullivan, J. Electrochem. Soc. 146, 170 (1999).

[5]J. P. Kurpiewsky, MSME Thesis, Massachusetts Institute of Technology (2005).

[6]G. A. Bertero, PhD Dissertation, Stanford University (1995).

[7]X.P. Qu, J. J. Tan, M. Zhou, T. Chen, Q. Xie, G. P. Ru, and B. Z. Li, Appl. Phys. Lett. 88, 151912 (2006).

[8]S. W. Jung, W. I. Park, G. C. Yi, and M. Kim, Adv. Mater. 15, 1358 (2003).

[9]Dimension 3100 manual, Veeco Instruments Inc.

[10]L. Belliard, J. Miltat, V. Kottler, V. Mathet, C. Chappert, and T. Valet, J. Appl. Phys. 81, 5315 (1997).

[11]C. M. Hurd, The Hall effect in metals and alloys, Plenum press, NY-London, 1972.

[12]C. L. Canedy, X. W. Li, and G. Xiao, J. Appl. Phys. 81, 5367 (1997).

[13]F. Ferdousi, H. Seinige, U. Roy, J. Mantey, M. Tsoi, and S. K. Banerjee, SRC TECHCON 2011.

[14]C. L. Zha, J. Persson, S. Bonetti, Y. Y. Fang, and J. Åkerman, Appl. Phys. Lett. 94, 163108 (2009).

[15] Z. Wei, PhD dissertation,The University of Texas at Austin, 2008.

[16]S. Mangin, D. Ravelosona, J. A. Katine, M. J. Carey, B. D. Terris, and E. E. Fullerton, Nat. Mat. 5, 210 (2006).

[17]O. J. Lee, V. S. Pribiag, P. M. Braganca, P. G. Gowtham, D. C. Ralph, and R. A. Buhrman, Appl. Phys. Lett. 95, 012506 (2009).

[18]L. Berger, Phys. Rev. B 2, 4559 (1970).

Table 4.1 Metal composition and thickness of spin-valve samples I & II

	I (Angstrom)		II (Angstrom)
Cu	40	Cu	41
Pt	10	Pt	6
Co	3	Co	2
Pt	10	Ni	6
Co	3	Co	4
Cu	40	Cu	40
Co	4	Co	4
Pt	12	Ni	7
Co	4	Co	7
Pt	12	Pt	17
Co	4	Co	7
Pt	12	Pt	17
Co	4	Co	7
Pt	12	Pt	17
Co	4	Co	7
Pd	250	Pt	16
Ta	60	Co	7
TaN	500	Pd	150
SiO_2	4000	Ta	60
Si		TaN	500
		SiO_2	4000
		Si	

Table 4.2: Metal composition and thickness of spin-valve samples III & IV

	III (Angstrom)		IV (Angstrom)
Cu	40	Cu	40
Pt	6	Co	15
Co	2	Cu	40
Ni	4	Co	4
Co	2	Pt	12
Cu	40	Co	4
Co	2	Pt	12
Ni	4	Co	4
Co	2	Pt	12
Pt	12	Co	4
Co	4	Pt	12
Pt	12	Co	4
Co	4	Pd	250
Pt	12	Ta	60
Co	4	TaN	500
Pt	12	SiO_2	4000
Co	4	Si	
Pd	250		
Ta	60		
TaN	500		
SiO_2	4000		
Si			

Table 4.3: AFM RMS roughness and 4-point probe resistance of the samples

Sample	RMS roughness(nm)	4-pt resistance (ohm)	MR (%)
I 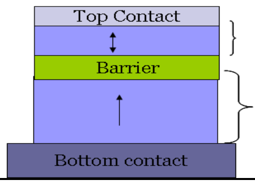	0.978	1.33	0.11
II 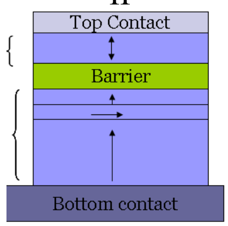	1.27	1.40	0.34
III 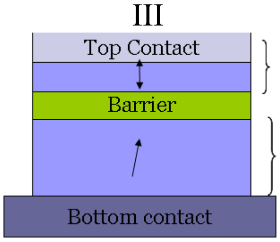	0.86	1.24	0.19
IV 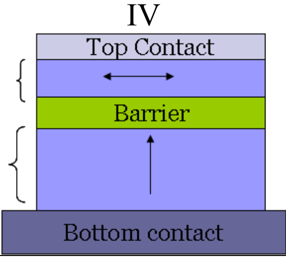	0.685	1.37	0.07

Table 4.4: XPS analysis of the peak positions of different metal elements in sample II

Element	Binding energy (eV)	Atomic percentage (%)	FWHM
	778.19	27.41	1.345
Co 2p	793.84	25.49	3.4506
	780.56	47.09	5.5173
	852.43	37.59	1.23
Ni 2p	869.85	24.92	2.6
	855.47	37.48	6.49
Cu 2p	932.51	69.28	1.18
	952.33	30.72	1.64
Pd 3d	335.18	47.06	1.21
	340.5	42.94	1.38
Pt 4f	71.3	51.78	1.23
	74.62	48.22	1.47

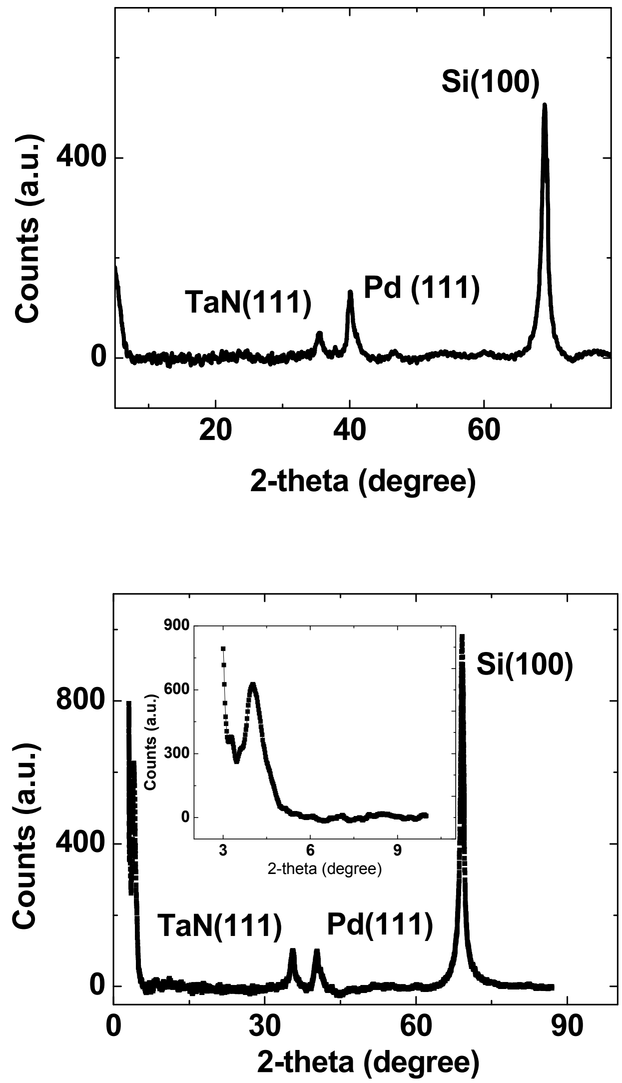

Figure 4.1: The XRD analyses of sample I (top) and sample II (bottom) which show (111) crystal growth of the spin-valve structure. The inset of bottom figure shows small angle peak corresponding to the thickness of one Co/Pt bilayer. The (111) peak at ~40° is the mean peak of the multilayer dominated by the thick Pd layer.

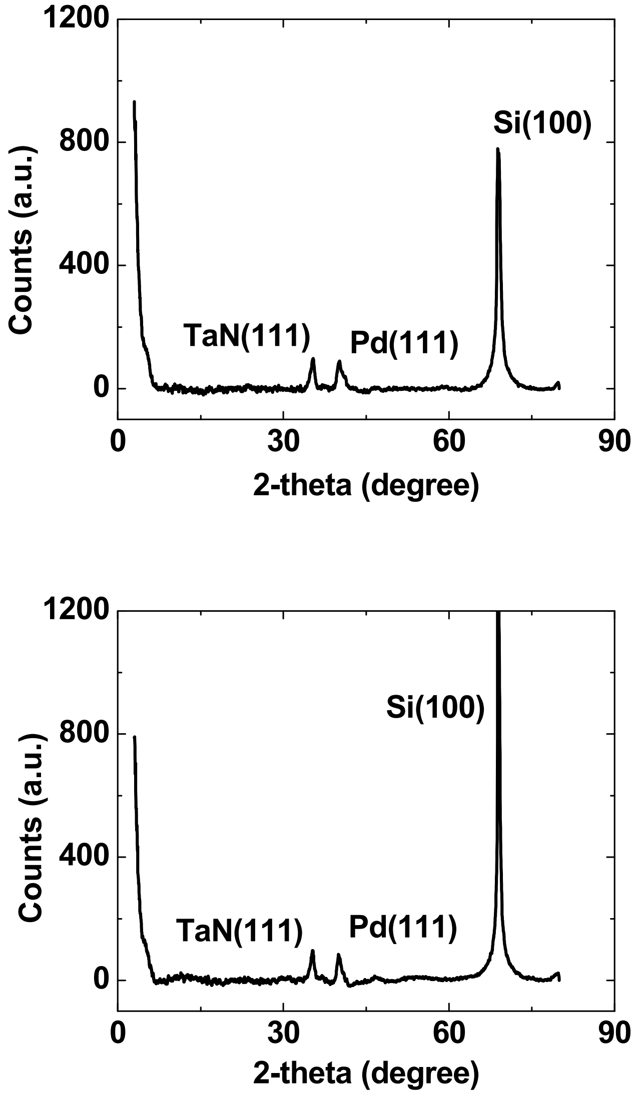

Figure 4.2: The XRD analyses of sample III (top) and sample IV (bottom) which show (111) crystal growth of the spin-valve structure. The (111) peak at ~40° is the mean peak of the multilayer dominated by the thick Pd layer.

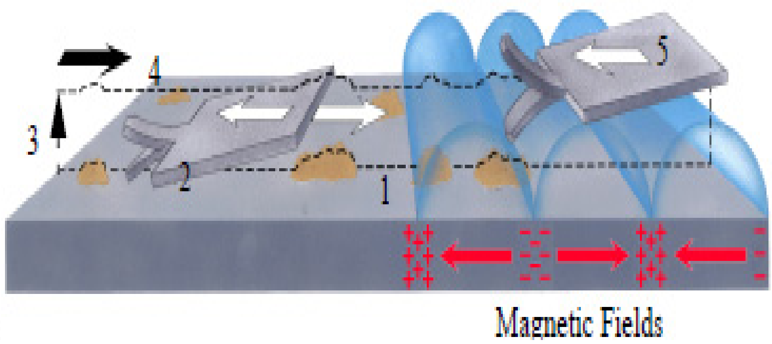

Figure 4.3: Schematic showing MFM measurement. [9] 1,2 -tapping mode surface topography by cantilever, 3- cantilever lifts up a specific height, 4,5-lifted cantilever responds to magnetic field. Copyright © 2000 Digital Instruments Veeco Metrology Group.

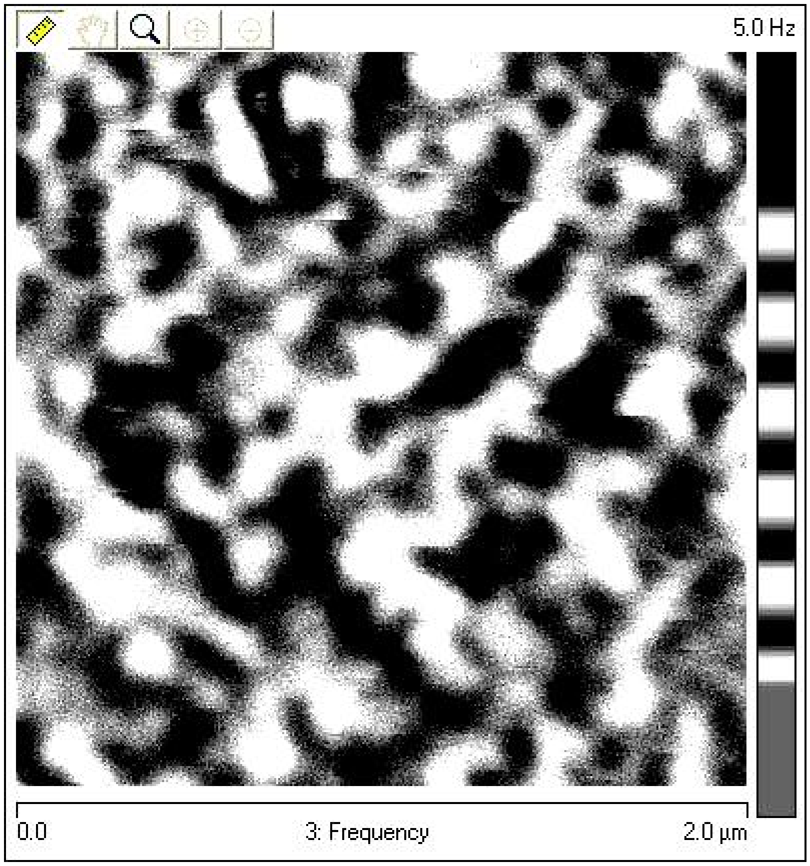

Figure 4.4: Frequency detected MFM scan of demagnetized sample II showing up (black) and down (white) stripe-like domains. The scan area is 2x2 μm^2.

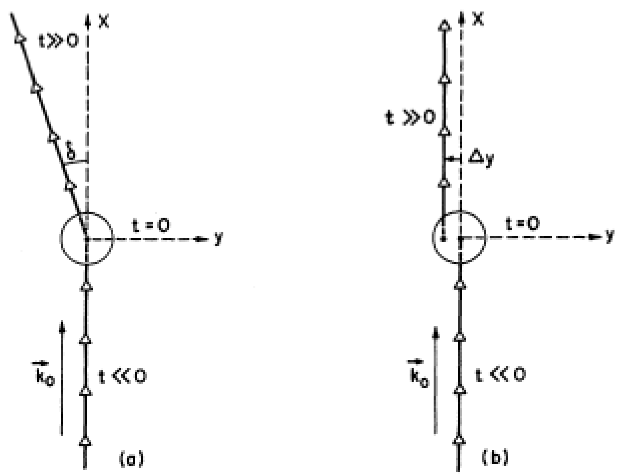

Figure 4.5: Schematics of skew scattering (a) and side-jump components (b) during EHE.[18] The incident direction is parallel to x and spin direction is parallel to z. The two effects are usually superposed. "Copyright (1970) by The American Physical Society."

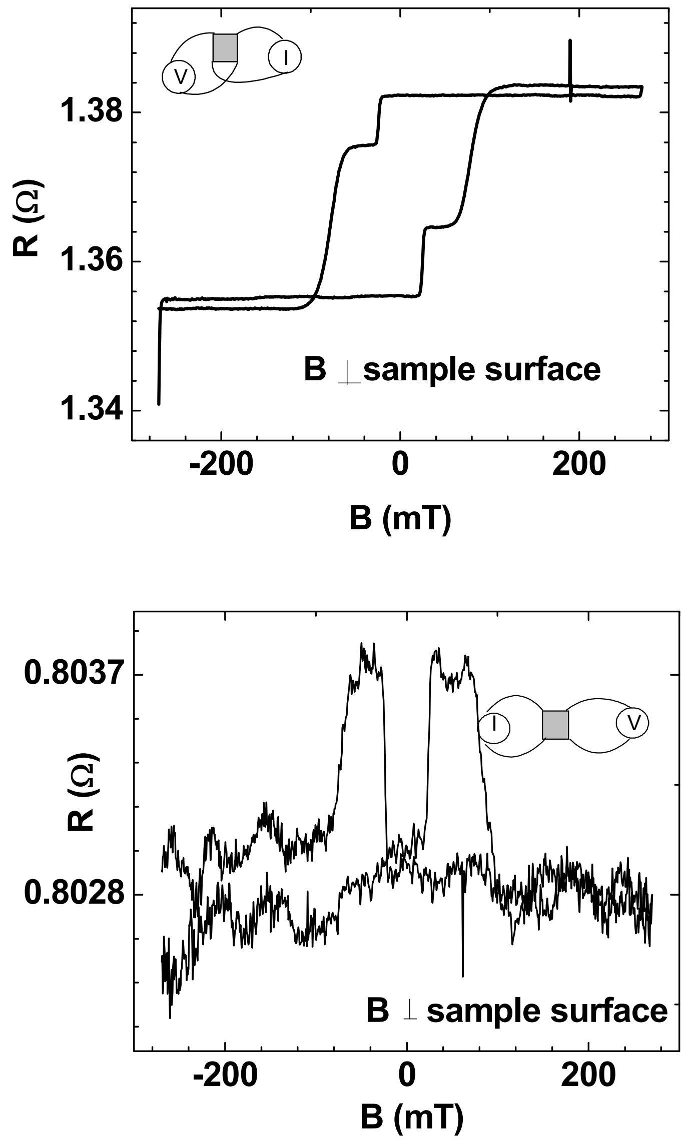

Figure 4.6: EHE (top) and MR (bottom) measurements of sample I with field applied perpendicular to the sample.[13] During EHE measurement, current is applied between cross contacts and voltage is measured across the other cross contacts. In MR measurement, current is applied across parallel contacts and voltage is measured across the other parallel contacts thus eliminating the Hall Effect.

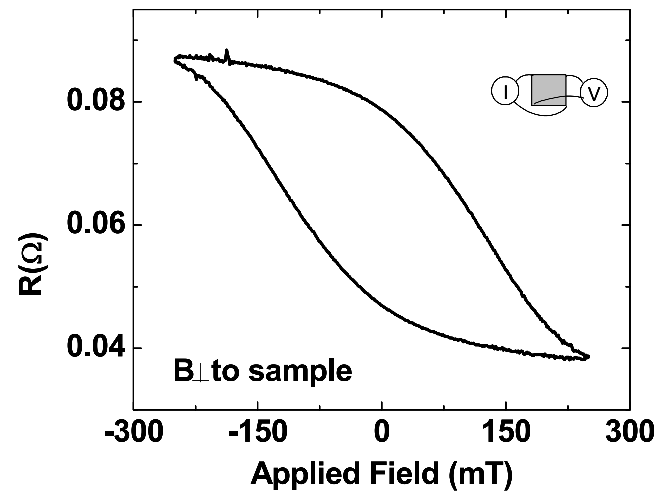

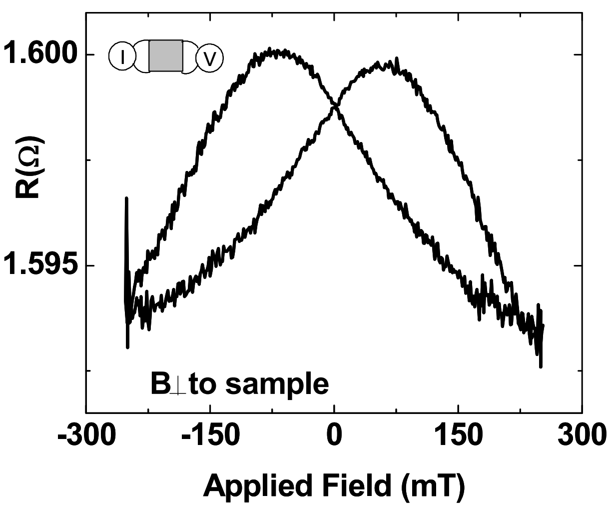

Figure 4.7: EHE (top) and MR (bottom) measurements of sample II with field applied perpendicular to the sample.[13] A broad MR distribution is obtained probably due to magnetization away from easy axis with perpendicular field and also due to the grains in the metal layers deposited by evaporation process.

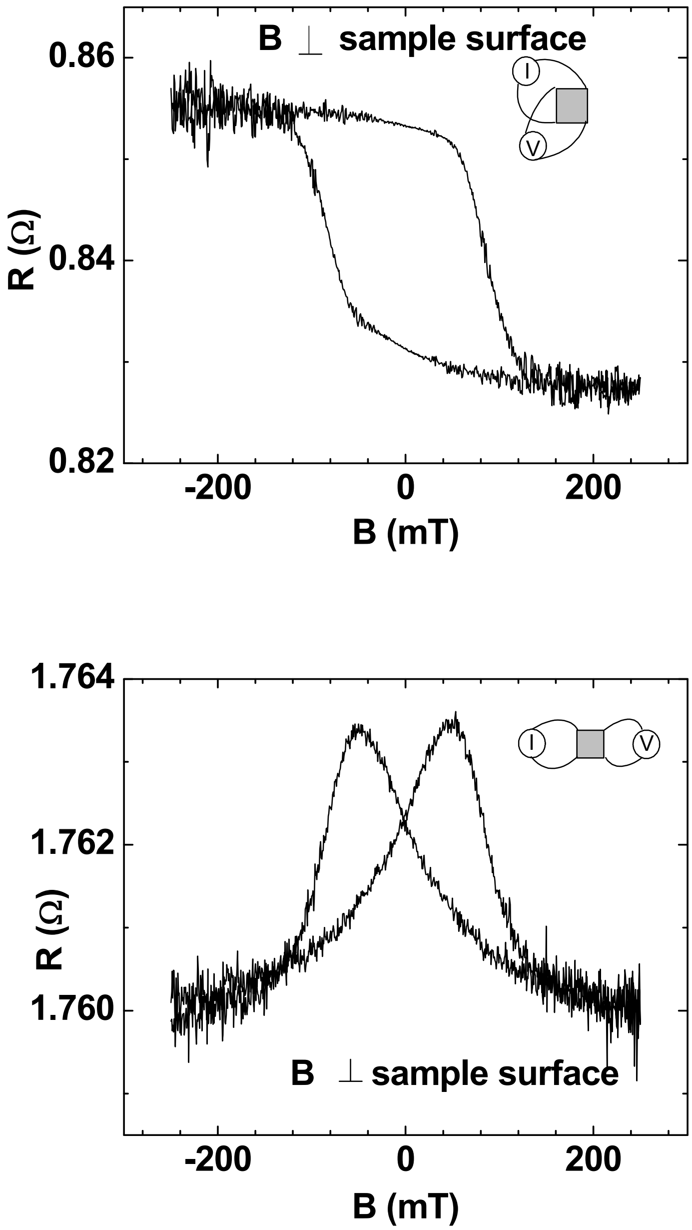

Figure 4.8: EHE (top) and MR (bottom) measurements of sample III with field applied perpendicular to the sample.[13] The MR switching of free layer is slow might be due to the presence of grains in evaporated layers.

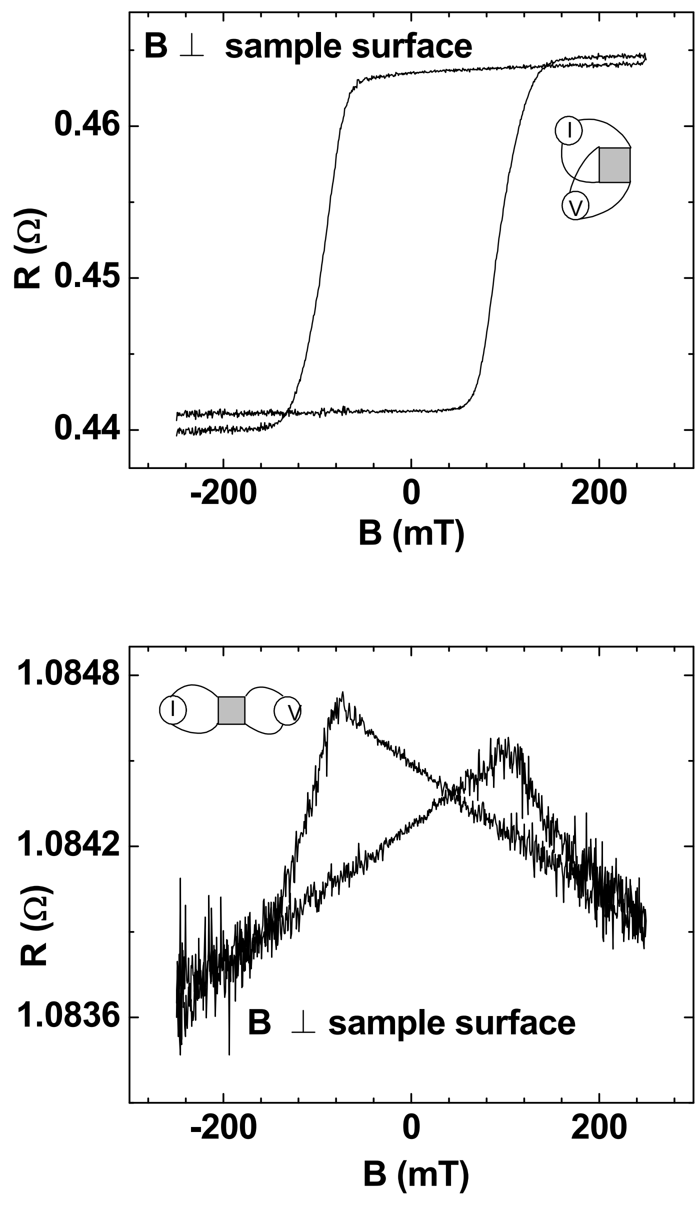

Figure 4.9: EHE (top) and MR (bottom) measurements of sample IV with field applied perpendicular to the sample.[13] A square loop is obtained in EHE because of the PMA reference layer. The MR distribution is broad and weak presumably due to the 90° tilt difference between free and reference layers.

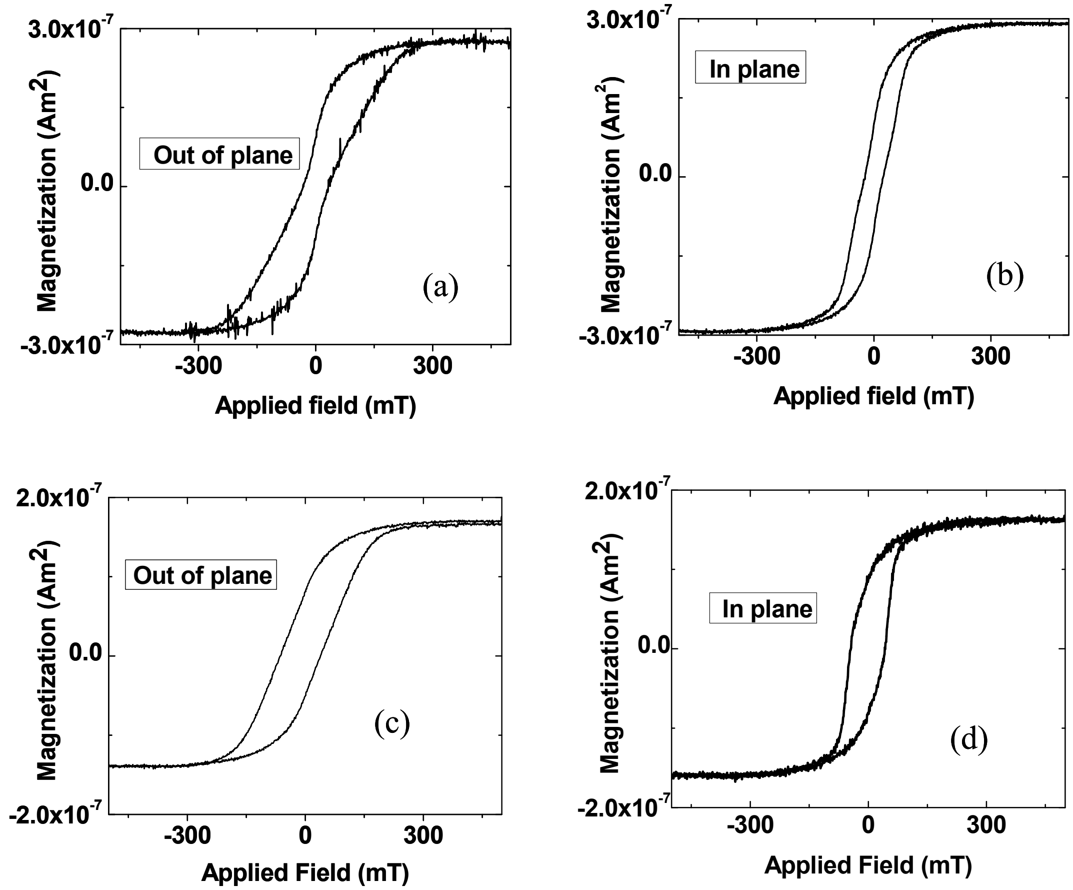

Figure 4.10: VSM measurements of sample II (a) and (b); VSM measurements of only the reference layer (c) and (d). The data are summarized in Table 4.5. The spin-valve M-H loops in (a) and (b) are different from that of reference layer in (c) and (d), as expected. The spin-valve loops exhibit two separate switching corresponding to two individual FM layers. This is due to the little or no exchange coupling between the layers and indicates different hysteresis behavior for free and reference layers.

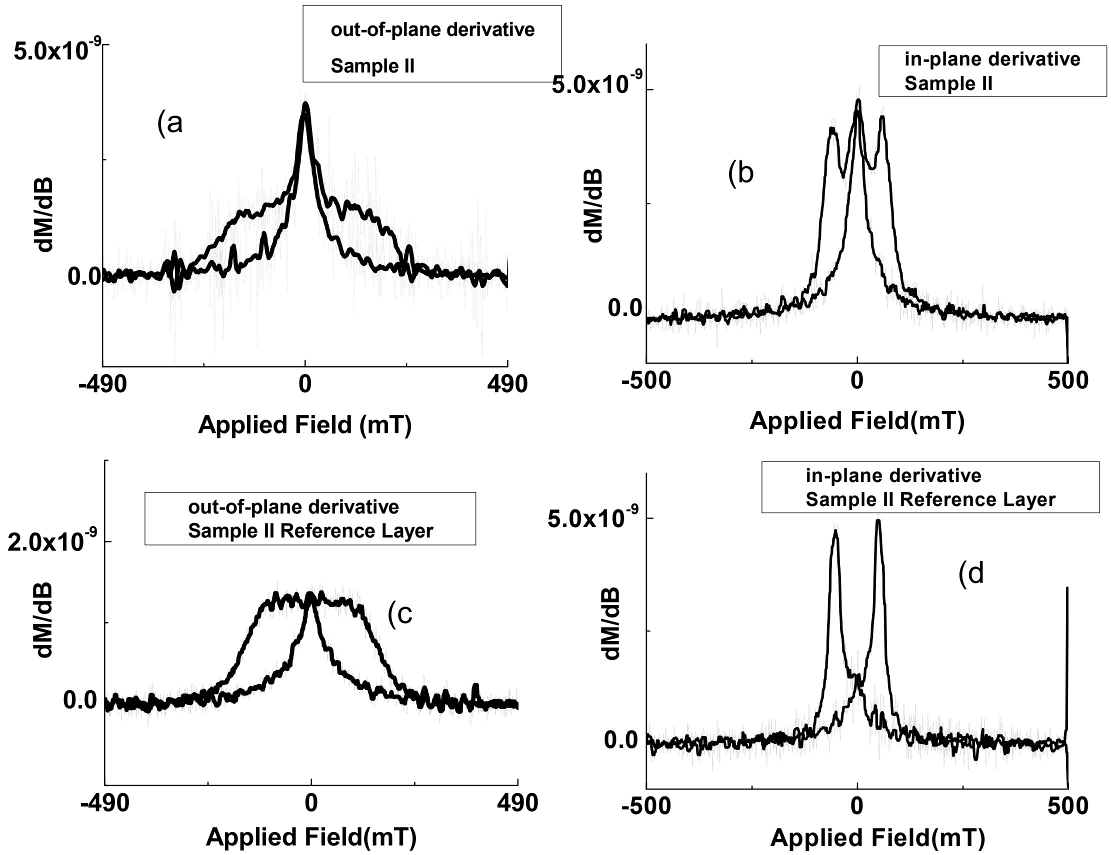

Figure 4.11: The first-order derivatives of Figure 4.10. The reference layer in (c) and (d) show slope change around switching fields. The spin-valve in (a) and (b) show two separate switching events corresponding to two different slopes.

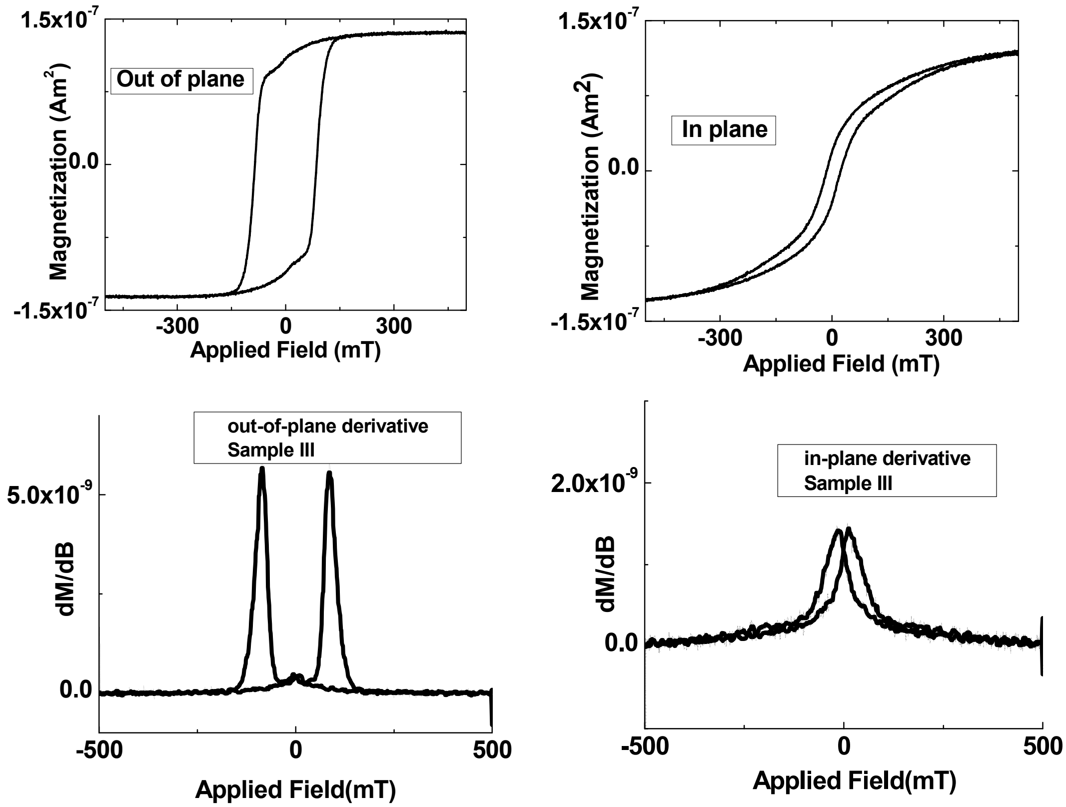

Figure 4.12: VSM measurements of sample III. The data are summarized in Table 4.5. The out-of-plane plot shows a distinct kink indicating different hysteresis behavior for free and reference layers which results from little or no exchange coupling between the layers. The same behavior is observed in the out-of-plane derivative plot (bottom left).

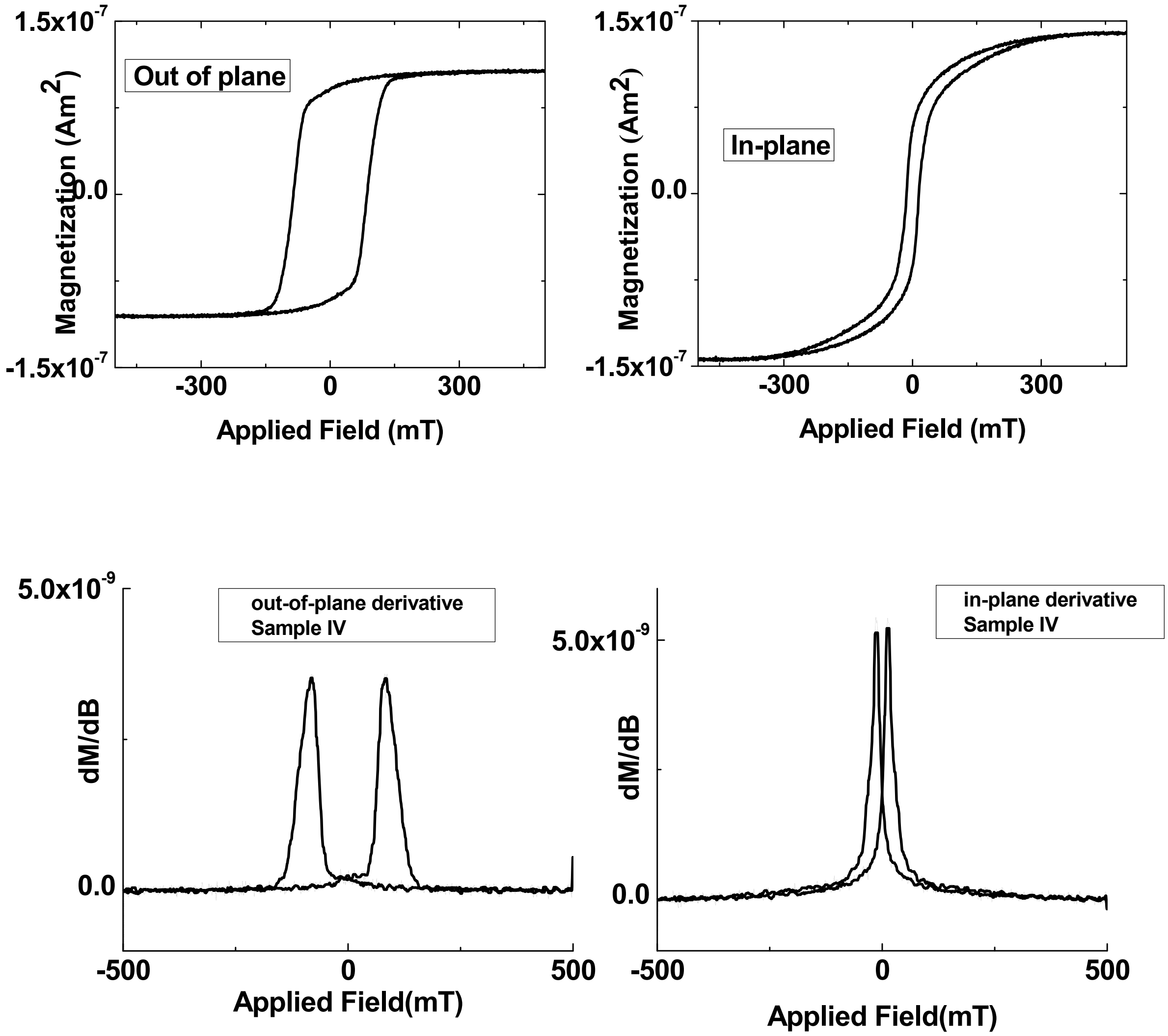

Figure 4.13: VSM measurements of sample IV. The data are summarized in Table 4.5. The free layer is in-plane and reference layer is out-of-plane. The out-of-plane plot shows no distinct kink indicating that free layer magnetization is probably not saturated. The in-plane plot also shows magnetization of one layer only.

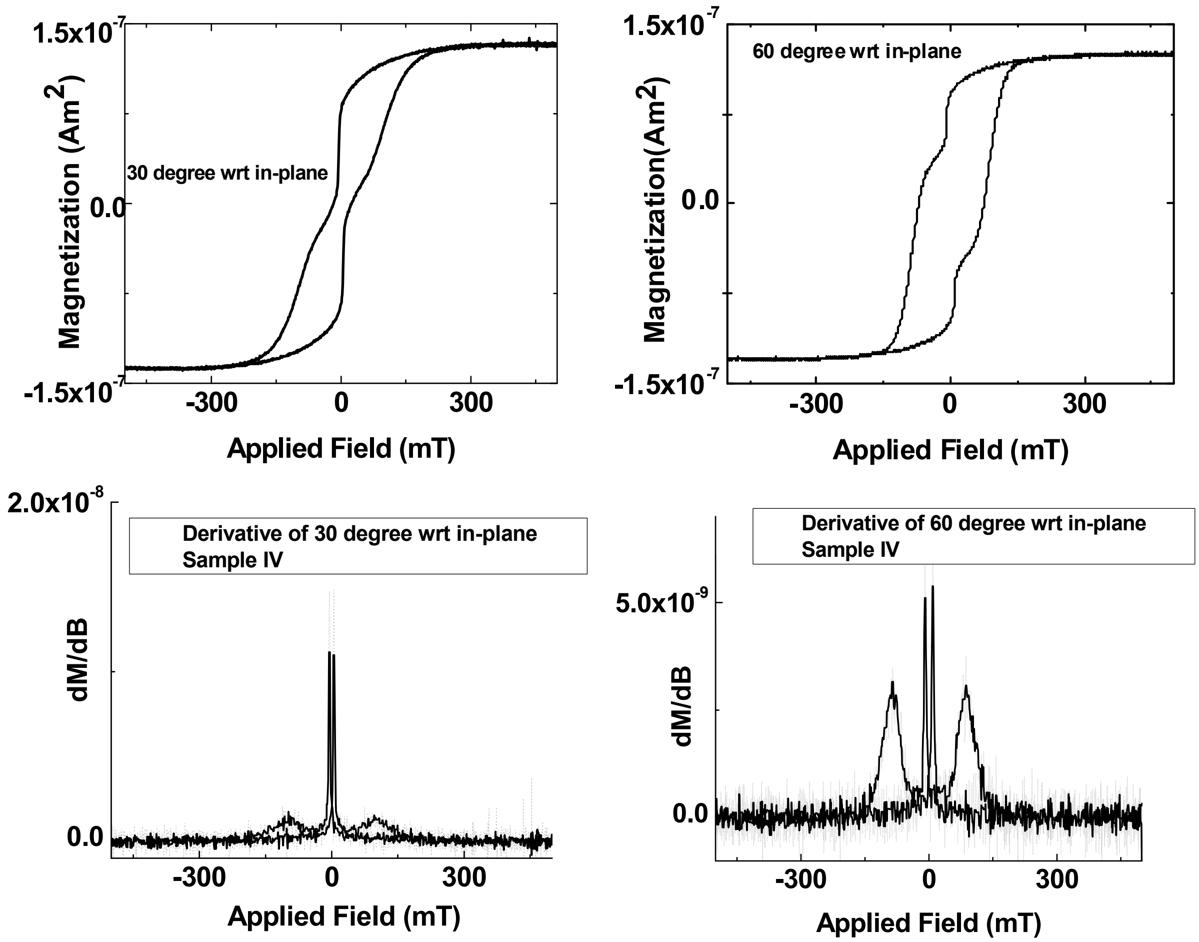

Figure 4.14: Angular VSM measurements of sample IV : (top left) at 30° angle with respect to the plane of the sample, (top right) at 60° angle with respect to the plane of the sample. The bottom left and right figures show respective 1st order derivatives. There are two distinct switching events from two different layers. Comparing the data with Figure 4.13, the lower field switching is presumably from the free layer and the higher field switching is from the reference layer.

Table 4.5: Summary of VSM measurements

Sample II	Sample III	Sample IV
Ms=2.9e-7 Am^2, in-plane = 2.76e-7 Am^2,out-of-plane Hc, in-plane=23mT Hc, out-of-plane=31mT Mr/Ms, in-plane=0.3447, out-of-plane=0.3354 arctan(out-of-plane/in-plane) =44.2 from x-axis =45.7 from z-axis	Ms=1.41e-7 Am^2, in-plane =1.35e-7 Am^2,out-of-plane Hc, in-plane=19mT Hc, out-of-plane=85.4mT Mr/Ms, in-plane=0.1796, out-of-plane=0.8086 arctan(out-of-plane/in-plane) =77.47 from x-axis =12.52 from z-axis	Ms=1.41e-7Am^2, in-plane =1.05e-7Am^2,out-of-plane Hc, in-plane=14.38mT Hc, out-of-plane=85.6mT Mr/Ms, in-plane=0.4235, out-of-plane=0.8580

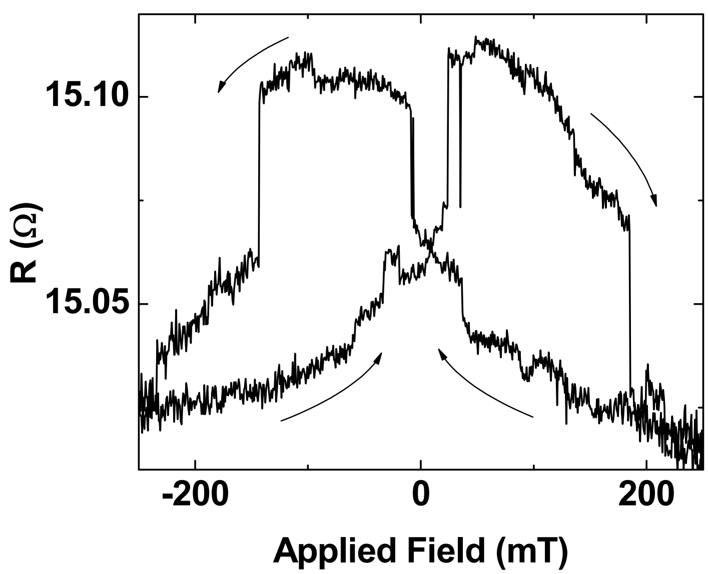

Figure 4.15: MR measurement of sample II with 45° tilt for a fixed dc current of 0.5mA while the magnetic field is varied. The arrows indicate direction of field sweeping. [13]

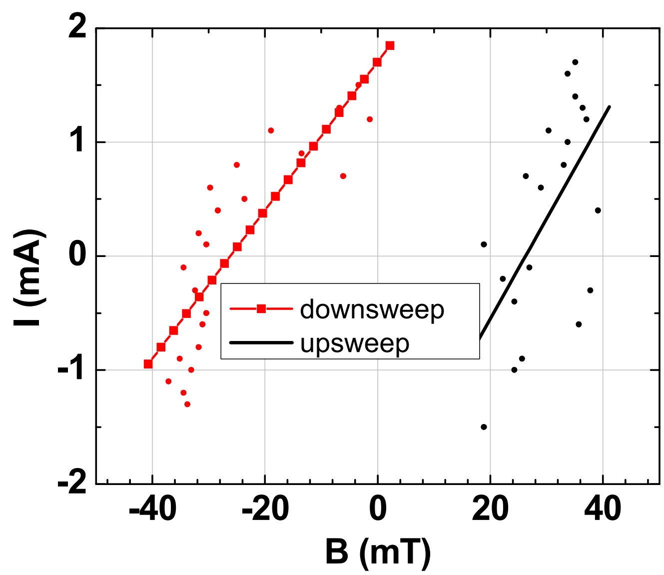

Figure 4.16: Applied current vs the magnetic switching field of sample II. [13] During upsweep, the switching field decreases as more electrons flow through the free layer or negative current increases. Again, as positive current increases, electrons are flowing through the reference layer which makes free layer switching difficult and switching field increases to higher values. During downsweep the free layer switching becomes difficult with negative current and easier with positive current indicating some biasing effect. The reference layer switching shows little dependence on current (not shown).

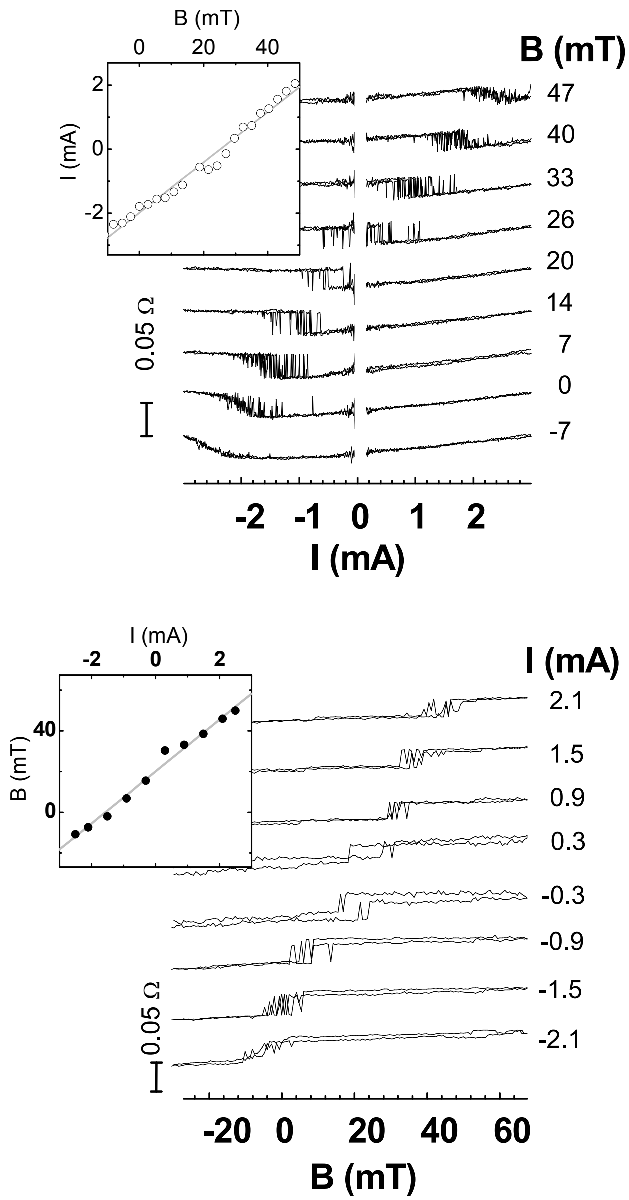

Figure 4.17: I-V (top) and MR (bottom) data for sample II where only free layer is switched by varying current or magnetic field, respectively. [13] As dc current is swept from negative to positive values, and vice versa, free layer switching is observed and the hysteresis loop can be exchange biased by applying a magnetic field perpendicular to the sample. Similar phenomena are observed with sweeping the magnetic field at fixed dc current levels.

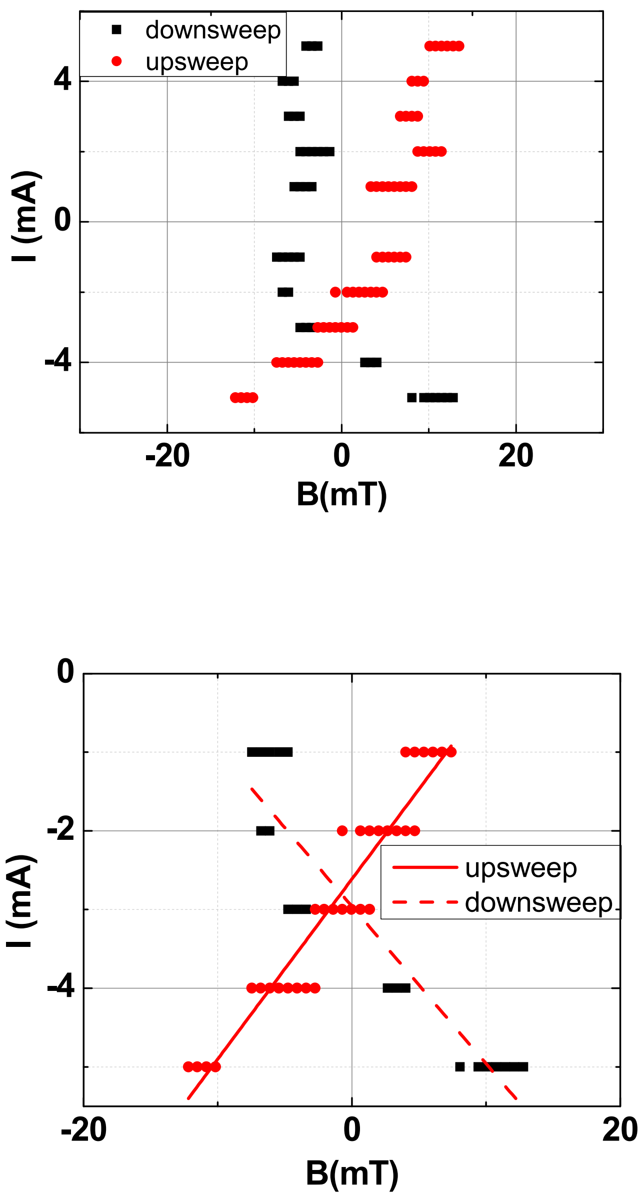

Figure 4.18: The applied current vs switching field for sample III with 12° tilt. [13] The bottom figure shows linear fit on part of the data from the top figure. During upsweep, the switching field moves towards more negative values as negative current increases. During downsweep, the switching field moves towards positive values as negative current increases. The STT effect changes the magnitude of slope at positive currents.

Table 4.6: Summary of point contact measurement

Sample	Point-contact resistance (ohm)	Point-contact radius (nm)	Switching Current density (A/cm^2)	Slope of STT (T/A)
II	26.4	3.41	Upsweep=6.07×10^9	526.31
			Downsweep=4.65×10^9	1149.4
III	12	5.33	Upsweep=2.9×10^9	323.6
			Downsweep=3.36×10^9	-370.3

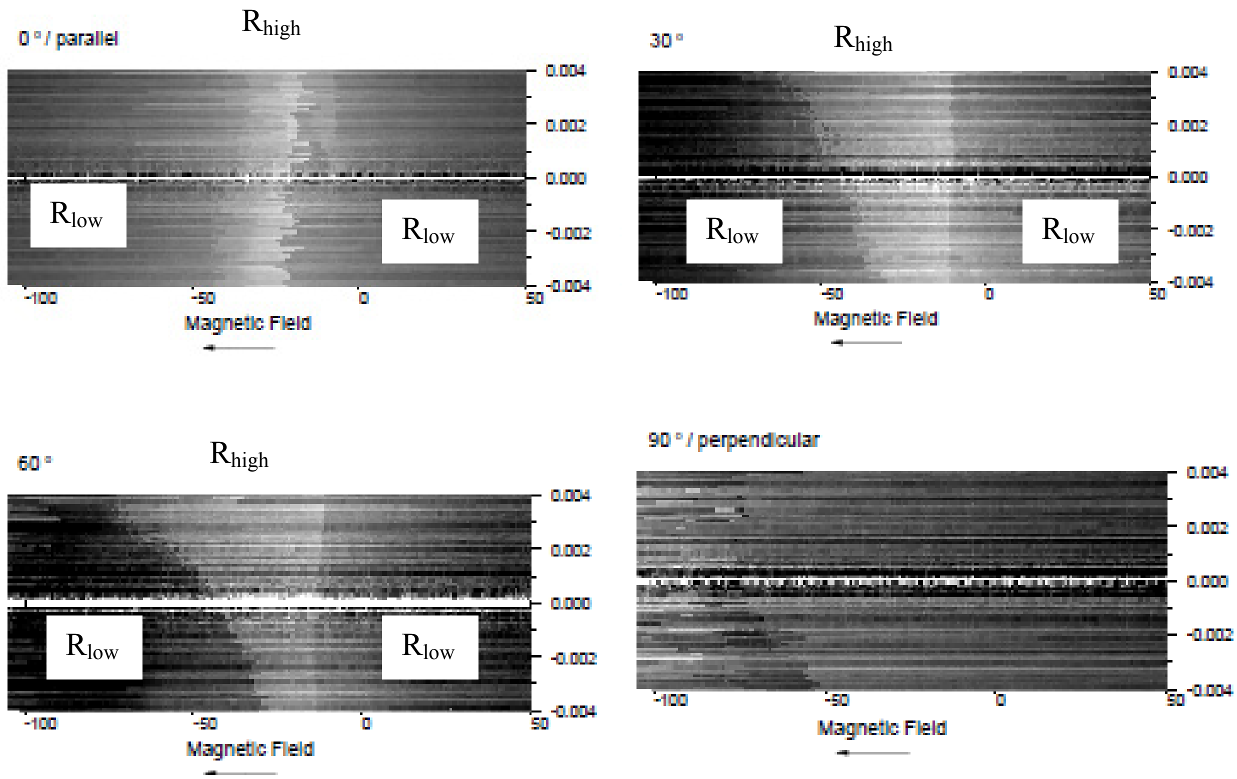

Figure 4.19: 3D plots of downsweep MR measurement. Magnetic field is shown in x-axis, dc current in y-axis, and resistance values in color.[13] Different colors indicate different resistance values (dark- low, light-high). The field was applied at different angular orientations with respect to the plane of the sample. Spin-torque-effect is observed as the resistance change varies with applied field, especially at 30° and 60°. At 30° and 60°, the light antiparallel region broadens with positive current. At 90° the free layer switching is very slow and resistance change is not distinct similar to MR results with applied field only. At 0° the switching field corresponding to resistance change has a distribution probably because of the angular orientation of the PMA reference layer with in-plane applied field.

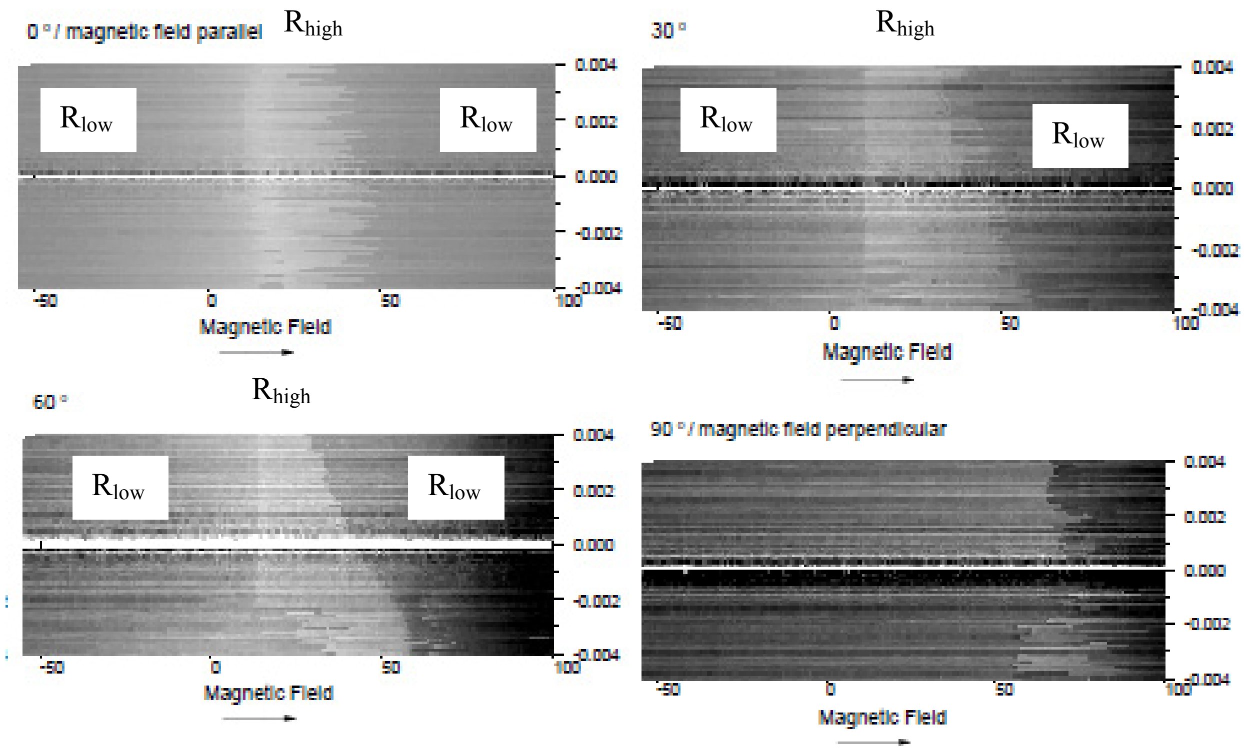

Figure 4.20: 3D plots of upsweep MR measurement. Magnetic field is shown in x-axis, dc current in y-axis and resistance value in color contrast.[13]Different colors indicate different resistance values (dark- low, light-high). The field was applied at different angular orientations with respect to the plane of the sample. Spin-torque-effect is observed as the resistance change varies with applied field, especially at 30° and 60°. At 30° and 60°, the light antiparallel region broadens with negative current. At 90° the free layer switching is very slow and resistance change is not distinct similar to MR results with applied field only. At 0° the switching field corresponding to resistance change has a distribution probably because of the angular orientation of the PMA reference layer with in-plane applied field.

Chapter 5: Summary and Future work

5.1 Summary

This dissertation focused on different high density nonvolatile memory structures. The first part of the work discusses hybrid MOS capacitors with fullerene molecules as a floating gate. Hybrid fullerene MOS capacitors were fabricated in a CMOS-compatible process flow and material as well as electrical characterization was carried out. The MOS capacitors demonstrate nonvolatile memory operation at room temperature. From the device data it can be concluded that program/erase mechanism in fullerene devices is FN tunneling; however, retention is determined by trap-assisted tunneling. Molecular orbital energies associated with the charge states in different dielectric environments were calculated to explain the device performance. Different high-k dielectric oxides were compared as tunnel and control oxides to optimize the memory operation. The dielectric permittivity as well as band offset of the control oxide needs to be increased to achieve low power operation and good data retention.

The second part of the dissertation focused on simulation and fabrication of PMA spin-valves with different tilt angles to achieve low critical switching current. Tilting of the reference layer introduces precessional switching which requires smaller energy and shorter time to switch the free layer. However, the amount of tilting needs to be optimized to achieve faster switching as some of the tilting configuration may not aide the spin-transfer switching. Next, fabrication and characterization of spin-valves were discussed with different amount of tilted magnetization. The difference in tilt was obtained by varying mainly the thickness of Co and Ni layers in multilayer structures. The tilting is quantified through VSM measurement. Material characterization was done to confirm a uniform, smooth film deposition. The STT effect of different samples was studied through point contact measurements and compared. The STT effect is not observed in the PMA sample with 0° tilt probably due to the presence of Pt near the Cu barrier layer as Pt shows strong spin-scattering effect. The spin-valve with 45° tilt shows stronger STT effect over a wide range of dc current compared to the spin-valve with 12° tilt.

5.2 Proposed future simulation of spin-valve structure

The simulation of spin-valve structures in Chapter 3 are done at 0 K without any temperature effects accounted for. However, temperature effects are important to study retention characteristics of memory devices. Thermally-assisted switching may flip the memory state and cause errors especially in the nanoscale devices. Thermal effects may also help the original bit switching if the device is designed accordingly. If the continuous free layer is replaced by nanomagnets, then the thermal effects may determine the scaling, material properties, and shape of the nanomagnets. The future simulations should include temperature effects on STT switching. Another interesting improvement would be to include crystal lattice of different layers in the simulation and study strain and interface effects on MR. The effects of nonuniform effective field and canting of the domains in the tilted structures also need to be studied in detail.

5.2 Proposed future fabrication and characterization of PMA spin-valves

The main focus of this work was to fabricate tilted spin-valves and study their STT effect through point-contact measurements. The study can be extended to samples with dual spin-valves where the free layer will be sandwiched between two reference layers: one PMA and the other in-plane. Another design may have 90° tilt with PMA free layer and in-plane reference layer. For all samples, the free layer of tilted spin-valve needs to be optimized to achieve the required retention and fast switching. The next advancement would be to make nanoscale devices through stencil mask and do pulsed measurement to compare the devices with ITRS specifications. Magnesium oxide may be used as a barrier layer in the nanoscale devices which will improve MR ratio. The damping constant of the free layer can be improved by contact metal engineering while the saturation magnetization, Ms, can be further lowered by material engineering.

Appendices

Appendix 1: MIF code for spin-transfer-torque

```
# MIF 2.1
# MIF Example File: spinvalve_j.mif
# Description: Spin valve example, with no exchange coupling between the
#  layers.
#
set pi [expr 4*atan(1.0)]
set mu0 [expr 4*$pi*1e-7]
set gt [expr 1/650e3]
 set gt2 [expr 1/500e3]
Specify Oxs_ImageAtlas:top {
  xrange {0 90e-9}
  yrange {0 45e-9}
  zrange {9e-9  12e-9}
viewplane xy
  image elp_spin.bmp
colormap
{black cotop
white nm
} }
Specify Oxs_MultiAtlas:atlas {
   atlas :top
   atlas { Oxs_ImageAtlas:spacer {
       xrange {0 90e-9}
```

```
      yrange {0 45e-9}
      zrange {6e-9 9e-9}
viewplane xy
  image elp_spin.bmp
colormap
{black cuspacer
white nm
}   }   }
   atlas { Oxs_ImageAtlas:bottom {
      xrange {0 90e-9}
      yrange {0 45e-9}
      zrange {0 6e-9}
viewplane xy
  image elp_spin.bmp
colormap
{black cobottom
white nm
}   }   }
}
Specify Oxs_UniaxialAnisotropy {
 K1 { Oxs_AtlasScalarField {
    atlas :atlas
default_value 0
    values {
      cotop    1.1e5
```

```
        cobottom  6.6e5
      cuspacer 0
    } }}
 axis { Oxs_AtlasVectorField {
    atlas :atlas
    norm 1
default_value {0 0 0}
    values {
       cotop {0 0 1}
       cuspacer {0 0 1}
       cobottom {0 0 1}
   } }}}
Specify Oxs_RectangularMesh:mesh {
  cellsize {3e-9 3e-9 3e-9}
  atlas :atlas
}
Specify Oxs_UniformExchange {
A  {13e-12}}
Specify Oxs_Demag {}
Specify Oxs_AtlasVectorField:topmz {
atlas :top
default_value {0 0 0}
values {
 cotop {0 0 1}
}
```

```
}
Specify Oxs_AtlasVectorField:botmz {
atlas :atlas
default_value {0 0 0}
values {
 cobottom {0 0 1}
}}
Specify Oxs_SpinXferEvolve:evolve [subst {
  alpha 0.1
    mp { 0 0 1}
  J 1e12
  P 0.4
  Lambda 2
  J_profile Jprofile
  J_profile_args total_time
do_precess 1
}]
# Driver
Specify Oxs_TimeDriver [subst {
 basename spinvalve_j
 evolver :evolve
 comment {1 deg/ns = 17453293 rad/sec; If Ms=8.6e5, and lambda is small,
         then mxh=1e-6 translates into dm/dt = 2e5 rad/sec = 0.01 deg/ns}
 comment {stopping_dm_dt 1e-9}
stopping_time 25e-9
```

```
 mesh :mesh
 Ms  { Oxs_AtlasScalarField {
    atlas :atlas
    default_value 0
    values {
      cotop 650e3
      cobottom 500e3
cuspacer 0
    }
 }}
 m0 { Oxs_AtlasVectorField {
  atlas :atlas
default_value {0 0 0}
  values {
     cotop {0   0  1}
     cobottom {0  0  1}
    cuspacer {0 0 1}
  }
  norm 1.0
 }}
user_output {
name "mztop"
source_field Oxs_TimeDriver::Magnetization
select_field :topmz
exclude_0_Ms 1
```

```
normalize 1
user_scaling $gt
}
user_output {
name “mzbot”
source_field Oxs_TimeDriver::Magnetization
select_field :botmz
exclude_0_Ms 1
normalize 1
user_scaling $gt2
}
}]
proc Jprofile { t } {
   set scale 0.0;
   if {$t>0.5e-9 & $t<2.5e-9} {
      set scale -1.0
   } elseif {$t>12.5e-9 & $t<14.5e-9} {
      set scale 1.0
   }
   return $scale
}
```

Appendix 2: MIF code for applied field

```
# MIF 2.1
```

```
# MIF Example File: spinvalve_h.mif
# Description: Spin valve example, with no exchange coupling between the
#  layers.
#
set pi [expr 4*atan(1.0)]
set mu0 [expr 4*$pi*1e-7]
set gt [expr 1/650e3]
 set gt2 [expr 1/500e3]
Specify Oxs_ImageAtlas:top {
  xrange {0 90e-9}
  yrange {0 45e-9}
  zrange {9e-9  12e-9}
viewplane xy
  image elp_spin.bmp
colormap
{black cotop
white nm
}
 }
Specify Oxs_MultiAtlas:atlas {
   atlas :top
   atlas { Oxs_ImageAtlas:spacer {
       xrange {0 90e-9}
       yrange {0 45e-9}
       zrange {6e-9 9e-9}
```

```
viewplane xy
  image elp_spin.bmp
colormap
{black cuspacer
white nm
}
   }   }
   atlas { Oxs_ImageAtlas:bottom {
       xrange {0 90e-9}
       yrange {0 45e-9}
       zrange {0 6e-9}
viewplane xy
  image elp_spin.bmp
colormap
{black cobottom
white nm
}
   }   }
}
Specify Oxs_UniaxialAnisotropy {
 K1 { Oxs_AtlasScalarField {
    atlas :atlas
default_value 0
    values {
       cotop    1.1e5
```

```
      cobottom  6.6e5
     cuspacer 0
    } }}
 axis { Oxs_AtlasVectorField {
    atlas :atlas
    norm 1
default_value {0 0 0}
    values {
       cotop {0 0 1}
       cuspacer {0 0 1}
       cobottom {0 0 1}
   } }}}
Specify Oxs_RectangularMesh:mesh {
  cellsize {3e-9 3e-9 3e-9}
  atlas :atlas
}
Specify Oxs_UniformExchange {
A  {13e-12}}
# Stepped applied field
Specify Oxs_UZeeman [subst {
  multiplier [expr 0.001/$mu0]
  Hrange {
     {    5  0  500  -2  0 -200  5 }
{    -2  0  -200  -10  0 -1000  20 }
     {   -10  0  -1000  2  0  200   5 }
```

```
{    2  0  200  10  0 1000  20 }
  }
}]
Specify Oxs_Demag {}
Specify Oxs_RungeKuttaEvolve:evolve {
  alpha 0.1
}
Specify Oxs_AtlasVectorField:topmz {
atlas :top
default_value {0 0 0}
values {
 cotop {0 0 1}
}}
Specify Oxs_AtlasVectorField:botmz {
atlas :atlas
default_value {0 0 0}
values {
 cobottom {0 0 1}
}}
# Driver
Specify Oxs_TimeDriver [subst {
 basename spinvalve_h
 evolver :evolve
 comment {1 deg/ns = 17453293 rad/sec; If Ms=8.6e5, and lambda is small,
        then mxh=1e-6 translates into dm/dt = 2e5 rad/sec = 0.01 deg/ns}
```

```
stopping_dm_dt 0.01
 mesh :mesh
 Ms  { Oxs_AtlasScalarField {
     atlas :atlas
     default_value 0
     values {
        cotop 650e3
        cobottom 500e3
cuspacer 0
     }
 }}
 m0 { Oxs_AtlasVectorField {
   atlas :atlas
default_value {0 0 0}
   values {
      cotop {0   0  1}
      cobottom {0  0  1}
     cuspacer {0 0 1}
   }
   norm 1.0
 }}
user_output {
name "mztop"
source_field Oxs_TimeDriver::Magnetization
select_field :topmz
```

```
exclude_0_Ms 1
normalize 1
user_scaling $gt
}
user_output {
name “mzbot”
source_field Oxs_TimeDriver::Magnetization
select_field :botmz
exclude_0_Ms 1
normalize 1
user_scaling $gt2
}
}]
```

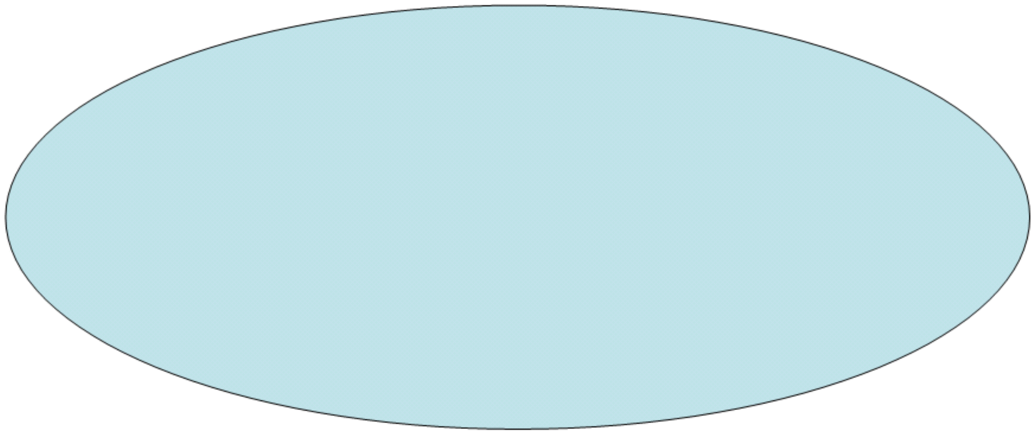

Figure A.1: Top-view of the simulated spin-valve in elp_spin.bmp

References

[R1]http://en.wikipedia.org/wiki/Nonvolatile_memory;http://creativecommons.org/licenses/by-sa/3.0/

[R2]G. E. Moore, Int. Elec. Dev. Meeting 21, 11 (1975).

[R3]S.E. Thompson, R.S. Chau, T. Ghani, K. Mistry, S. Tyagi, and M.T. Bohr, IEEE Tran. Semi. Manu. 18, 26 (2005).

[R4]K.W. Guarini, C.T. Black, Y. Zhang, I.V. Babich, E.M. Sikorski, and L.M. Gignac, IEEE Int. Elect. Dev. Meeting Tech. Dig., 22.2.1 (2003).

[R5]C.Y. Lu, K.Y. Hsieh, and R, Liu, Microelec. Eng. 86, 283 (2009).

[R6]R.F. Steimle, R. Muralidhar, R. Raoa, M. Sadd, C.T. Swift, J. Yater, B. Hradsky, S. Straub, H. Gasquet, L. Vishnubhotla, E.J. Prinz, T. Merchant, B. Acred, K. Chang, and B.E. White, Jr., Microelec. Reliability 47, 585 (2007).

[R7]C.M. Compagnoni, D. Ielmini, A.S. Spinelli, and A.L. Lacaita, IEEE Trans. Elec. Dev. 52, 2473 (2005).

[R8]J. Sarkar, Ph.D. dissertation, The University of Texas at Austin, Austin, TX (2007).

[R9]S. Tang, C. Mao, Y. Liu, D.Q. Kelly, and S.K. Banerjee, IEEE Trans. Electron. Dev. 54, 433 (2007).

[R10]I. Yamashita, Thin Solid Films 393, 12 (2001).

[R11]S. Gowda, G. Mathur, Q. Li, S. Surthi, and V. Misra, IEEE Trans. Nanotech. 5, 258 (2006).

[R12]C. Li, W. Fan, B. Lei, D. Zhang, S. Han, T. Tang, X. Liu, Z. Liu, S. Asano, M. Meyyappan, J. Han, and C. Zhou, Appl. Phys. Lett. 84, 1949 (2004).

[R13]H. Majumdar, J. Baral, R. Osterbacka,O. Ikkala, and H. Stubb, Org. Electron. 6,188 (2005).

[R14]J. Scott, and L. Bozano, Adv. Mater.19, 1452 (2007).

[R15]T. Hou, U. Ganguly, and E. C. Kan, Appl. Phys. Lett. 89, 253113 (2006).

[R16]Y.Y. Chen, C.H. Chien, and J.C. Lou, Jpn. J. Appl. Phys. 44,1704 (2005).

[R17]C. Sargentis, K. Giannakopoulos, A. Travlos, and D.Tsamakis, Surf. Sci. 601, 2859 (2007).

[R18]C. K. Maiti, S. K. Samanta, S. Chatterjee, G. K. Dalapati, and L. K. Bera, Solid state Elec. 48, 1369 (2004).

[R19]D.C. Ralph, and M.D. Stiles, J. Magn. Magn. Mater. 320, 1190 (2008).

[R20]T. Kishi, H. Yoda, T. Kai, T. Nagase, E. Kitagawa, M. Yoshikawa, K. Nishiyama, T. Daibou, M. Nagamine, M. Amano, S. Takahashi, M. Nakayama, N.

Shimomura, H. Aikawa, S. Ikegawa, S. Yuasa, K. Yakushiji, H. Kubota, A. Fukushima, M. Oogane,T. Miyazaki, and K. Andoet, IEEE Int. Elect. Dev. Meeting Tech. Dig. 2008.

[R21]J.C. Slonczewski, J. Magn. Magn. Mater. 159 (1996).

[R22]L. Berger, Phys. Rev. B 54 , 9353(1996).

[R23]M. Tsoi, A.G.M. Jansen, J. Bass, W.C. Chiang, M. Seck, V. Tsoi, and P. Wyder, Phys. Rev. Lett. 80, 4281 (1998).

[R24]X. Zhu, PhD dissertation, Carnegie Mellon University, 2007.

[R25]S. Yuasa, and D. D. Djayaprawira, J. Phys. D: Appl. Phys. 40, R337(2007).

[R26]J.G. Zhu, Proceedings of the IEEE 96, 1786 (2008).

[R27]S. Mangin, D. Ravelosona, J. A. Katine, M. J. Carey, B. D. Terris, and E. E. Fullerton, Nature Mat. 5 , 210 (2006).

[R28]D. C. Worledge, G. Hu, P. L. Trouilloud, D. W. Abraham, S. Brown, M. C. Gaidis, J. Nowak, E. J. O'Sullivan, R. P. Robertazzi, J. Z. Sun, and W. J. Gallagher, IEEE Int. Elect. Dev. Meeting Tech. Dig. 2010.

[R29]M. T. Johnson, P. J. H. Bloemenz, F. J. A. Broeder and J. J. Vries, Rep. Prog. Phys. 59, 1409 (1996).

[R30]G.H.O. Daalderop, P.J.Kelly, and F.J.A. Broeder , Phys. Rev. Lett. 68, 682 (1992).

[R31]E.B. Myers, D.C. Ralph, J.A. Katine, R.N. Louie, and R.A. Buhrman, Science 285, 867 (1999).

[R32]Z. Wei, PhD dissertation,The University of Texas at Austin, 2008.

[R33]G. Wexler, Proc. Phys. Soc. 89, 927 (1966).

[R34]L. Chiang, J. Swirczewski, C. Hsu, S. Chowdhury, S. Cameron, and K. Creegan, J. Chem. Soc. , Chem. Commun., 1791(1992).

[R35]A. Pirkle, R. M. Wallace, and L. Colombo, Appl. Phys. Lett. 95, 133106 (2009).

[R36]F. Ferdousi, J. Sarkar, S. Tang, D. Shahrjerdi, T. Akyol, E. Tutuc, and S. K. Banerjee, J. Elec. Mat. 38, 438 (2009).

[R37]D.C. Gilmer, N. Goel, H. Park, C. Park, S. Verma ,G. Bersuker, P. Lysaght, H.H. Tseng, P.D. Kirsch, K.C. Saraswat, and R. Jammy, IEEE Int. Elec. Dev. Meet. Tech. Dig. 2009.

[R38]W. Green, S. Gorun, G. Fitzgerald, P. Fowler, A. Ceulemans, and B. Titeca, J. Phys. Chem. 100, 14892 (1996).

[R39]U. Ganguly, C. Lee, and E. C. Kan, MRS Proc. NI6.3.1 (2004).

[R40]Y. Liu, S. Tang, and S. K. Banerjee, Appl. Phys. Lett. 88, 213504 (2006).

[R41]M. Okutan, H.I. Bakan, K. Korkmaz, and F. Yakuphanoglu, Physica B 355, 176 (2005).

[R42]F. Ferdousi, M. Jamil, H. Liu, S. Kaur, D. Ferrer, L. Colombo, and S. K. Banerjee, IEEE Tran. Nanotech.(in press).

[R43]C. Sargentis, K. Giannakopoulos, A. Travlos, and D. Tsamakis, Surf. Sci. 601, 2859 (2007).

[R44]T. L. Gilbert, Phys. Rev.100, 1243 (1955).

[R45]L. Landau, and E. Lifshitz, Physik. Z. Sowjetunion 8, 153–169 (1935).

[R46]J. Xiao, A. Zangwill, and M. D. Stiles, Phys. Rev. B 70, 172405 (2004).

[R47]M. J. Donahue, and D. G. Porter, OOMMF User's Guide, Version 1.0, National Institute of Standards and Technology Report No. NISTIR 6376, September 1999 (unpublished).

[R48]M. A. Zimmler, B. Ozyilmaz, W. Chen, A. D. Kent, J. Z. Sun, M. J. Rooks, and R. H. Koch, Phys. Rev. B 70, 184438(2004).

[R49]D. E. Nikonov, G. I. Bourianoff,G. Rowlands, and I. N. Krivorotov, J. App. Phys. 107, 113910 (2010).

[R50]L. Berger, J. Appl. Phys. 93, 7693 (2003).

[R51]A. D. Kent, B. Ozylimaz, and E. Barco, Appl. Phys. Lett. 84, 3897 (2004).

[R52]P. M. Braganca, O. Ozatay, A. G. F. Garcia, O. J. Lee, D. C. Ralph, and R. A. Buhrman, Phys. Rev. B 77, 144423 (2008).

[R53]O. J. Lee, V. S. Pribiag, P. M. Braganca, P. G. Gowtham, D. C. Ralph, and R. A. Buhrman, Appl. Phys. Lett. 95, 012506 (2009).

[R54]R. Law, E. L. Tan, R. Sbiaa, T. Liew, and T. C. Chong, Appl. Phys. Lett. 94, 062516 (2009).

[R55]C.L. Wang, S.H. Huang, C.H. Lai, W.C. Chen, S.Y. Yang, K. H. Shen, and H.Y. Bor, J. Phys. D: Appl. Phys. 42 , 115006(2009).

[R56]G. Csaba, P. Lugli, M. Becherer, D. S. Landsiedel, and W. Porod, J. Comput. Electron 7, 454 (2008).

[R57]J. H. Jung, B. Jeong, S. H. Lim, and S.R. Lee, App. Phys. Exp. 3, 023001(2010).

[R58]R. Law, R. Sbiaa, T. Liew, and T. C. Chong, Appl. Phys. Lett. 91, 242504 (2007).

[R59]J.H. Park, C. Park, T. Jeong, M. T. Moneck, N. T. Nufer, and J.G. Zhu, J. App. Phys. 103, 07A917(2008).

[R60]A. E. Kaloyeros, X. Chen, T. Stark, K. Kumar, S. C. Seo, G. G. Peterson, H. L. Frisch, B. Arkles, and J. Sullivan, J. Electrochem. Soc. 146, 170 (1999).

[R61]J. P. Kurpiewsky, MSME Thesis, Massachusetts Institute of Technology (2005).

[R62]G. A. Bertero, PhD Dissertation, Stanford University (1995).

[R63]X.P. Qu, J. J. Tan, M. Zhou, T. Chen, Q. Xie, G. P. Ru, and B. Z. Li, Appl. Phys. Lett. 88, 151912 (2006).

[R64]S. W. Jung, W. I. Park, G. C. Yi, and M. Kim, Adv. Mater. 15, 1358 (2003).

[R65]Dimension 3100 manual, Veeco Instruments Inc.

[R66]L. Belliard, J. Miltat, V. Kottler, V. Mathet, C. Chappert, and T. Valet, J. Appl. Phys. 81, 5315 (1997).

[R67]C. M. Hurd, The Hall effect in metals and alloys, Plenum press, NY-London, 1972.

[R68]C. L. Canedy, X. W. Li, and G. Xiao, J. Appl. Phys. 81, 5367 (1997).

[R69]F. Ferdousi, H. Seinige, U. Roy, J. Mantey, M. Tsoi, and S. K. Banerjee, SRC TECHCON 2011.

[R70]C. L. Zha, J. Persson, S. Bonetti, Y. Y. Fang, and J. Åkerman, Appl. Phys. Lett. 94, 163108 (2009).

[R71]L. Berger, Phys. Rev. B 2, 4559 (1970).